

PETE'S THESIS

by

Peter Thompson

A thesis submitted in conformity with the requirements
for the degree of Doctor of Philosophy
Graduate Department of Physics
University of Toronto

Copyright © 2011 by Peter Thompson

Abstract

Pete's Thesis

Peter Thompson

Doctor of Philosophy

Graduate Department of Physics

University of Toronto

2011

(At most 150 words for M.Sc. or 350 words for Ph.D.)

Contents

1	The LHC and the ATLAS Detector	1
1.1	the Large Hadron Collider	1
1.2	The ATLAS Detector	2
1.2.1	Inner Detector	2
1.2.2	Calorimeters	5
1.2.3	Forward Calorimeters	10
1.2.4	Muon Spectrometer	20
1.2.5	Trigger and Data Acquisition	21
2	The Standard Model	24
2.1	Overview	24
2.2	Quantum ChromoDynamics	26
2.2.1	Factorisation	28
2.2.2	Hadronization and Jet Production	31
3	Inclusive Jet Cross Section	33
3.1	Introduction	33
3.2	Jets in ATLAS	35
3.2.1	Topological Clustering	35
3.2.2	Jet-Finding Algorithms	36
3.2.3	Jet Energy Scale Calibration	38

3.2.4	JES uncertainty	41
3.2.5	Jet Selection	44
3.3	Event Selection and Data quality	47
3.3.1	Triggers used for the inclusive jet analysis	47
3.3.2	Transition Bin	50
3.3.3	Dijet Triggers	52
3.4	Data Correction	55
3.4.1	IDS method	56
3.4.2	Matching Efficiency	57
3.5	Treatment of uncertainties	59
3.5.1	Statistical uncertainties	59
3.5.2	Systematic Uncertainties	59
3.6	Results and discussion	61
3.6.1	Inclusive Jet Cross Section	61
3.6.2	Dijet Mass Spectrum	62
4	TestBeam Overview	71
4.1	Introduction	71
4.2	Beamline Instrumentation	73
4.2.1	Timing and Pulse Shapes	77
4.2.2	Offline Reconstruction	78
4.3	Simulation	79
4.3.1	Geant4	80
4.3.2	Reconstruction of Simulation Results	82
4.3.3	Noise Generation and Application	84
5	Testbeam Results	86
5.1	Event Selection	86

5.2	Electron analysis	88
5.2.1	Cylindrically Clustered Results	88
5.2.2	Hadron Results	102
5.3	Topologically Clustered Results	113
5.3.1	Electrons	113
5.3.2	Hadrons	117
5.3.3	Cluster moments	122
	Bibliography	129

Chapter 1

The LHC and the ATLAS Detector

1.1 the Large Hadron Collider

The Large Hadron Collider (LHC) is a particle accelerator near Geneva, Switzerland. It is 27km in circumference and is located between 45m and 170m underground, crossing the swiss-french border four times. Designed to accelerate two beams of protons to energies of 7 TeV, and to collide these beams at four points along its circumference with an instantaneous luminosity of $10^{34}\text{cm}^{-2}\text{s}^{-1}$.

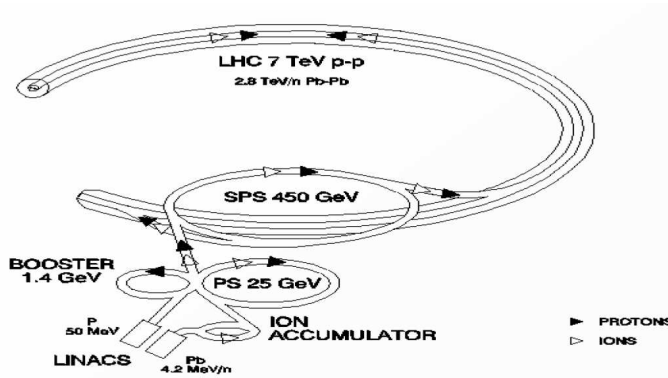


Figure 1.1: Injection chain for protons and ions feeding the LHC.

The injection chain for beam particles is shown in figure 1.1. Hydrogen gas is used as a source of protons. Gas molecules are ionised, and the protons are then accelerated

to an energy of 50 MeV in a linear accelerator (LINAC2). A series of synchrotrons (the Proton Synchrotron Booster (PSB), Proton Synchrotron (PS), and Super Proton Synchrotron (SPS)) are then used to accelerate protons to energies of 1.4 GeV, 25 GeV and 450 GeV, respectively. After acceleration by the SPS, beams are injected into the LHC. The LHC beam consists of 2808 bunches, each containing $\sim 10^{11}$ protons, which are separated in time by 24.95 ns. Superconducting Radio-Frequency (RF) cavities are then used to accelerate the protons to their final energy. At present, protons in the LHC are being accelerated to 3.5 TeV per beam, which is half of the design energy. It is also capable of accelerating heavy ions to high energy, and the ALICE experiment is focused on analysing these collisions.

1.2 The ATLAS Detector

The ATLAS detector (shown in figure 1.2) is a multipurpose detector used to analyse collisions at the LHC. It is one of two multi-purpose detectors, the other being the Compact Muon Solenoid (CMS). It consists of sophisticated particle tracking systems, several calorimeters, and a muon spectrometer.

1.2.1 Inner Detector

The inner detector is used to reconstruct the trajectories (tracks) of charged particles produced during proton-proton collisions. It is comprised of three elements: the pixel, the SemiConductor Tracker (SCT), and the Transition Radiation Tracker (TRT). These three components are contained within a cylindrical region of length 3.5m and radius 1.15m centred on the ATLAS interaction point. The ATLAS solenoid immerses this area in a 2T magnetic field oriented along the z axis. The applied field gives rise to curvature in the trajectories of charged particles, which can then be used to obtain measurements of particle momenta.

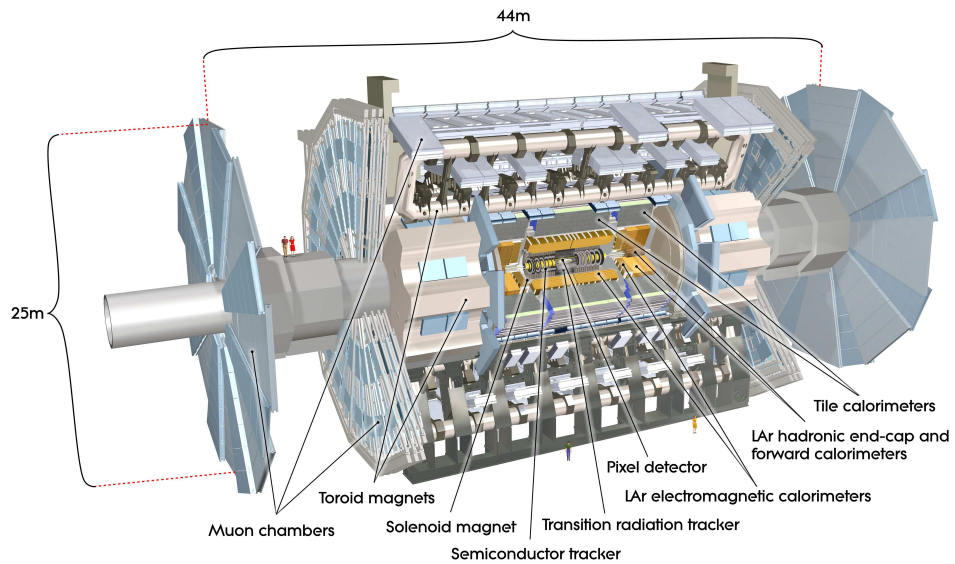


Figure 1.2: Diagram of the ATLAS detector.

The inner detector consists of a barrel section (shown in figure 1.3 and two end cap sections (figure 1.4).

The pixel detector sensors are formed from $250\mu\text{m}$ thick wafers of silicon. The barrel section consists of three cylindrical layers, and three disc like layers are used to form each end cap. All together there are $\sim 8 \times 10^7$ pixel channels, providing a hit resolution of $10\mu\text{m}$ in the $R - \phi$ plane and $115\mu\text{m}$ in the z direction.

The SCT is located beyond the pixel detector, and consists of 4 cylindrical layers in the barrel section and 9 disc layers in each end cap. Each SCT module has semiconducting microstrip sensors mounted on both sides. The sensors on either side are oriented at an angle of 40 mrad to each other. As a single microstrip sensor only provides a position measurement in one dimension, orienting two at a slight angle allows the position of the hit to be measured in two dimensions. This gives the SCT a resolution of $17\mu\text{m}$ in the $R - \phi$ plane and $580\mu\text{m}$ in z .

The TRT is the outermost section of the inner detector, and is formed from drift (straw) tubes. The barrel section contains $\sim 52,500$ tubes, while $\sim 123,000$ tubes are contained in each end-cap section. Each straw is made from polyimide and is 4mm in

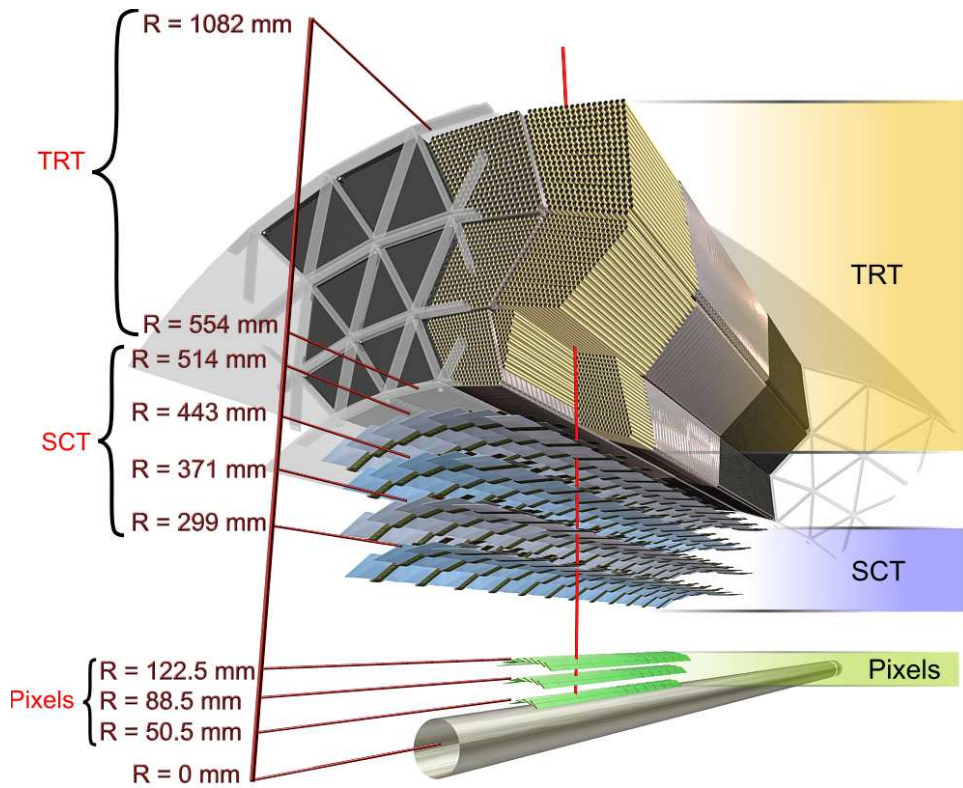


Figure 1.3: Diagram of the barrel section of the inner detector.

diameter, and has a gold plated tungsten wire (with diameter $30\mu\text{m}$) located in the centre of the tube that acts as an anode. The gas in the tubes is made up of 70% Xe, 27% CO_2 and 3% O_2 . Particles entering the tube ionise the gas, with the resulting electrons drifting towards the anode in the centre. Measurement of the electron drift time allows the distance of the particle track from the wire to be determined with a resolution of $130\mu\text{m}$. The straw tubes are housed within a volume filled with CO_2 and a matrix of polypropylene fibres. Electrons moving between the CO_2 /polypropylene interfaces will emit transition radiation, which is absorbed by the Xe and leads to an increased signal measured by the straw tubes. The detection of this transition radiation allows the TRT to perform particle identification, discriminating electrons from charged pions.

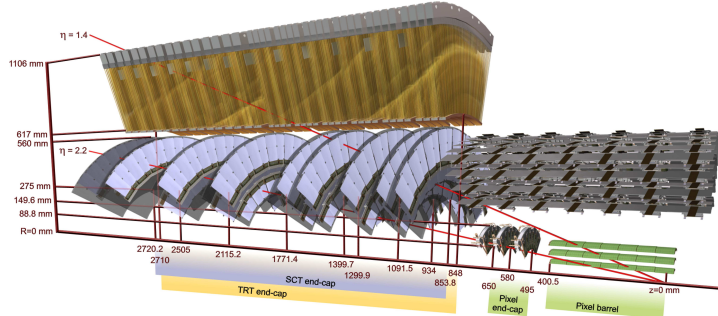


Figure 1.4: Diagram of the inner detector end cap, showing the elements traversed by particles at pseudorapidities of 1.4 and 2.2.

1.2.2 Calorimeters

ATLAS consists of five distinct calorimeters, shown in figure 1.5. The Electromagnetic Barrel and Tile calorimeters are located in the central “barrel” section of ATLAS, while the EMEC, HEC, and FCal calorimeters are located within the end cap cryostats at either end.

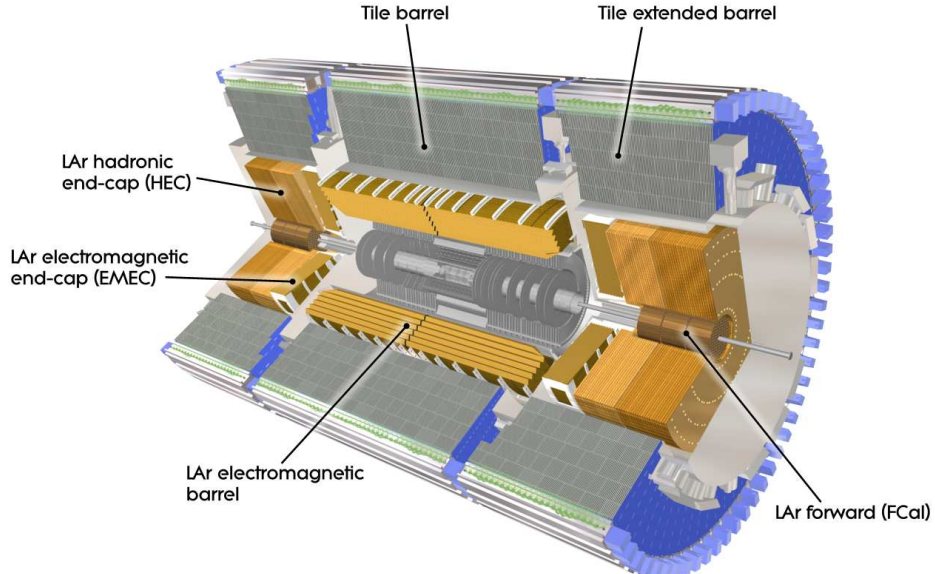


Figure 1.5: The calorimeters of the ATLAS detector.

Barrel calorimeters

The EM Barrel (EMB) calorimeter is a lead/liquid argon calorimeter with a distinctive accordion-shaped geometry. It is made up of two half barrel sections ($z < 0$ and $z > 0$), each divided azimuthally into 16 modules. It covers the pseudorapidity range $0 < |\eta| < 1.475$, and is completely symmetric in ϕ .

The diagram in figure 1.6 shows part of the EM barrel calorimeter. The absorber is formed from plates of lead, which are 1.5mm thick for $|\eta| < 0.8$ and 1.1 m thick for $|\eta| > 0.8$. An 0.2mm sheet of stainless steel is glued onto each side of the lead plate in order to increase the mechanical strength of the absorber sheets. These sheets are then folded into the accordion shape. The folding angle increases with depth (radius) in order to maintain the size of the LAr gap through the calorimeter.

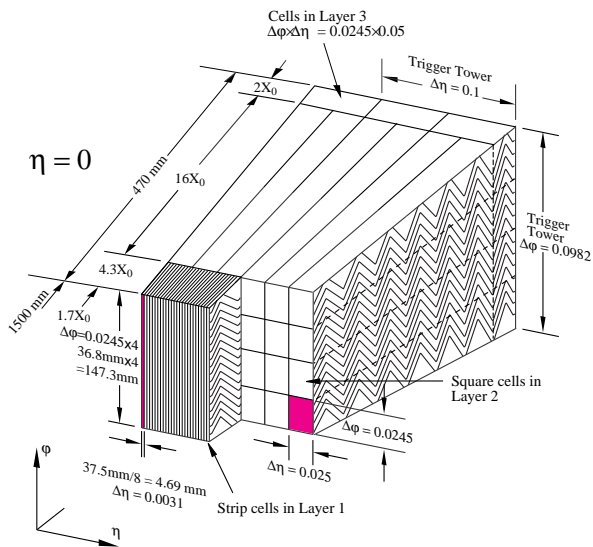


Figure 1.6: Section of the electromagnetic barrel calorimeter, showing the accordion

Flexible Printed Circuit Boards (PCBs) are used to form the electrodes, which consist of three layers of copper separated by polyimide. The electrodes are positioned in between layers of the absorber, with honeycomb spacers being used to keep the electrodes in the centre of these gaps. The absorber layers are grounded, while the two outer layers of copper on each electrode are connected to the HV supply. This creates two active liquid

argon gaps of depth 2.1 mm on either side of the electrode. The inner layer of copper on each electrode is used to read out the signal, as it is capacitively coupled to both the outer layers.

The readout in the EM Barrel calorimeter [?] is divided radially into three layers. The first and last layers are a few X_0 in depth and only catch the beginning and end of the shower, while most of the energy is deposited in the second layer which has a depth of $\sim 17\text{-}20 X_0$. The total depth of the EM calorimeter ranges from 22 to 30 X_0 for pseudorapidities in the range $0 < |\eta| < 0.8$, and from 24 to 33 X_0 in the region $0.8 < |\eta| < 1.3$. The readout granularity in $\Delta\eta \times \Delta\phi$ is 0.003×0.1 , 0.025×0.0245 , and 0.05×0.0245 in layers 1, 2 and 3, respectively. A diagram of the readout layer of the electrode is shown in figure 1.7, in which the different readout granularities are visible.

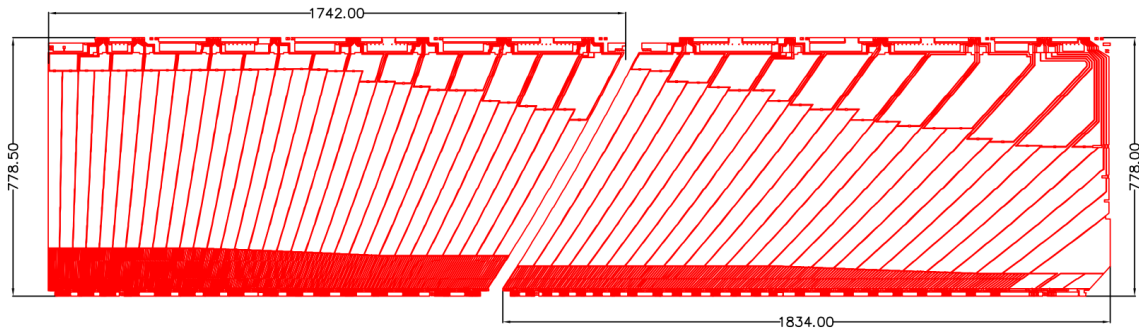


Figure 1.7: Readout layer of an EM Barrel electrode, prior to folding. The piece on the left is used to read out signals from $0 < \eta < 0.8$, while the piece on the right covers the region $0.8 < \eta < 1.475$.

A steel/scintillator “Tile” calorimeter [?] is used to measure the energy of hadronic particles in the barrel region ($|\eta| < 1.7$). It consists of a central barrel section covering the pseudorapidity range $|\eta| < 0.8$, and two extended barrel sections that surround the end cap cryostats. The total depth of the tile calorimeter is 7.4 interaction lengths.

Each section is divided into 64 modules, each of which covers an azimuthal angle of 5.625° . The absorbing material of the calorimeter is formed from a series of steel “master” plates, which are 5mm thick and run the full radial depth of the tile calorimeter (2.0m).

A series of smaller, 4mm thick spacer plates are positioned in between layers of master plates. The spacer plates are used to create gaps between adjacent master plates, and it is within these gaps that the scintillating tiles are located, as shown in figure 1.8. The scintillating tiles are made of polystyrene, which produces scintillation light in the

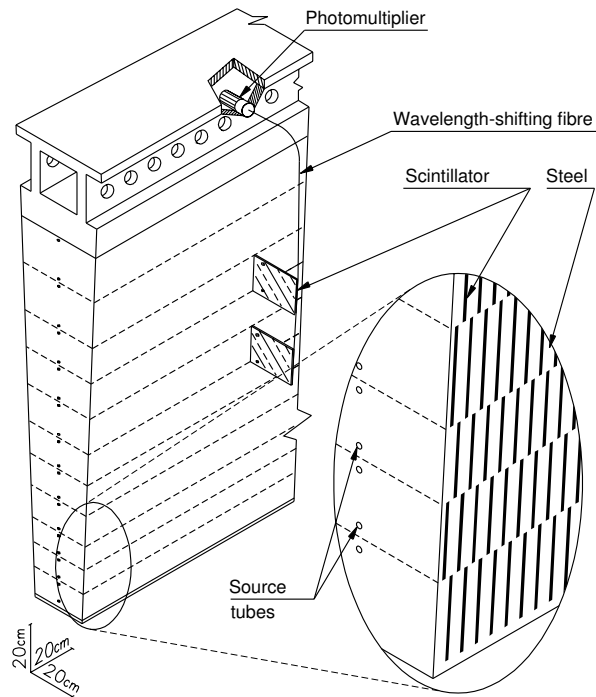


Figure 1.8: Schematic of a tile calorimeter module. Alternating layers of master plates and spacer plates are glued together, with scintillating tiles positioned in the gaps in this structure.

ultra-violet range when excited by the passage of showering particles. The polystyrene is doped with fluors that shift the wavelength of this light into the visible spectrum. Optical fibres are coupled to two sides of each scintillator tile, and are used to carry light from the tiles to the PhotoMultiplier tubes (PMTs). The PMTs then convert the scintillation light to an electronic signal, and are housed within the mechanical support structure of the calorimeter.

End Cap calorimeters

The Electromagnetic End Cap (EMEC) and Hadronic End Cap (HEC) Calorimeters are housed within cryostats at either end of the detector.

The EMEC covers the pseudorapidity range $1.375 < |\eta| < 3.2$, and has a similar design to the EM Barrel calorimeter. As with the barrel, the absorber is formed from accordion shaped layers of lead sheets, while the active regions consist of the liquid argon gaps between these layers. Honeycomb spacers are used to keep the electrodes positioned in the centres of these gaps.

The EMEC consists of two coaxial wheels, with the boundary between wheels located at $|\eta| = 2.5$. Each wheel is further divided into eight wedge-shaped modules. Due to the accordion shape of the absorber layers, there are no discontinuities in the calorimeter between adjacent modules. As with the EM barrel, the structure of the EMEC is completely symmetric with respect to azimuthal angle. The readout of inner wheel has a granularity of 0.1×0.1 in $\Delta\eta \times \Delta\phi$. The granularity of the outer wheel varies with pseudorapidity, but is at its finest (0.003×0.1) in the region $1.5 < |\eta| < 1.8$.

The HEC calorimeters [?] utilise a flat plate geometry, which consists of alternating layers of copper and liquid argon oriented at right angles to the beam. Each section of the HEC consists of a front wheel and a rear wheel, each of which is divided azimuthally into 32 wedge-shaped modules. The front wheel is comprised of a front plate which is 12.5 mm thick, as well as 24 copper plates, each of which is 25mm thick. The rear wheel contains a front plate that is 25mm thick, and is followed by 16 plates of thickness 50mm.

In both wheels, the liquid argon gaps formed between the absorber plates have a depth of 8.5mm. These gaps are then divided into four sub-gaps of depth ~ 2 mm by a set of three parallel electrodes, forming an electrostatic transformer [?]. The signal is read off from a central pad in the middle electrode, with the shapes etched into this pad determining the read-out structure. Cells in the HEC have a granularity of 0.1×0.1 in $\Delta\eta \times \Delta\phi$ for $|\eta| < 2.5$, and a granularity of 0.2×0.2 at higher pseudorapidities.



Figure 1.9: photograph of an EMEC module, showing the accordion structure of the absorbers. The boundary between the inner wheel and the outer wheel can be seen towards the left, where the shape of the absorber plate changes.

1.2.3 Forward Calorimeters

The ATLAS Forward Calorimeters (FCal) are located just outside the beampipe, 4.7m away from the ATLAS interaction point on either side. These are Liquid Argon (LAr) based calorimeters, and are located within a special support tube inside the end-cap cryostat (figure 1.11).

The FCal consists of three modules, one electromagnetic module (FCal1) and two hadronic modules (FCal2 and FCal3). Each module has a cylindrical shape, with an outer radius of 450mm and a depth of 440mm. A plug made of brass alloy has a similar shape and is located behind the hadronic modules in order to provide additional shielding for the muon chambers behind it. As the FCal operates at a temperature of about 90K in ATLAS, “cold” lengths will be used in the following when quoting dimensions and densities, etc.

The electromagnetic modules of the FCal were produced by the university of Arizona. Each module consists of a number of circular copper plates with an inner radius of 72mm

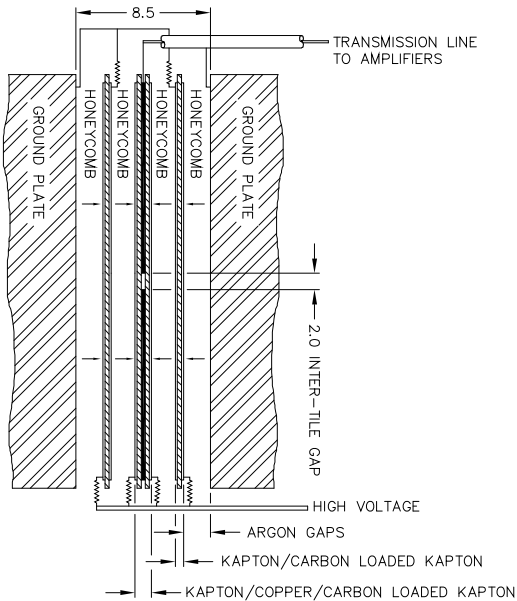


Figure 1.10: Electrode structure in the HEC. Electrodes are arranged to form an electrostatic transformer

and an outer radius of 455mm. On one side (the ATLAS “A” side, $z > 0$ in the ATLAS coordinate system), the FCal 1 module consists of 18 plates of thickness 24 mm, whereas on the opposite side (the “C” side) 19 slightly thinner plates are used. Each plate is drilled with a hexagonal array of holes into which the electrodes were inserted. This was done in a way that established a good electrical connection between the outside of the electrode and one of the copper end-plates. Each electrode consists of a copper tube (the cathode) containing a copper rod (anode) around which a PEEK fiber is wrapped. The inner diameter of the copper tubes is 2.62 mm while the diameter of the copper rods is 2.35mm, thus leaving a gap of 267 μm which is filled with liquid Argon. The PEEK fiber has a diameter of 250 μm , and is present to keep the rod positioned in the centre of the tube, thus maintaining the uniformity of the LAr gap throughout the electrode and keeping the rod electrically isolated from the tube. Typical gap sizes used in LAr

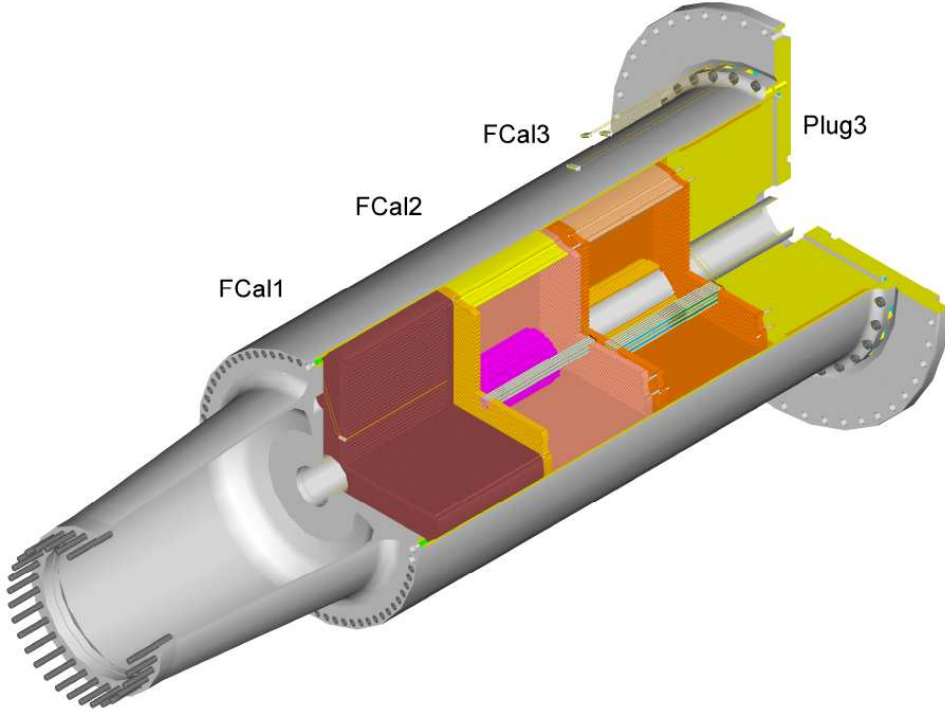


Figure 1.11: Cut-away view showing the FCal within its support tube (taken from [?]).

calorimeters are on the order of a few millimetres. However, as the FCal is located at high pseudorapidity minimum bias events will deposit energy in it at a very high rate. The smaller gap size is required in order to reduce the drift time across the gap, and thus preventing the high rate of ionization from causing a build-up of positive ions in the liquid argon. The distance between electrodes in FCal1 is similar to the Molière radius (a measure of the lateral spread of an electromagnetic shower) for copper. EM showers in the FCal should thus spread across several electrodes, allowing the calorimeter to sample the shower effectively. Copper also allows the FCal1 module to conduct heat efficiently. The Cryostat temperature is kept at 90K, while the boiling point for liquid argon is 92.7K. With the LHC running at design luminosity, minimum bias events are expected to heat the FCal at a rate of 45W, with about half of that power going into FCal1. A finite element analysis estimated that this heating would cause a temperature increase within the FCal of no more than 1.5K, which is not enough to cause the liquid argon to

boil[?].

The hadronic modules of the FCal were produced at the University of Toronto (FCal2) and at Carleton University in Ottawa (FCal3). Each of these modules uses two copper end plates drilled with a hexagonal array of holes, each of which holds an electrode. The electrodes in these cases use copper tubes for their anodes but rods made of pure tungsten (with density 19.2) for the cathodes. The absorbing matrix is formed from small slugs of tungsten alloy (“WFeNi” - 97% tungsten/2% Iron/1% Nickel) positioned in the gaps between the electrode tubes. The material composition and density of the calorimeter components are important factors when establishing a description of the calorimeter to be used by simulations. By themselves, the WFeNi slugs have a measured mean density of 18.3 g/cm³. When considering the WFeNi slugs, the copper electrode tubes, the tungsten rods and any spaces in the absorber matrix that are filled with liquid argon, the average density of absorbing material in the hadronic modules is 14.33 g/cm³ for FCal2 and 14.45 g/cm³ for FCal3 [?]. A diagram showing the way in which the WFeNi slugs are positioned amongst the electrodes is shown in figure 1.12

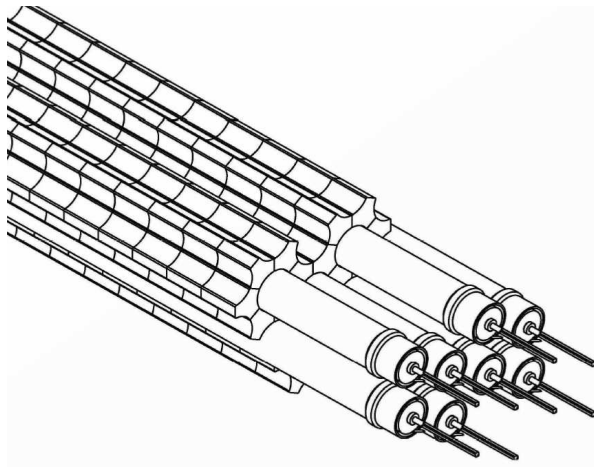


Figure 1.12: Diagram showing the arrangement of electrodes and slugs in the hadronic modules (taken from [?]).

quantity	FCal1	FCal2	FCal3
Absorber material	Copper	Tungsten	Tungsten
Module inner diameter	720 mm	790 mm	860 mm
Electrode Separation	7.5mm	8.62 mm	9.0mm
Rod Diameter	2.35 mm	2.47 mm	2.75 mm
Tube inner diameter	2.62 mm	2.84 mm	3.25 mm
LAr Gap	267 μm	375 μm	500 μm
distance from IP to front face	4668.5mm	5128.3 mm	5602.8

Table 1.1: Dimensions of the FCal modules.

FCal Electronics

An electric field of $\sim 1\text{KV/mm}$ is conventional for liquid argon calorimeters. In order to provide this the rods of each electrode are supplied with high voltage while the tubes are grounded. Showering particles ionize the liquid argon, leaving free electrons and Ar^+ ions in the gap. The electric field in the gap then causes this charge to drift resulting in a current pulse, which is used as a signal. This pulse is triangular in shape, having a fast rise time ($\sim 1\text{ ns}$) and taking $\sim 61\text{ ns}$ (in FCal1) to return to zero [?]. The pulse peak corresponds to the amount of charge deposited in the liquid argon, and is thus proportional to the amount of energy deposited in the liquid argon.

The signal is read out on the same line that supplies the electrodes with high voltage. Electrodes in the FCal are ganged together on interconnect boards to form “tube groups”. Tube groups are formed from four electrodes in FCal1, six electrodes in FCal2, and nine electrodes in FCal3. The rods from these electrodes are connected to the interconnect board, which is supplied with HV via a coaxial cable as shown in figure 1.13. The tubes are also grounded through this coax: each interconnect board is connected to the FCal end plate. The line supplying HV to the tube group also serves as a readout line, carrying the signal off the interconnect board. As the interconnect board connects electrodes in parallel, the signal carried off the interconnect board is the sum of the current pulses in each electrode of that tube group.

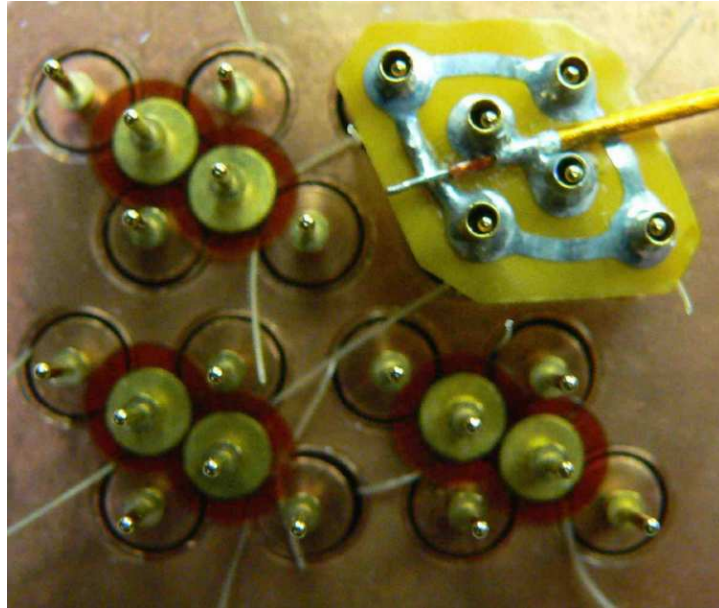


Figure 1.13: Photo of an endplate of FCal1, taken during assembly, showing the interconnect board and the coaxial cable used for HV delivery and readout [?]. Also visible are the PEEK fibres used to keep the rods centred within the tubes. The two central pins in each group are used to ground the end plate, and thus the tubes, while the four exterior pins provide HV to the rods.

The readout lines are then fed out to a summing board. On each summing board, four read-outs from the interconnect boards are further combined to form a single channel. One FCal channel thus corresponds to four tube groups, which is equivalent to 16/24/36 electrodes in FCal1/FCal2/FCal3. The summation is carried out through a transmission line transformer, which serves to match the impedance of the readout coax to that of the "pigtail" cable used to carry the signal away from the summing board (figure 1.14). A different HV source is used to supply each tube group, so that if one source fails then the other three tube groups in the channel should still be powered. This is the case in ATLAS, where one of the lines supplying HV to the A side of the FCal is severed. This line supplies HV to one quadrant of FCal3, leaving one quarter of the tube groups in the affected area without HV. The remaining tube groups still contribute signal to the channels in this area, and so energy deposited in this region may still be measured. Near

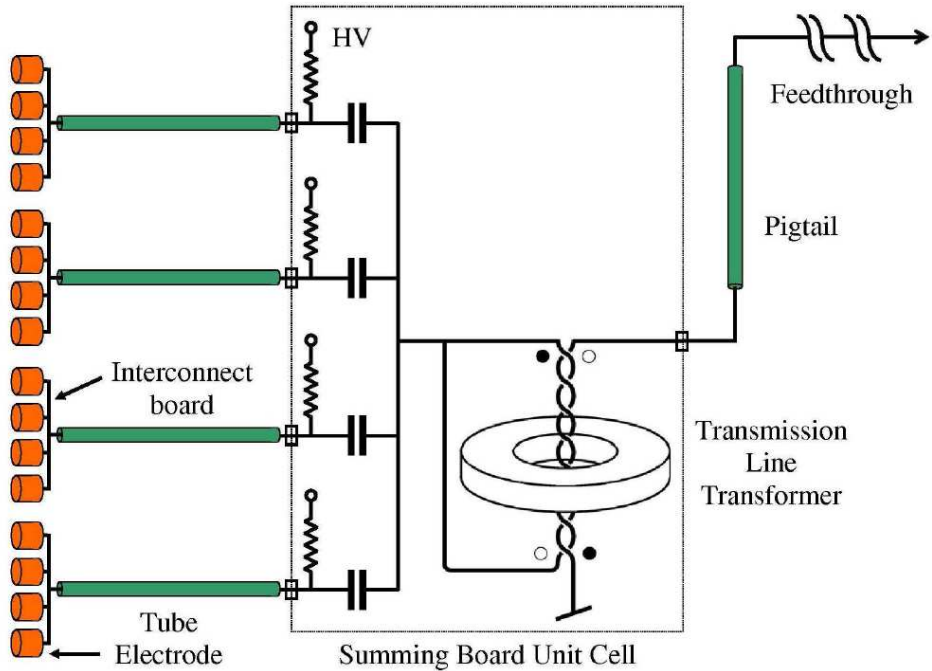


Figure 1.14: Illustration of a summing board used in the readout electronics. A single channel is composed of four tube groups, which each consist of 4/6/9 electrodes in FCal1/FCal2/FCal3.

the inner and outer edges of the FCal the tube groups are irregularly shaped, and it is not feasible to sum these in a coherent manner. These tube groups form the "unsummed" channels. The unsummed channels located near the inner edge (high η) also provide a readout with finer $\eta - \phi$ granularity than summed channels would in this region.

The summing boards are located inside the cryostat. The pigtails carry the signal from the summing boards out of the cryostat feedthrough to the Front End Boards (FEBs), which are used in the electronics chains of all the liquid argon calorimeters. On the FEB, the signal is preamplified and then shaped. The shaping consists of one differentiation and two integration steps (CR-RC²) resulting in a bipolar pulse shape. This is done in order to improve the signal to noise ratio of the pulse [cite this](#). In the other LAr calorimeters it takes much longer for the triangular current pulse to drop from its peak value back to zero: this time is ~ 400 ns in the EM barrel but only ~ 60 ns in

the FCal [?]. In these cases the shaping also allows the signal to be read out much faster, as the relevant information can be obtained from the first $\sim 125\text{ns}$ of the shaped pulse. The shaping consists of one differentiation and two integration steps (CR-RC²) resulting in a bipolar pulse shape. The pulse is also amplified at the same time it is shaped. Three different gains (low, medium, and high) are used. The amplification used for high gain is about 10 times as much as that used for medium gain, which in turn is about 10 times higher than that used for low gain.

Timing on the FEB is managed by a Trigger Timing Control (TTC) chip, which distributes clock pulses every 25ns. The signal (at each gain) is sampled at every 25ns, and stored (as an analog voltage) on a Switched Capacitor Array (SCA) circuit. The pulse shapes for the three FCal modules are shown in figure 1.15. Each pulse consists of an initial positive lobe followed by a longer negative lobe, the start of which can be seen in the figure.

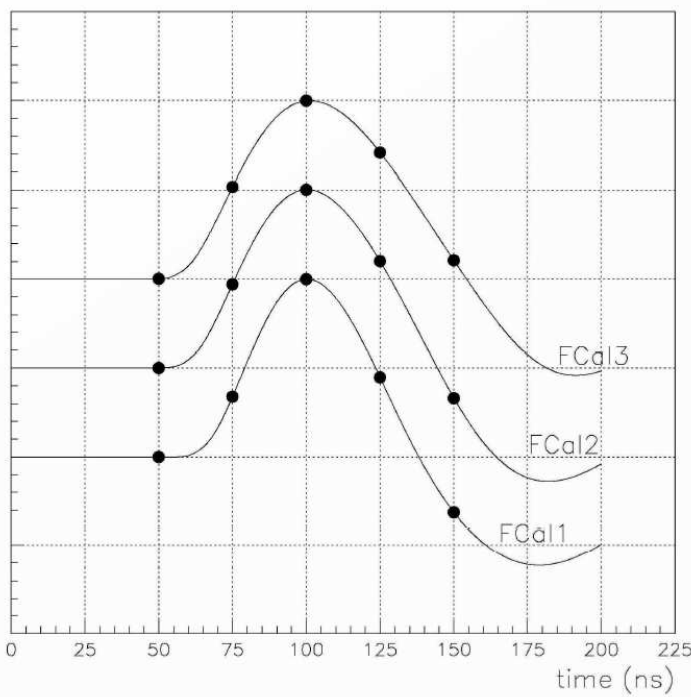


Figure 1.15: Pulse shapes for each module. The dots indicate the times at which they are sampled and digitized.

When a trigger signal indicates that the event should be read out, the pulse samples are read off the SCA and fed to an ADC (Analog to Digital Converter). For each sample the ADC then outputs a 12-bit signal, which is a discretized voltage capable of taking one of 4,096 distinct logical levels. Generally only a single gain is read out of the SCA and digitized, and so a gain selector chip is used to determine which gain will yield the largest pulse height without saturating the ADC output. As the pulse shape has a negative lobe, a “pedestal” value must be subtracted from the digitised output in order to represent a negative value. To achieve this, an offset is added to the samples read from the SCA just prior to them being digitised. The offset voltage is chosen such that the pedestal value is around 1,000 ADC counts, leaving around 3,000 ADC counts to represent the positive lobe of the pulse. The pedestal value is calculated using physics data on a run by run basis. For each channel, the first sample of each pulse is averaged over the entire run, and this value is used as the pedestal during reconstruction.

Signal Reconstruction/Optimal Filtering Method

Offline reconstruction of the energy deposited in the calorimeter is done through the use of optimal filtering coefficients (OFCs) [?]. These coefficients may be used to reconstruct the amplitude of the signal pulse and its timing in such a way that the effect of the noise on the reconstruction is minimised.

The OFC method produces two sets of coefficients, a_i and b_i , which on average correctly produce the pulse amplitude A and time shift τ :

$$A = \left\langle \sum_i a_i S_i \right\rangle \quad (1.1)$$

$$A\tau = \left\langle \sum_i b_i S_i \right\rangle, \quad (1.2)$$

where S_i is the value of the i -th signal sample, after pedestal subtraction. Given that

the pulse shape, $g(t)$ is known, these samples may be expressed as

$$S_i = Ag(t_i - \tau) + n_i = Ag(t_i) - A\tau g'(t_i) + n_i, \quad (1.3)$$

where g' is the derivative of the pulse shape and n_i is the noise present in the i -th sample.

Equations 1.1 and 1.2 may then be rewritten as

$$A = \sum_i a_i Ag(t_i) - a_i A\tau g'(t_i) + a_i \langle n_i \rangle \quad (1.4)$$

$$A\tau = \sum_i b_i Ag(t_i) - b_i A\tau g'(t_i) + b_i \langle n_i \rangle \quad (1.5)$$

The coefficients should be chosen in such a way that the variances of A and $A\tau$ are minimised. As the mean value of the noise is zero, these variances may be written as

$$\text{Var}(A) = \sum_{i,j} a_i a_j \langle n_i n_j \rangle \quad (1.6)$$

$$\text{Var}(A\tau) = \sum_{i,j} b_i b_j \langle n_i n_j \rangle, \quad (1.7)$$

where $\langle n_i n_j \rangle$ is simply the autocorrelation matrix of the noise between samples. This minimisation may be carried out using the method of Lagrange multipliers, with constraints

$$\sum_i a_i g_i = 1, \quad \sum_i a_i g'_i = 0$$

$$\sum_i b_i g_i = 0, \quad \sum_i b_i g'_i = -1$$

obtained from equations 1.4 and 1.5.

A SPICE [15] simulation of the electronics chain is used to obtain an initial estimate of the pulse shape used in the OFC calculation. This estimate was then improved using an iterative procedure that incorporated data taken from physics runs. The data used in this procedure is taken from events in which have a large pulse amplitude, in order to ensure that the signal is coming from a physical energy deposit.

1.2.4 Muon Spectrometer

The muon spectrometer is the outermost system of the ATLAS detector, and is illustrated in figure 1.16. It is capable of measuring muon momenta in the region $|\eta| < 2.7$, with a momentum resolution of $\sim 10\%$ at 1 TeV, and can trigger on muons with $|\eta| < 2.4$. The muon spectrometer is comprised of four types of sensors: Monitored Drift Tubes (MDTs), Cathode Strip Chambers (CSCs), Resistive Plate Chambers (RPCs) and Thin Gap Chambers (TGCs). The MDTs and CSCs are used to measure the kinematics of muons, while the TGCs and RPCs are used for triggering.

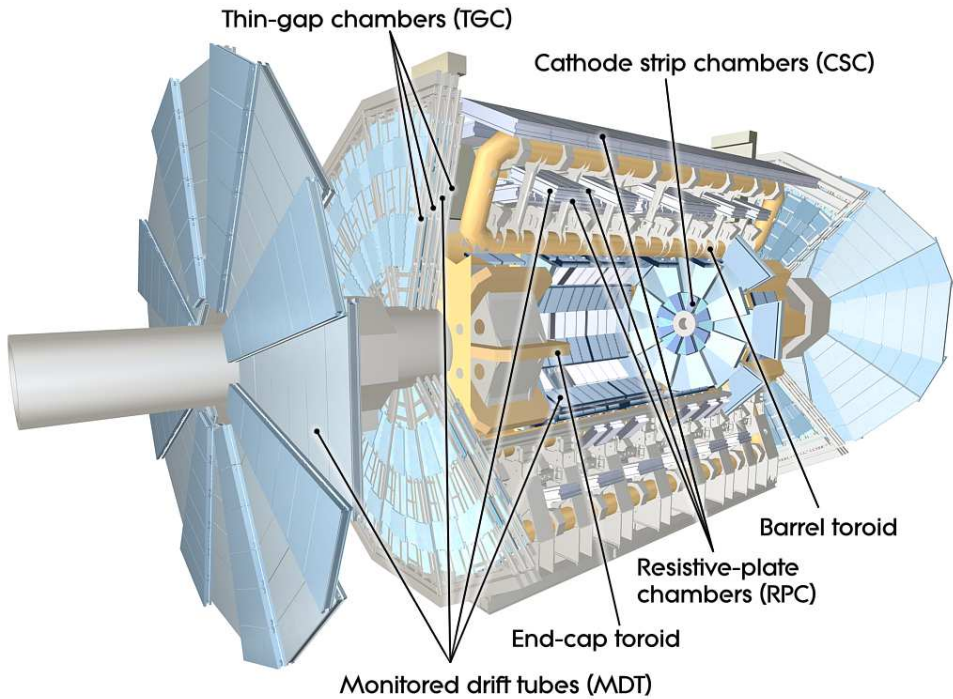


Figure 1.16: The different components of the Muon spectrometer. The MDT and CSC components are used for measuring muon

The toroid magnets (located in the barrel and end caps) produce a toroidal field, which causes charged particles to bend in the $R - z$ plane. In order to measure track momenta with high resolution, the alignment of the MDT and CSC chambers must be well known. A high precision optical system is used to measure the positions and

mechanical deformations of the measurement chambers, which must be known to within $30\ \mu\text{m}$ in order to achieve the desired momentum resolution.

MDTs are comprised of cylindrical drift chambers of diameter 29.97mm, with a central anode wire of diameter $50\mu\text{m}$. A mixture of Argon (93%) and CO_2 (7%) is used to fill the tubes. Each tube is capable of measuring the distance of a muon track to the anode wire with a resolution of $80\mu\text{m}$. Arranged in three layers in the barrel and two in the end cap.

In the end cap sections, the innermost layer of measurement chambers is made up of CSCs. the MDTs are unable to withstand the high levels of radiation present at these locations ($|z| \sim 7\text{m}$), and so CSCs are used instead. These are multi-wire proportional chambers (MWPCs), filled with a mixture of Argon (80%) and CO_2 (20%). The CSCs are capable of measuring hit position to within $60\ \mu\text{m}$ in the bending plane, achieving the desired momentum resolution.

For triggering purposes, RPCs are used in the barrel region ($|\eta| < 1.05$) while TGCs (which are a form of MWPC) are used in the end cap region ($1.05 > |\eta| > 2.4$). The intrinsic response time of these detectors is on the order of a few nanoseconds, enabling them to reliably identify the bunch crossing in which any detected muons were produced.

1.2.5 Trigger and Data Acquisition

Collisions between proton bunches occur at ATLAS at a rate of 40MHz, whereas the maximum rate at which event data can be recorded is 200Hz. The trigger system is in place in order to ensure that as many interesting events are recorded as possible, while rejecting less interesting events. The ATLAS trigger system consists of three consecutive levels: level one (L1), level 2 (L2), and the Event Filter (EF). The L1 trigger selects candidate events at a maximum rate of 75 kHz. Some of these events are subsequently rejected at L2, reducing the acceptance rate to 3.5 kHz. The final level of event rejection is done by the EF, which accepts events at the desired rate of 200 Hz.

The L1 trigger utilises custom-built hardware, and needs to decide whether to accept or reject the event within $2.5 \mu\text{s}$ of the corresponding bunch crossing. The level 1 trigger consists of three of three parts, L1 Calo, L1 muon, and the Central Trigger Processor (CTP). The L1 Calo trigger is used to select electrons, jets, taus, and other high p_{T} objects, while the L1 muon trigger processes signals from the RPCs and TGCs of the Muon spectrometer.

The CTP decides whether an event is accepted or rejected at L1. Trigger conditions are specified in a “menu”, where each object on the menu is some combination of trigger items from L1Calo and/or L1Muon. The CTP also handles the prescales on menu objects, which are used to control the bandwidth allowed for each item and keep the L1 acceptance rate at the desired level. For a menu item with a prescale of 50, one event will be accepted at L1 for every fifty events that satisfy the trigger conditions associated with that menu item. Menu items associated with a rare or particularly interesting event topology may be given a prescale of one, in which case the event is accepted every time the trigger conditions are met. Frequently occurring or less interesting topologies (such as those containing low-pt jets) are given higher prescales.

The available time in which the L1 decision must be made is too short for L1Calo to consider the information from individual calorimeter cells, and so readouts from these cells are grouped together to form trigger towers. In the barrel and end cap regions ($|\eta| < 3.2$), these trigger towers have a granularity 0.1×0.1 in η and ϕ . The level 1 central jet trigger combines 2×2 blocks of trigger towers to form “jet elements”, which then have a granularity of 0.2×0.2 in $\eta - \phi$ space. A sliding window algorithm is then used to identify jets [?]. The window consists of a 4×4 grid of jet elements, and a jet is reconstructed if the total E_{T} within the window exceeds a given threshold. For example, the “L1_J10” algorithm requires the transverse energy in the in the window to exceed 10 GeV. Additionally, the 2×2 cluster of jet elements in the centre of the window is required to be a local maximum, that is, the central cluster must have a transverse energy greater

than that of any other 2×2 block of jet elements within the window.. If these criteria are met, then the event is accepted by the jet algorithm. The 0.4×0.4 area of $\eta - \phi$ at the centre of the window is then identified as a “Region of Interest” (ROI), and is passed on to any relevant L2 trigger algorithms.

The forward jet trigger is used to identify jets in the region $|\eta| > 3.2$, and operates independently of the central jet trigger. While the central jet trigger uses information from the EM Barrel, tile, EMEC and HEC calorimeters, the forward jet trigger relies only on the FCal. Trigger towers in the FCal have a granularity of 0.4×0.4 in $\eta - \phi$, which is coarser than in other calorimeters. A jet element is then formed by summing all FCal trigger towers in η , such that the jet element has dimensions 1.2×0.4 in η and ϕ , respectively. Jets are then identified using the same sliding window algorithm as the central jet trigger.

At L2, the trigger decision needs to be made within 40ms. This interval is sufficient for cell based methods to be used, although only cells within the region of interest (about 2% of the detector) are read out. A cone-based algorithm is used for jet identification: a cone of fixed radius $\Delta R = \sqrt{\Delta\eta^2 + \Delta\phi^2}$ is positioned at the centre of the RoI. Energy weighted values of η and ϕ are obtained by summing cells within the cone, and the centre of the cone is then moved to these coordinates. This process carried out a predetermined number of times.

At the EF level, 4.0s of processing time is available, and so algorithms similar to those used for offline reconstruction (described in section [XX](#)) may be used at the trigger level. Note that the EF was not online while taking the data used in this analysis.

Chapter 2

The Standard Model

2.1 Overview

The Standard Model (SM) describes the particles present in nature and the interactions between them. It has existed in it's current form since 1978, and has been validated by numerous experiments since

Elementary particles in the standard model are divided into two groups: the quarks and leptons. These particles represent the fundamental building blocks of matter, and there are six "flavours" of each. For the quarks these are the up (u), down (d), charm (c), strange (s), top (t), and bottom (b). These may be organised into three mass generations as follows

$$\begin{pmatrix} u \\ d \end{pmatrix} \quad \begin{pmatrix} c \\ s \end{pmatrix} \quad \begin{pmatrix} t \\ b \end{pmatrix}, \quad (2.1)$$

where the upper members of each generation have charge $+2/3$ and the lower members have charge $-1/3$. The leptons may be arranged in the same way, giving

$$\begin{pmatrix} \nu_e \\ e \end{pmatrix} \quad \begin{pmatrix} \nu_\mu \\ \mu \end{pmatrix} \quad \begin{pmatrix} \nu_\tau \\ \tau \end{pmatrix}, \quad (2.2)$$

where the lower members are the electron, muon, and tau, respectively, each having charge -1. Each of these is paired with a neutrino (ν_x), which is neutral and (almost) massless. Quarks and leptons are both fermions, with all twelve of these particles having spin 1/2.

The strong, weak, and electromagnetic forces are also described by the standard model¹. These are described by gauge theories, such that the SM Lagrangian exhibits $SU(3)_c \otimes SU(2)_L \otimes U(1)_Y$ symmetry. The doublets listed in equations 2.1 and 2.2 reflect the way in which the quark and lepton fields transform under the $SU(2)_L$ symmetry group, where the subscript L denotes that only the left handed components of the fields take part in this interaction.

Interactions between particles may occur via the strong (or colour) force, the weak force, and the electromagnetic force. These interactions are described in terms of gauge bosons, which act as force carriers and all have spin 1. The strong force is carried by gluons, which are massless. There are eight types of gluon, corresponding to the 8 generators of the $SU(3)_c$ symmetry associated with the strong force. There would be four massless bosons arising from the $SU(2)_L \otimes U(1)_Y$ symmetries, however these symmetries are broken down to a single $U(1)_{EM}$ symmetry by the Higgs mechanism. This $U(1)_{EM}$ symmetry describes electromagnetic interactions, and the corresponding gauge boson is the massless photon. The other three gauge bosons associated with the broken symmetries are the W^+/W^- bosons which have a mass of 80GeV, and the Z_0 boson which has a mass of 91 GeV.

In addition to the gauge bosons, the standard model also describes a Higgs boson. The Higgs field allows the fermionic particles (and the gauge bosons of the weak force) to possess mass in a way that doesn't violate the gauge invariance of the SM Lagrangian. It is this mechanism that is responsible for the breaking of the electroweak ($SU(2)_L \otimes U(1)_Y$) symmetry. The Higgs field has a potential that makes it favorable for it to take a non

¹gravity is not included in the SM, but its effects are negligible at the energy scales of interest.

zero vacuum expectation value. Fermions and gauge bosons then interact with the Higgs field via a Yukawa coupling, and so when the Higgs takes a vev these couplings act as mass terms in the Lagrangian, while retaining their gauge invariance. At present the Higgs boson is the only particle in the standard model that has not been experimentally observed. However, The ATLAS experiment has narrowed the mass range of the Higgs boson to be within 115-131 GeV[?]. If the Higgs boson exists, it is expected to be observed at ATLAS by the end of 2012.

2.2 Quantum ChromoDynamics

The physics of the strong force are described by Quantum ChromoDynamics (QCD), which is a gauge theory based on the symmetry group $SU(3)_c$. It is the strongest of the three interactions in the standard model, and effects quarks but not leptons. As the LHC collides beams of protons, QCD is the dominant interaction. LHC collides protons, therefore QCD is dominant interaction. QCD: non abelian gauge theory of $SU(3)$. As mentioned above, gauge particles are gluons, of which there are 8 types.

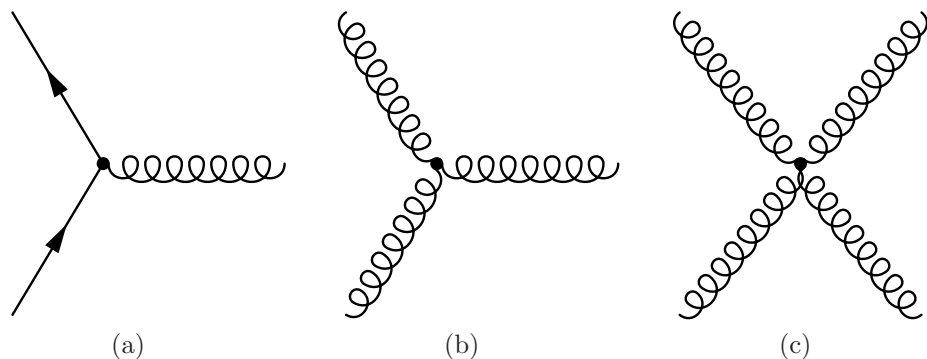


Figure 2.1: Feynman diagrams depicting the vertices of QCD.

Feynman diagrams for QCD vertices are shown in figure 2.3. A major difference of QCD compared to quantum electrodynamics (QED) is that gluons carry colour charge and thus interact with themselves, while the photon is chargeless. Gluon-gluon interac-

tions can occur via the three gluon or four gluon vertices, which are depicted in figures 2.1(b) and 2.1(c).

The coupling constant, α_s , describes the strength of QCD interactions. This varies as a function of momentum, such that the strength of the coupling at two different momentum scales, q^2 and Q^2 , are related by

$$\alpha_s(q^2) = \frac{\alpha_s(Q^2)}{1 + \frac{11-2/3N_f}{4\pi} \alpha_s(Q^2) \log(\frac{q^2}{Q^2})} \quad (2.3)$$

where N_f is the number of quark flavours with mass less than q^2 and Q^2 . The “QCD scale”, Λ_{QCD} , is defined as the scale at which the denominator of equation 2.3 vanishes, such that

$$\frac{11 - 2/3N_f}{4\pi} \alpha_s(Q^2) \log(\frac{\Lambda_{QCD}^2}{Q^2}) = -1. \quad (2.4)$$

Using this definition, equation 2.3 becomes

$$\alpha_s = \frac{4\pi}{(11 - 2/3N_f) \log(\frac{-q^2}{\Lambda_{QCD}^2})}. \quad (2.5)$$

The value of Λ_{QCD} is around 200-300 MeV. This does not mean that the coupling constant is infinite at Λ_{QCD} , merely that the perturbative calculations used in the derivation of eqn 2.3 are no longer valid in this regime. When measured at the mass of the Z boson, the coupling constant $\alpha_s(M_Z) = 0.12$, indicating that perturbation theory is reliable at this energy scale.

A leading order diagram for a $qq \rightarrow qq$ process is shown in figure 2.2(a), where momentum is exchanged between two quarks via a gluon. At next to leading order (NLO), the gluon propagator in figure 2.2(a) may be replaced by the vacuum polarisation diagrams shown in figures 2.2(b)-2.2(d). The first of these diagrams, figure 2.2(b), causes the vacuum to effectively screen colour charge, such that at large distances the strength of the interaction is diminished. This is what happens in QED, and is the reason why

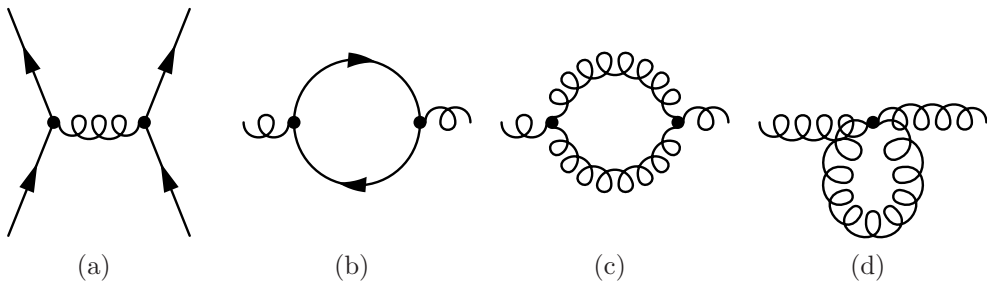


Figure 2.2: tree level $qq\bar{q}q$ scattering, and vacuum polarisation diagrams

the effective coupling constant α_{QED} decreases at higher momenta.

The three and four gluon vertices give rise to the diagrams in figures 2.2(c) and 2.2(d). The gluon loops in these diagrams cause an anti-screening effect, such that the strength of the interaction decreases as the exchanged momentum increases. This is the opposite effect to that seen for the quark loop, however in QCD it is this effect that dominates.

The anti-screening effect is characteristic of $SU(N)$ gauge theories. An $SU(4)$ theory would contain four colours and 15 gluon fields ($N^2 - 1$), increasing the contribution of the gluon loop diagrams in figure?? and thus increasing the anti-screening effect. Conversely, there are only 3 gluon fields in an $SU(2)$ theory (c.f. the three gauge bosons of the weak force), which would result in a smaller anti-screening effect. The screening effect, however, increases with the number of quark fields contained in the theory. For example, in $SU(3)$ gauge theories that contain 17 or more quark flavours, the screening effect is dominant and the strength of the interaction increases as the exchanged momenta increases [?].

2.2.1 Factorisation

Computing the results of a proton-proton collision is complex, as different energy scales are involved in the problem. The momentum exchanged between partons is at the TeV scale for collisions at the LHC, while the physics describing the arrangement of the partons within the proton is determined at a much lower scale, Λ_{QCD} . QCD is a strongly coupled theory at low energies, whereas at higher scales it is weakly coupled

and perturbative methods may be used. Fortunately, factorization allows the physics at these different scales to be separated [?]. The low momentum, nonperturbative physics describing the structure of the proton may be isolated from the high momentum, parton-parton scattering.

The structure of the proton may thus be described using Parton Distribution Functions (PDFs), $q_i(x, Q^2)$, $G(x, Q^2)$, and $\bar{q}_i(x, Q^2)$. The functions $q_i(x, Q^2)$ describe the probability of a probe with momentum Q^2 resolving a quark of flavour i within the proton, with said quark carrying a fraction x of the proton's momentum. Similarly, the distribution functions $\bar{q}_i(x, Q^2)$ and $G(x, Q^2)$ describe the probability of resolving an antiquark or gluon, respectively, within the proton. While a proton is typically thought of as containing two up quarks and one down quark, it also contains a number of gluons. These gluons may decay into quark-antiquark pairs, referred to as "sea" quarks. Because of this, the probabilities of finding antiquarks, or quarks with flavours other than up or down, are non-zero. The number of valence quarks is conserved, however, giving the conditions [?]

$$\int_0^1 dx [q_{\text{up}}(x, Q^2) - \overline{q_{\text{up}}}(x, Q^2)] = 2 \quad (2.6)$$

$$\int_0^1 dx [q_{\text{down}}(x, Q^2) - \overline{q_{\text{down}}}(x, Q^2)] = 1 \quad (2.7)$$

$$\int_0^1 dx [q_j(x, Q^2) - \overline{q_j}(x, Q^2)] = 0 , \quad j \in \{c, s, t, b\} \quad (2.8)$$

While the parton distribution functions must be determined from experiment, the evolution of distribution functions can be calculated in a similar fashion to the coupling constant, α_s . The dependence of the PDFs on Q^2 is given by the Dokshitzer - Gribov - Lipatov - Altarelli - Parisi (DGLAP) equations[?, ?]:

$$\frac{dq_i(x, Q^2)}{d \log Q^2} = \frac{\alpha_s}{2\pi} \int_x^1 \frac{dy}{y} \left[P_{qq}(y) q_i\left(\frac{x}{y}, Q^2\right) + P_{qG}(y) G\left(\frac{x}{y}, Q^2\right) \right] \quad (2.9)$$

$$\frac{d\bar{q}_i(x, Q^2)}{d \log Q^2} = \frac{\alpha_s}{2\pi} \int_x^1 \frac{dy}{y} \left[P_{qq}(y) \bar{q}_i\left(\frac{x}{y}, Q^2\right) + P_{qG}(y) G\left(\frac{x}{y}, Q^2\right) \right] \quad (2.10)$$

$$\begin{aligned} \frac{dG(x, Q^2)}{d \log Q^2} &= \frac{\alpha_s}{2\pi} \int_x^1 \frac{dy}{y} \left[P_{Gq}(y) \sum_i \left(q_i\left(\frac{z}{y}, Q^2\right) + \bar{q}_i\left(\frac{z}{y}, Q^2\right) \right) \right. \\ &\quad \left. + P_{GG}(y) G\left(\frac{x}{y}, Q^2\right) \right], \end{aligned} \quad (2.11)$$

where the P_{xx} are splitting functions. While a probe at Q^2 may resolve a quark or gluon within the proton, a probe with higher momentum may be able to resolve finer structures that are only present for a short time. For example, a given probe may be able to resolve a quark, while a probe with higher momentum may be able to interact with a collinear gluon emitted by this quark (fig 2.3(a)). Similarly, a high momentum probe may be able to resolve a quark or antiquark produced by a gluon (fig 2.3(b)). The splitting function $P_{Gq}(y)$ describes the probability that a gluon will be resolved a quark, carrying a fraction y of the quark momentum. Similarly the function $P_{qq}(y)$ describes the probability of resolving a daughter quark from a parent quark, while the functions $P_{qG}(y)$ and $P_{GG}(y)$ describe the probability of resolving quarks and gluons, respectively, from a parent gluon.

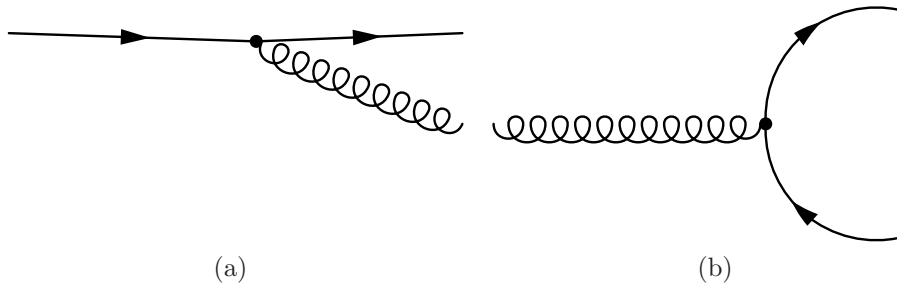


Figure 2.3: processes described by the splitting functions. In figure 2.3(a), a quark emits a collinear gluon. A high momentum probe may be able to resolve the emitted gluon.

The PDFs derived by the CT10 group are plotted in figure 2.4. At small x the gluon

PDF is dominant, and consequently the sea quark contributions are also significant in this regime, whereas the valence quarks dominate at higher values of x .

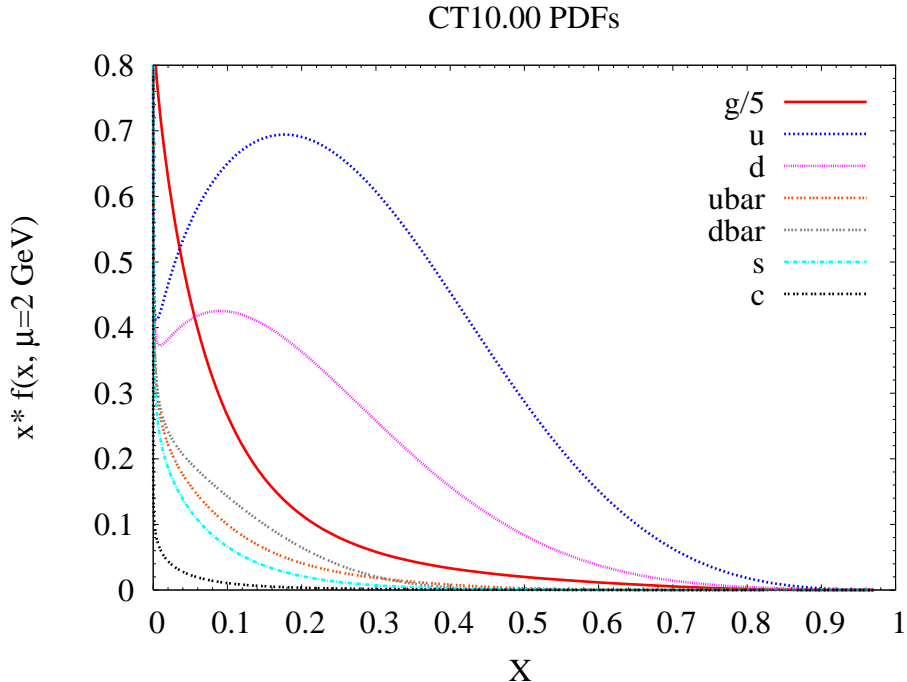


Figure 2.4: CT10 pdfs, obtained at a momentum scale of 2 GeV [12, ?].

2.2.2 Hadronization and Jet Production

Any partons produced in a collision will continue to interact via the colour force. However, the strength of the coupling increases approximately linearly with the separation between these partons: $\alpha_s \sim \sigma r$. This increases the probability that an initial parton will collinearly radiate other partons, in a process referred to as showering. While there may initially be only a few partons produced by the hard scattering, those partons will multiply, evolving into several collimated showers of partons.

These partons will then arrange themselves into hadrons. The confinement hypothesis states that colour charged partons do not exist in isolation, they must be confined within colourless hadrons. All hadrons observed in nature consist of quarks and gluons arranged

in colour singlet (i.e. neutral) states. If a given quark were to be separated from the other constituents in its parent hadron in order to “isolate” it, the energy required to achieve this would increase with the separation distance. At a certain point it becomes energetically favourable for a quark-antiquark pair to be produced from the vacuum, such that the remnants of the parent hadron form a bound state with one member of the new pair, while the separated quark binds with the other member of the pair. It is thus not possible to observe a free quark in isolation, as new hadrons are formed instead using partons created from the vacuum.

Partons created in the collision thus organise themselves into collimated sprays of hadrons, which are referred to as “jets”. The showering and hadronization of particles are non-perturbative processes, and so it is difficult to predict the way in which a parton produced in a collision will evolve into a jet. In ATLAS, jets are defined from energy deposited in the calorimeters using jet finding algorithms, which are discussed in section ???. The experimental measurement of the inclusive jet cross section obtained using 2010 data is discussed in section ??.

Chapter 3

Inclusive Jet Cross Section

3.1 Introduction

The first measurements of the inclusive jet cross section was made in 2010 [?, ?] using 17nb^{-1} of early data. The results described the cross section for production of jets with p_{T} from 60 to 600 GeV and with rapidities less than 2.8 in magnitude. This measurement was repeated in early 2011 using the full 2010 ATLAS dataset (45pb^{-1}) to extend those results, covering jets with p_{T} from 20 GeV to 1.2 TeV. The rapidity range has also been extended into the forward region, to include jets with $|y| < 4.4$. Figure ?? shows the kinematic region covered by the initial measurement compared to that described in this analysis. The dijet mass spectrum has also been measured using 2010 data, and this rapidity coverage of this measurement has been expanded to include the forward region as well.

Section 3.2 describes how jets are defined and calibrated in ATLAS data. The event selection and triggers used for data collection are described in section 3.3, while section 3.4 describes the method used to correct detector resolution effects in the measured data. The treatment of experimental uncertainties is described in section 3.5, and results are presented in section 3.6.

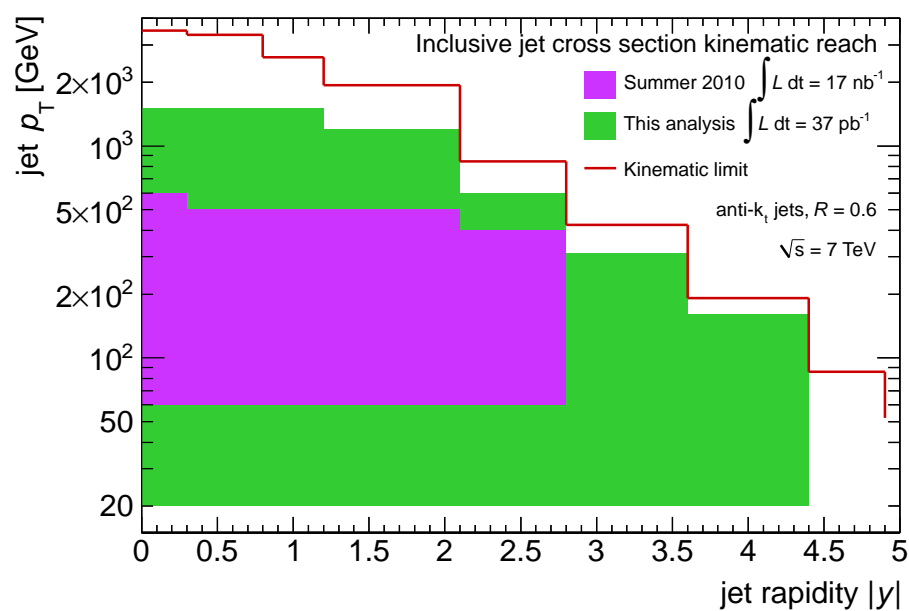


Figure 3.1: Diagram showing the kinematic range covered by the first inclusive jet cross section measurement using 17nb^{-1} (purple) of early data, and that covered when using the full 37pb^{-1} from the 2010 dataset.

3.2 Jets in ATLAS

For the inclusive jet cross section and dijet analyses, jets were reconstructed using the anti- k_t algorithm running on topologically clustered calorimeter cells. The topological and jet clustering algorithms will be described, and then the jet calibration method and the uncertainty on the jet energy scale will be discussed.

3.2.1 Topological Clustering

Topological clusters (or topoclusters) are formed by grouping neighbouring calorimeter cells based on their signal to noise ratio [13]. Cluster seeds are found by searching for calorimeter cells that have an energy greater than some multiple, t_{seed} , of their noise RMS. The noise value used is obtained by adding in quadrature the contributions from electronics noise and pile-up.

Neighbour Cells are added to the cluster provided they are adjacent to the seed cell (or a neighbour cell) and that their signal to noise ratio exceeds the neighbour threshold, $t_{neighbour}$. This is done repeatedly until all neighbour cells are found. Finally, boundary or perimeter cells are added to the cluster by taking all cells that are adjacent to neighbour or seed cells and that have a significance greater than t_{cell} .

Hadronic clusters typically use a “420” scheme, where t_{seed} , $t_{neighbour}$ and t_{cell} have values of 4,2 and 0, respectively. In this case, the signal is defined as the absolute value of the energy deposited in the calorimeter cell when searching for seed and neighbour cells. This ensures that the contribution from noise is handled symmetrically. A high seed threshold makes it unlikely that a cluster will be seeded purely from noise, while a low cell threshold means that low energy cells around the periphery of the shower are still clustered. A “633” scheme is also used in ATLAS to cluster electromagnetic objects, while other schemes have been investigated using testbeam data ([Louise’s thesis](#)) . Topoclusters created using the 420 scheme are used as inputs for the jet algorithms

considered in this analysis.

3.2.2 Jet-Finding Algorithms

The jets considered in this analysis are found using the anti- k_t algorithm [?], with topological clusters used as constituents. The family of k_t -like jet algorithms operate by forming a list of all the constituents in the event. For all constituents and pairs of constituents, the jet resolution quantities

$$d_{ij} = \min(k_{ti}^{2p}, k_{tj}^{2p}) \frac{(y_i - y_j)^2 + (\phi_i - \phi_j)^2}{R^2} \quad (3.1)$$

and

$$d_i = k_{ti}^{2p} \quad (3.2)$$

are computed, where k_{ti} , ϕ_i and y_i are the transverse momentum, azimuthal angle and rapidity of the i th constituent, respectively. The distance parameter R describes the desired size of the jets being sought after, such that found jets will be separated by no less than R in (y, ϕ) -space. The parameter p defines the jet-finding algorithm: $p = 1$ corresponds to the k_t algorithm, $p = -1$ gives the anti- k_t algorithm, and $p = 0$ corresponds to the Cambridge-Aachen cone algorithm.

Once d_{ij} and d_i have been computed, the values are sorted. If the smallest value present corresponds to a d_{ij} , then the i -th and j -th constituents are merged into a proto-jet. This is done by summing their four momenta. The proto-jet is then added to the list of constituents while its components are removed from the list. The d_{ij} and d_i values are then recomputed for all remaining constituents and proto-jets. This process is repeated, with each iteration either adding constituents to an existing proto-jet or merging constituents to form a new proto-jet. In the case where a d_i value is smaller than any d_{ij} value, then this proto-jet is considered a complete, final jet and it is removed from the list. The process continues until the constituent list is empty, with all constituents

having been used to form complete jets.

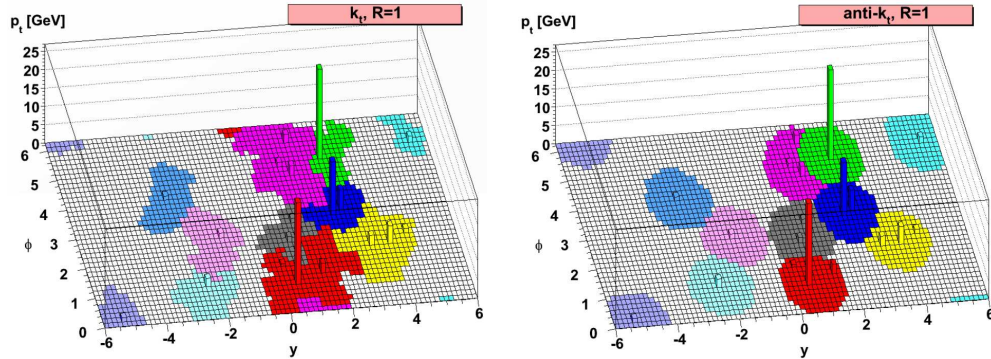


Figure 3.2: jets found by the k_t algorithm (left) and the anti- k_t algorithm (right). The event was generated using HERWIG [?], and contains some soft radiation in addition to the high- p_T constituents

In the k_t algorithm d_{ij} is approximately equal to the relative difference in transverse momentum between the two constituents, in the limit where the angle between the constituents is small. The k_t algorithm thus acts to cluster together constituents with similar momenta, reversing the fragmentation process caused by QCD. However, this procedure clusters constituents with the smallest transverse momenta first, such that high p_T constituents may be clustered around groups of low p_T constituents. This tends to result in jets with irregularly shaped boundaries. Conversely, the anti- k_t algorithm considers the highest p_T constituents first and builds the proto-jets around those, resulting in conically-shaped jets (fig. 3.2(b)). This procedure also means that jets found by the anti- k_t algorithm tend to be less sensitive to the effects of pile-up and the underlying event [?].

The k_t -like jet algorithms are favored because they are both infrared (IR) and collinear safe. IR safety means that the jets found are stable with respect to low p_T constituents arising from pile-up or the underlying event (fig ??). For an algorithm to be IR safe, the presence of soft particles can not “confuse” the algorithm into mistaking two separate jets for a single large jet if there is some soft radiation between them (fig. 3.4). Collinear safety requires that the algorithm will still find a jet if, for instance, a single high- p_T constituent

is replaced by two (or more) close together constituents with lower p_T (fig 3.3). The k_t -like algorithms have these properties, whereas more iterative cone algorithms tend not to.

3.2.3 Jet Energy Scale Calibration

Once a jet has been defined, its energy must be calibrated to the Jet Energy Scale (JES). This is done through an “EM+JES” scheme, whereby the EM scale energy of the jet is multiplied by a correcting factor to obtain the energy at the JES. The calibration is derived from Monte Carlo using a numerical inversion process. This calibration accounts for the following effects:

- non-compensation of the calorimeter, i.e. the energy is calibrated to the hadronic scale.
- energy deposited in inactive (dead) regions of the detector
- leakage effects from particle showers not fully contained in the calorimeters
- particles contained in the truth jet but not in the reco jet
- energy from showering particles that is not collected by the topoclustering algorithm. (out of cluster corrections).

The calibration is done in three steps. First, the EM scale energy of the jet is adjusted in order to correct for pile-up effects. Additional proton-proton interactions from the same event can deposit energy in the calorimeter, effecting the energy of the high p_T objects from the hard scattering. Minimum bias data is used to determine the average energy deposited in the calorimeter as a function of pseudorapidity and the number of primary vertices reconstructed from the event. This information is used to subtract the average EM scale energy added to the jet as a result of pileup.

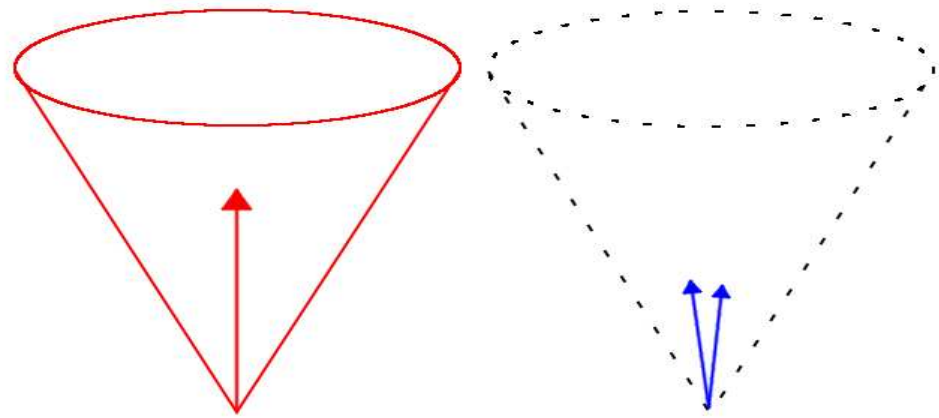


Figure 3.3: An example of an algorithm which is not collinear safe. On the left, a jet is found around a single high- p_T constituent. On the right, the single constituent is replaced by two, each with half the p_T of the original. In this case, the algorithm fails to find a jet.

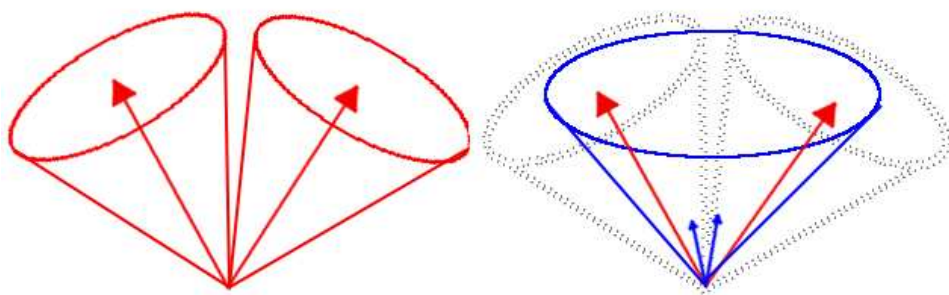


Figure 3.4: example of a jet algorithm which is not IR safe. In the figure on the left, two distinct jets are found around the high- p_T constituents. In the presence of soft radiation (right), The algorithm finds only a single jet.

The second step is to correct the kinematics of the jet, still at the EM scale, based on the location of the hard scattering. The vertex with the highest sum of squared transverse momenta from tracks ($\sum p_{T,track}^2$) is taken as the position of the hard scatter, and all jet kinematic quantities (p_T, y, ϕ , etc) are recomputed using this vertex as the origin.

Finally, the JES correction is applied. The correction is derived exclusively from Monte Carlo, using samples generated without the inclusion of pile-up. An event generator is used to simulate a hard parton-parton scattering typical of proton-proton collisions, which outputs a set of final state particles and their four momenta. Geant 4 is then used to simulate the interaction of these particles with the detector. The event is then reconstructed using the same methods that are used for the data: calorimeter cells are reconstructed and used to form topological clusters, on which jet finding algorithms are run. Truth jets are formed by running the jet finding algorithms on the final state particles output by the event generator.

The calibration is derived by comparing the jets reconstructed from the (simulated) calorimeter information to the truth jets. A reconstructed jet is matched to a truth jet if the distance between them is less than 0.3 in (y, ϕ) . Only isolated jets are matched: a reconstructed/truth jet must have no other jets with $p_{T,EM} > 7\text{GeV}$ within $2.5R$, or it is not used in the derivation of the calibration.

The matched reconstructed-truth jet pairs are then used to define the response R , such that

$$R = \frac{E_{\text{reco}}^{\text{EM}}}{E_{\text{truth}}}, \quad (3.3)$$

where $E_{\text{reco}}^{\text{EM}}$ is the EM scale energy of the reconstructed jet and E_{truth} is the energy of the truth jet. The response is binned in E_{truth} and η_{det} , the pseudorapidity of the reconstructed jet at the EM scale. For each $(E_{\text{truth}}, \eta_{\text{det}})$ bin, the mean reconstructed jet energy, $\langle E_{\text{reco}}^{\text{EM}} \rangle$, is found, and a gaussian fit is used to extract the mean response, $\langle R \rangle$.

The response is then parameterized as a function of $E_{\text{reco}}^{\text{EM}}$ for each η_{det} bin. For the k -th η_{det} bin, a fit is performed on the $(\langle E_{\text{reco}}^{\text{EM}} \rangle, \langle R \rangle)$ points obtained from each E_{truth} bin.

The fitted function is of the form

$$F_{\text{calib},k}(E_{\text{reco}}^{\text{EM}}) = \sum_{j=0}^{N_{\text{max}}} a_j (\log E_{\text{reco}}^{\text{EM}})^j, \quad (3.4)$$

where the a_j are free parameters and N_{max} is an integer between 1 and 6 chosen to maximize the goodness of fit.

The correction factor is then found by inverting $F_{\text{calib},k}$, so the final EM+JES energy of a jet lying in the k -th η_{det} bin is given by

$$E_{\text{reco}}^{\text{JES}} = \frac{E_{\text{reco}}^{\text{EM}}}{F_{\text{calib},k}(E_{\text{reco}}^{\text{EM}})}. \quad (3.5)$$

3.2.4 JES uncertainty

The systematic uncertainty on the JES is an important quantity, and one of the dominant sources of uncertainty in this analysis. There are several sources that contribute to this uncertainty, outlined below:

- **Uncertainty from the calibration method** The method assumes that all jet constituents require the same average correction. Additionally, the same correction factor is used for both the energy and transverse momenta of the jet, which may bias the calibrated p_T in cases where the calibrated jet mass differs from the mass of the truth jet. The uncertainty arising from the calibration method is estimated by comparing the reconstructed jets at the EM+JES scale to their truth jet counterparts. The responses $\langle RE \rangle = \langle E_{\text{reco}}^{\text{EM+JES}} / E_{\text{truth}} \rangle$ and $\langle R_P \rangle = \langle p_T, \text{reco}^{\text{EM+JES}} / p_{T,\text{truth}} \rangle$ are computed, and binned in terms of $p_T, \text{reco}^{\text{EM+JES}}$. Any deviation of $\langle RE \rangle$ or $\langle R_P \rangle$ from unity suggests that the kinematics of the reconstructed jets after calibration are not equal to those of the truth level jets, for the reasons mentioned above. The uncertainty assigned to the calibration method is taken as the largest deviation of $\langle RE \rangle$ or $\langle R_P \rangle$ from unity, and is found to be less than 1% for

$$p_T, reco^{EM+JES} > 30GeV.$$

- **Uncertainty from calorimeter response** The contribution to the JES systematic from the uncertainty in the calorimeter response is derived from single particle measurements. The uncertainty in the response to charged hadrons is measured in E/p studies [?] and in testbeam data [?]. The simulation framework allows the particles in the truth jet to be associated with the energy they deposit in the calorimeter, and thus the single particle response uncertainties can be propagated to obtain an uncertainty for the response of the jet. When estimating this uncertainty, effects relating to the calorimeter acceptance, charged particles with $E > 400GeV$, and energy deposited by neutral hadrons are also considered. Effects related to the calorimeter response are found to contribute a 1.5% – 4% uncertainty to the JES systematic.
- **Uncertainty from noise thresholds in detector simulation** The noise present in the calorimeter electronics can change over time, whereas the noise used in the simulation is fixed when the MC sample is generated. The effect of the noise threshold in the simulation was measured by increasing the noise thresholds for the topoclustering algorithm by amounts of 5-10%. This influences which cells are grouped into topoclusters, and thus contribute energy to the jet. The uncertainty assigned to this effect was found to be negligible for jets with $p_T > 45GeV$, and is estimated as 1-2% for jets with lower p_T .
- **Effect of additional material in simulation** As the JES calibration is intended to correct for the effects of inactive material, it is sensitive to the material description of the detector in the simulation. The effects of this were estimated by adding additional material to the simulation geometry in several places, and comparing the response obtained with the modified geometry to that obtained using the nominal geometry.

- **MC event generators** The nominal MC sample used in the derivation of the JES was generated using PYTHIA, using the AMBT1 tune. Samples were also produced using ALPGEN interfaced with HERWIG and JIMMY, and using the perugia 2010 tune in PYTHIA. The ALPGEN sample used the CTEQ6.1 pdfset, and treated parton showering and hadronization effects differently to the nominal PYTHIA sample, whereas the perugia2010 sample provided a different treatment of the underlying event. Deviations between the response obtained from the perugia2010 and ALPGEN +HERWIG +JIMMY samples with respect to the nominal PYTHIA sample were used to estimate the uncertainty arising from the choice of theoretical physics models.
- **Relative calibration of uncertainties between forward and central regions.** Contributions to the JES uncertainty from the above sources have been calculated in the central region, $0.3 < |\eta| < 0.8$. This uncertainty is used as a baseline, and an intercalibration method [?] is used to extend the estimate of the JES systematic into other pseudorapidity regions. This method uses a p_T balancing technique applied to dijet events in order to obtain the ratio of the calibrated jet responses in different regions of pseudorapidity. This response was calculated for data and simulation, using several different MC event generators. The RMS of the differences in response between MC and data is then added in quadrature to the baseline uncertainty, yielding the uncertainty in higher pseudorapidity regions.

The total JES uncertainty, and its components, are plotted in figures 3.5 and 3.6. The dominant contribution in the central region ($0.3 < |\eta| < 0.8$) is from the uncertainty in the calorimeter response. In other pseudorapidity regions the intercalibration uncertainty dominates at low p_T .

3.2.5 Jet Selection

After Jets have been calibrated, there are some criteria that they need to meet before being included in the analysis. Certain detector issues were capable of causing a jet to be reconstructed even if there were no physical particles depositing energy in that region of the calorimeter. Jet cleaning cuts were made to address these issues, and remove from the analysis as many “fake” jets as possible. The jet cleaning cuts, and the problems they are intended to address, are listed below

- **Coherent noise in the EM calorimeter** Jets with $|\eta| < 2.8$ were rejected if EM_f , the fraction of energy deposited in the EM calorimeter, exceeded 0.9 while the LAr quality variable exceeded 0.8. The LAr quality refers to the fraction of LAr cells in the jet which have a pulse shape significantly different to a reference shape.
- **Noise bursts (“spikes”) in the HEC** Jets were rejected if the fraction of energy deposited in the HEC was greater than $1 - HECQ$, where $HECQ$ is the HEC quality variable and is defined analogously to the LAr quality variable. Jets were also rejected if the sum of negative energy cells exceeded 60 GeV in magnitude.
- **cosmics/beam background** Jets were rejected if the average timing for jet cells was greater than 10ns from the average event time. For jets with $|\eta| < 2.0$, tracking information can be used to define the charged fraction, Chf , which is the fraction of the jet p_T associated with tracks in the inner detector. In this case, Jets were rejected if the charge fraction were less than 0.1 and the EM fraction was less than 0.05, if the EM fraction exceeded 0.95 while the charge fraction was less than 0.05, or if 99% of the jet energy was deposited in a single layer of the calorimeter. Jets with $|\eta| > 2.0$ were rejected if the EM fraction was less than 0.05.

Jets which failed these cleaning cuts were not included in the analysis.

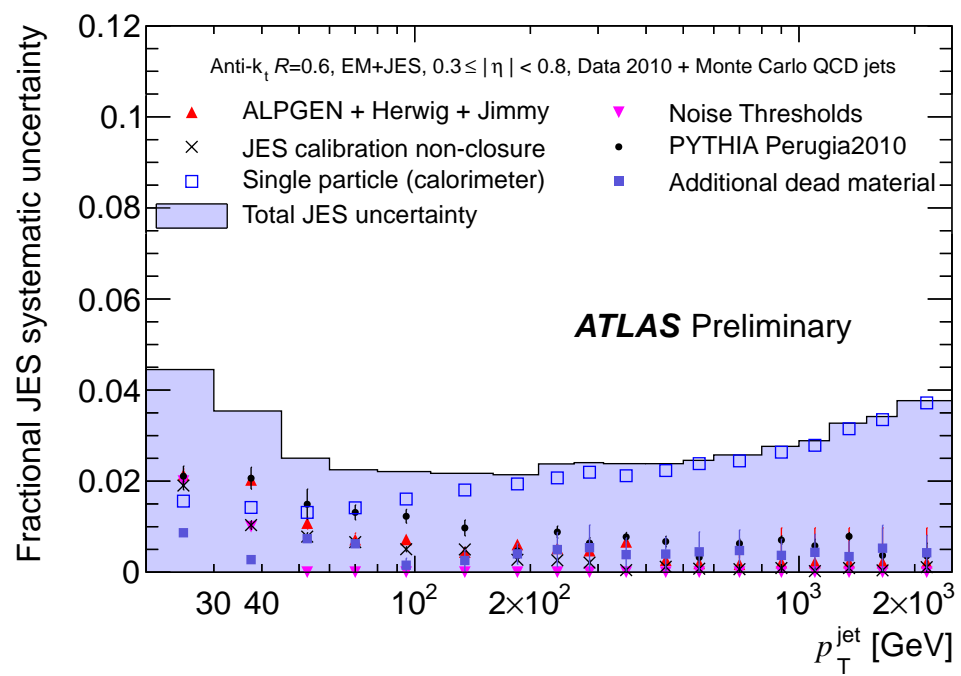


Figure 3.5: JES uncertainty in the central barrel region ($0.3 < |\eta| < 0.8$)

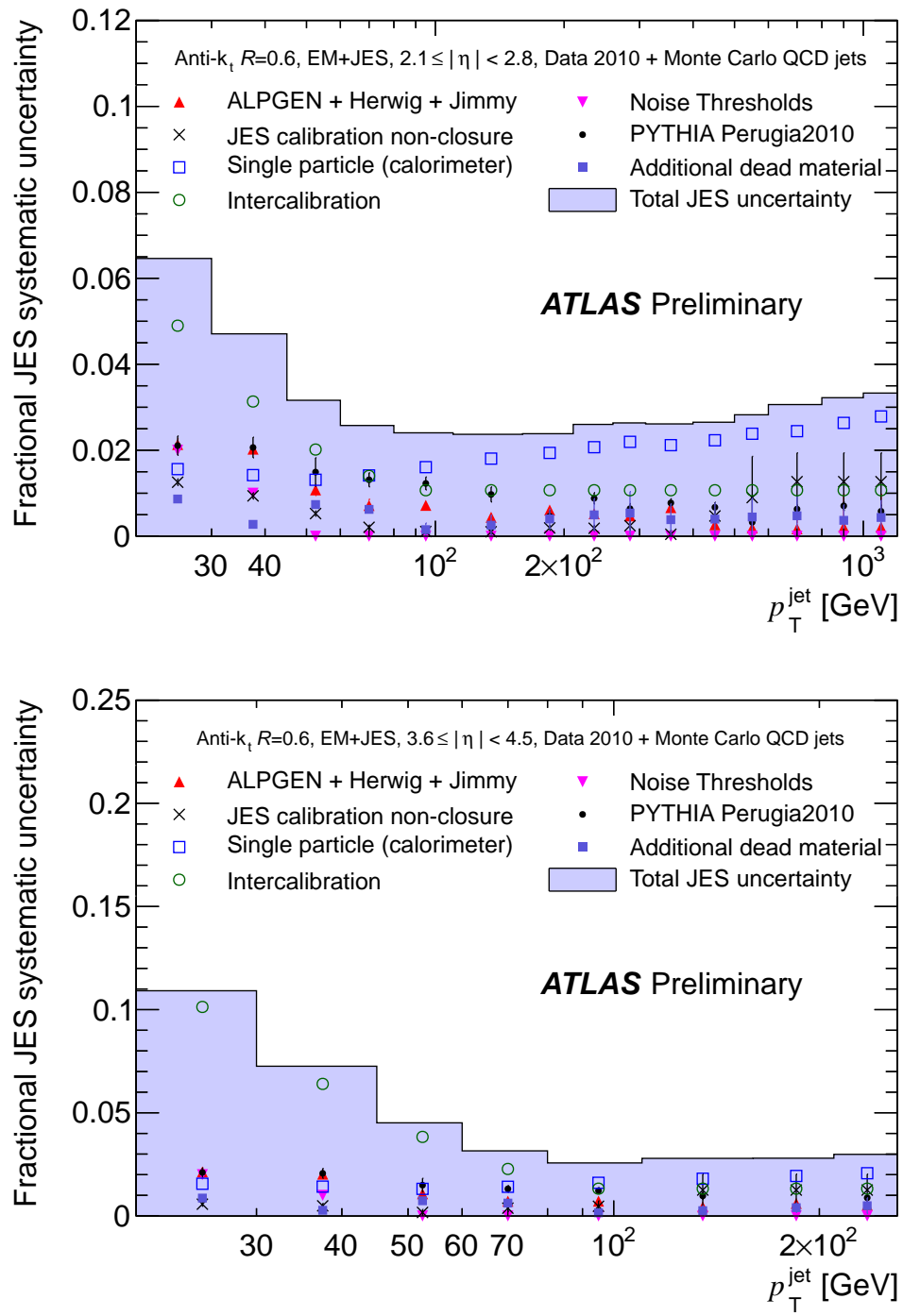


Figure 3.6: JES uncertainty for the end-cap ($2.1 < |\eta| < 2.8$) and FCal ($3.1 < |\eta| < 4.5$). At low p_T , the intercalibration provides the dominant source of uncertainty.

3.3 Event Selection and Data quality

In order for an event to be considered in the inclusive jet cross section analysis, data quality flags for the event needed to be green. The event was also required to have a primary vertex with at least 5 tracks. Each p_T -rapidity bin in the inclusive analysis was associated with a trigger. An event only contributed jets to a given p_T - y bin if the trigger threshold associated with that bin is passed.

The same criteria were used for the dijet mass spectrum analysis, with the addition that leading jet in the event was required to have $p_T > 30$ GeV, while the subleading jet was required to have $p_T > 20$ GeV.

3.3.1 Triggers used for the inclusive jet analysis

The cross section measurement is divided into 7 bins of rapidity and 16 bins of p_T . A dedicated, fully efficient trigger is used to collect jets in each bin in order to maximize statistics. The three lowest p_T bins are filled using data taken from the MBTS1 (minimum bias) trigger. Minimum bias data from only the three earliest periods of running (A-C) was used for this purpose, as in these periods the trigger had a lower prescale (and so collected more data) and there was a minimal amount of pile-up. At higher p_T (above 60 GeV), data is taken using the central jet trigger for jets with $|y| < 2.8$. The rapidity bin from $2.8 < |y| < 3.6$ is referred to as the “transition bin”, as it covers the transition region between the end cap calorimeters and the FCal (figure 3.7). In this region both the central and forward jet triggers are used, whereas in the forward region ($3.6 < |y| < 4.4$) only the forward jet trigger is used. The behaviour of the jet trigger system needs to be understood before they can be used effectively. This is achieved by measuring the trigger efficiency. The inclusive efficiency of a trigger is defined as

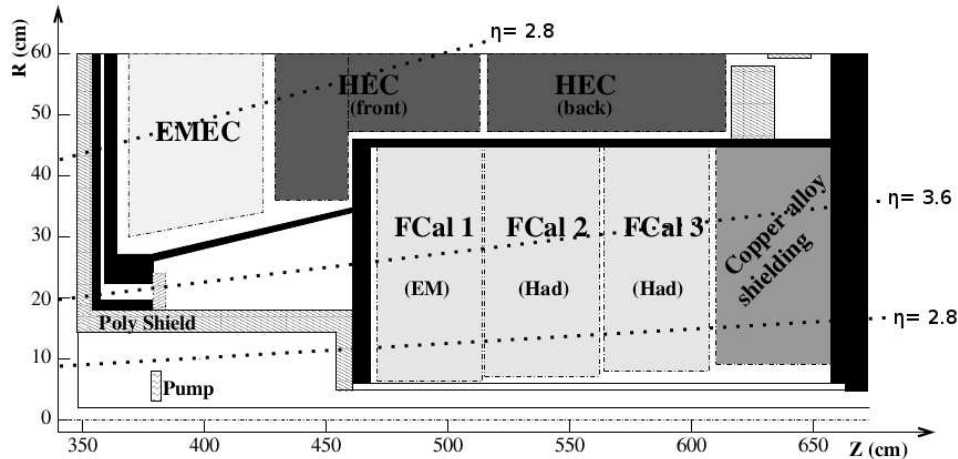


Figure 3.7: diagram showing cross section of part of an end-cap in ATLAS. The forward bin corresponds approximately to the region $2.8 < |\eta| < 3.6$, and is completely contained within the FCal. The transition bin covers the area between $|\eta| = 2.8$ and $|\eta| = 3.6$, which is partially occupied by both the end-cap calorimeters and the FCal.

$$\epsilon_{inc} = \frac{N_{triggered}}{N_{reference}}, \quad (3.6)$$

where $N_{reference}$ is the total number of jets reconstructed offline from a reference sample, and $N_{triggered}$ is the number of reconstructed jets coming from events in the reference sample which pass the trigger condition. This efficiency is then binned in the p_T of the reconstructed jets to produce a turn-on curve. Trigger efficiencies for the transition and forward bins are plotted in figures 3.8 and 3.9, respectively.

The plateau point is defined by integrating bins of $N_{triggered}$ and $N_{reference}$ from high p_T towards low p_T , until reaching the point where the ratio of these sums drops below 99%. The high edge of this bin is then taken as the plateau point, as the trigger is at least 99% efficient at p_T 's higher than this value. Above the plateau point the trigger is assumed to be fully efficient, and is used to collect data for the appropriate p_T bins.

While studying the forward jet triggers, it was observed that events containing high p_T jets in the region $x < y < z$ and $x < \phi < z$ were not being selected by the trigger. The L1 trigger tower in this region was producing very little signal, and was effectively

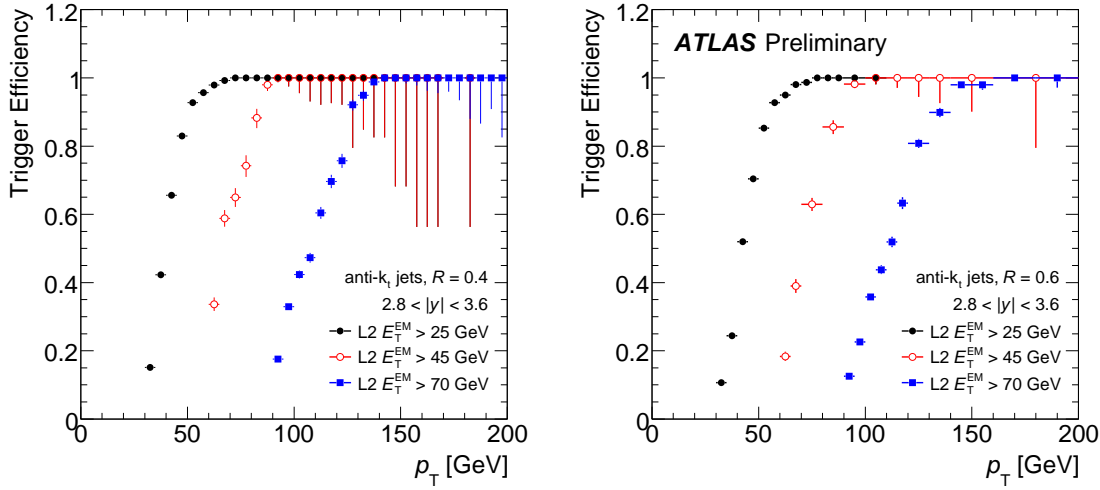


Figure 3.8: Efficiencies for L2 triggers in the transition bin, for anti- k_t jets with $R=0.4$ (left) and $R=0.6$ (right).

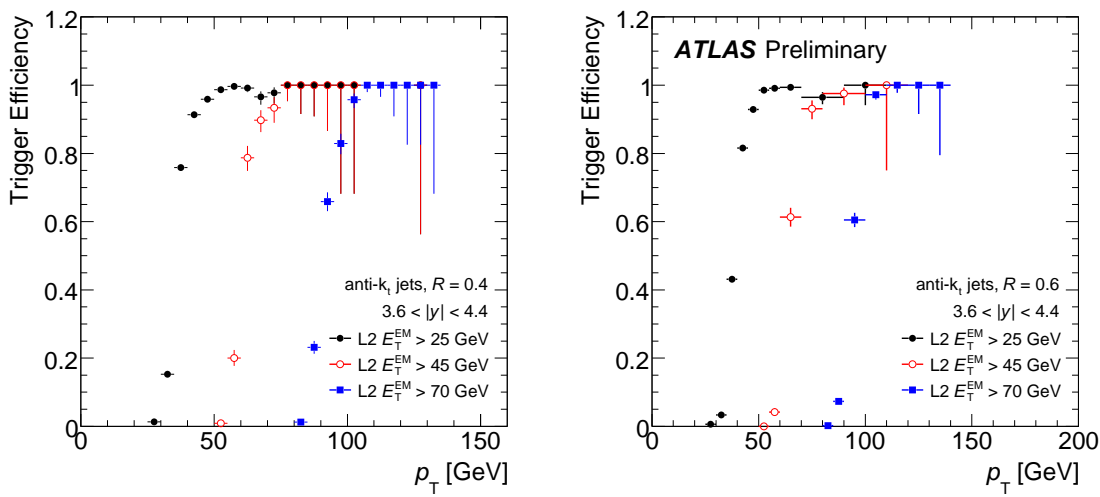


Figure 3.9: Efficiencies for L2 triggers in the forward bin, for anti- k_t jets with $R=0.4$ (left) and $R=0.6$ (right).

dead. This reduced the geometrical acceptance of the forward jet trigger by $\frac{1}{128}$, which is corrected for in the cross section calculation. Consequently, the plateau points in the forward and transition bins are defined at an efficiency of 98%. It should be noted that while the trigger tower is considered dead, calorimeter cells (and hence jet reconstruction) are unaffected in this region.

As data taking progressed, the trigger system was commissioned further. The forward jet triggers were commissioned after run **1561127** (period E5), and used to collect data in the forward and transition regions from then on. The HLT system was commissioned from period G on, which allowed event rejection to occur at L2. The EF remained in pass-through mode throughout the remainder of 2010, and so all events passing at L2 were recorded. Triggers at L1 were used to collect data until the HLT was commissioned, after which L2 triggers were used.

3.3.2 Transition Bin

The transition bin covers the region between end cap calorimeters and the FCal. Information from the EMEC and HEC is only used by the central jet trigger, while information from the FCal is only used by the forward jet trigger. In order for the analysis to be sensitive to all jets in this region of rapidity, both the central and forward jet triggers need to be considered when collecting data. This is done by taking the logical “OR” of the two triggers, such that jets in the event are counted if either the central or forward trigger condition is met. The efficiency of each trigger through this rapidity range is shown in figure 3.10.

When only a single trigger is used, the measured cross section is given by

$$\sigma = N_{jets} \left(\sum_i \frac{\mathcal{L}_i}{S_i} \right)^{-1}, \quad (3.7)$$

where N_{jets} is the number of jets observed and \mathcal{L}_i and S_i are the integrated luminosity and

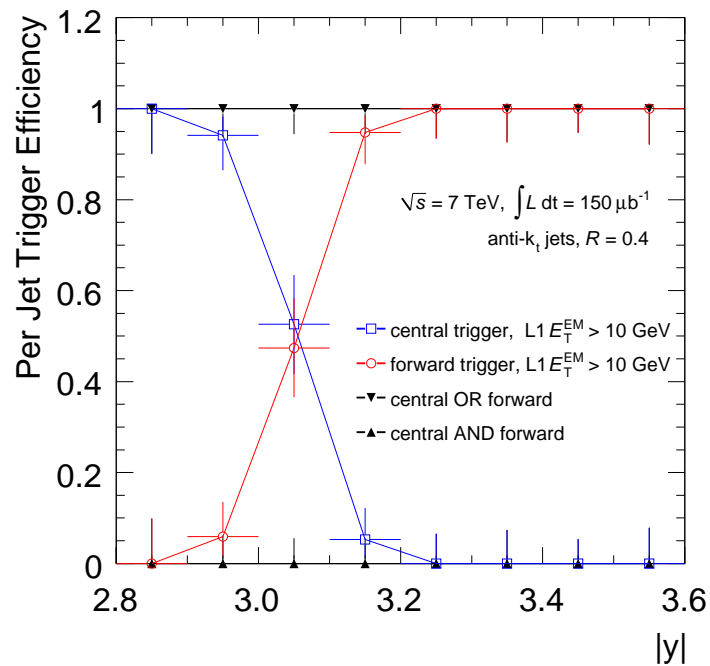


Figure 3.10: Efficiency of Level 1 forward (red) and central (blue) triggers as a function of offline jet rapidity for jets with p_T greater than 45 GeV in the transition bin ($2.8 < |y| < 3.6$). Note that the OR of these remains fully efficient throughout the rapidity range.

trigger prescale for the i th luminosity block, respectively. . The situation is more complex in the case where two (or more) triggers are collecting data. In this situation we classify events as belonging to one of three classes, based on whether the event passed the forward trigger condition but not the central (case 10), the central trigger condition but not the forward (case 01), or both trigger conditions (case 11). When making these distinctions, it is important to consider whether the event satisfied a trigger condition before the prescale was applied, as events should be classified according to the triggers that they could potentially be accepted by rather than the triggers which actually recorded the event. For L1 triggers the “Trigger Before Prescale” flag can be checked in **Athena**, but for L2 triggers the jets found at L2 must be checked to see if any exceed the trigger threshold.

Once the events have been divided into their respective classes, the cross section may be written as

$$\sigma = \frac{N_{01}}{\mathcal{L}_{01}} + \frac{N_{10}}{\mathcal{L}_{10}} + \frac{N_{11}}{\mathcal{L}_{11}}, \quad (3.8)$$

where integrated luminosities are given by

$$\mathcal{L}_{01} = \sum_i \frac{\mathcal{L}_i}{S_{i,01}} \quad (3.9)$$

$$\mathcal{L}_{10} = \sum_i \frac{\mathcal{L}_i}{S_{i,10}} \quad (3.10)$$

$$\mathcal{L}_{11} = \sum_i \frac{\mathcal{L}_i (S_{i,01} + S_{i,10} - 1)}{S_{i,01} S_{i,10}} \quad (3.11)$$

and $S_{i,10}$ ($S_{i,01}$) is the prescale of the forward (central) jet trigger for the i th lumi-block.

3.3.3 Dijet Triggers

For the initial measurements made using data from ATLAS [?, ?] the dijet mass spectrum was binned in terms of the dijet mass, m_{12} , and the maximum rapidity of the two jets, $y_{max} = \max(|y_1|, |y_2|)$. Dijet events were selected by triggering on the leading jet, using

the same trigger thresholds as for inclusive analysis. These first measurements only considered cases where both jets were in the central region, with $y_{max} < 2.8$.

When the dijet analysis was extended to cover the transition and forward regions, a new trigger scheme was considered. The intent was to bin the trigger efficiency in terms of the observables of interest. The central jet trigger would be used for $y_{max} < 2.8$, the forward jet trigger for $3.6 < y_{max} < 4.4$, and the OR of the two for $2.8 < y_{max} < 3.6$, with the trigger efficiency being described by a turn-on curve in m_{12} . Each trigger could then be considered fully efficient above some threshold value for the dijet mass, and used to collect data above this point. This trigger scheme was later abandoned, as the trigger system is based on jet p_T and thus inflates the minimum dijet mass at which the trigger becomes unbiased. Consider the case where both jets in the dijet system have transverse momenta well above the trigger threshold, but the separation between jets is small. The small separation between jets will yield a small mass, and the trigger will efficiently accept dijet events in this configuration. However, in cases where the separation between jets is large and the jet momenta are close to the trigger threshold, the resulting value for the dijet mass can still be quite large while the trigger is not fully efficient.

For this reason, the observables of interest were changed to the dijet mass and the jet separation, $y^* = |y_1 - y_2|/2$. The trigger scheme then reverted back to that used for earlier versions of the analysis wherein the leading jet is used to trigger the event, although this was extended to cover the forward region. The L1 trigger efficiencies for dijet events are plotted as a function of the leading jet p_T in figures 3.11 and 3.12, for the transition bin and forward bin respectively.

It was then expanded to consider the subleading jet, utilizing a method similar to what was done for the transition bin in the inclusive analysis. The kinematic region is divided into a number of bins in p_T and rapidity, each of which is associated with a trigger threshold. Events are then divided into categories based on whether the trigger condition associated with the leading jet was met, or that for the the subleading jet, or

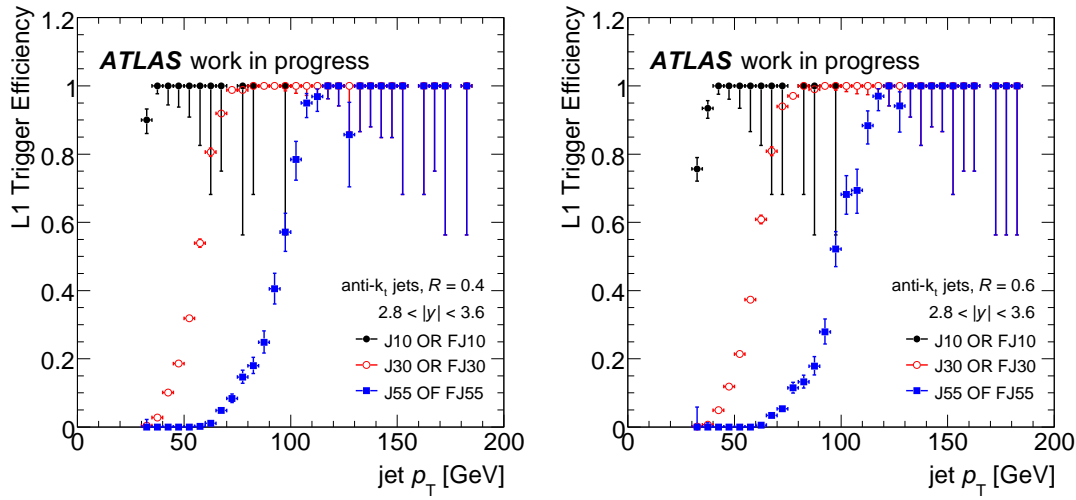


Figure 3.11: L1 trigger efficiencies for dijet events in which the leading jet lies in the transition bin, for anti- k_t jets with $R = 0.4$ (left) and $R = 0.6$ (right).

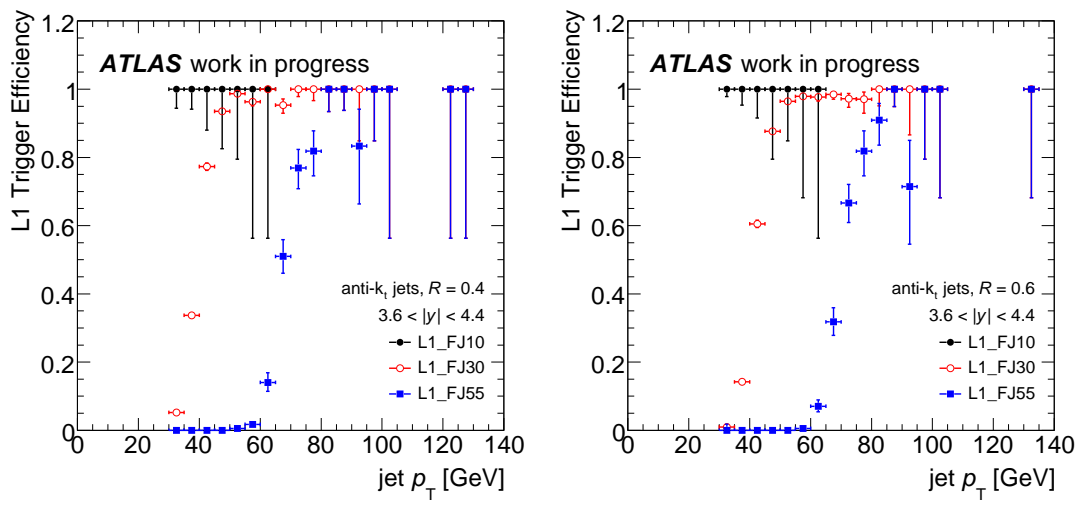


Figure 3.12: L1 trigger efficiencies for dijet events in which the leading jet lies in the forward bin, for anti- k_t jets with $R = 0.4$ (left) and $R = 0.6$ (right).

if both trigger conditions were satisfied. As there is some overlap between the forward and central jet triggers in the region $3.0 < |y| < 3.2$ (fig 3.10), jets in this region are matched to ROI words at L1 or trigger jets at L2 in order to determine whether the jet should be associated with forward or central trigger. Events are then weighted based on the prescales of the triggers, using a generalized version of the method described in section 3.3.2, in order to account for the larger number of trigger categories.

3.4 Data Correction

after cross section calculations are carried out in section above, data needs to be corrected in order to account for (acceptance) and detector effects. As the jet cross section falls sharply with p_T , the non-zero resolution of the detector causes the measured spectrum to be skewed towards higher p_T from the “true” spectrum. Monte Carlo may be used to compare the p_T of truth jets with reconstructed jets in order to understand the effects of the detector resolution. These effects can then be “unfolded” from the measured spectrum in order to obtain results particle level results from data.

The transfer matrix, A_{ij} , may be derived from Monte Carlo, whereby the entry A_{ij} is the number of truth jets in the j -th p_T bin which are then reconstructed in the i -th p_T bin. The transfer matrix describes the influence that detector effects have on the measured results, and must be derived from simulation. This may be normalized to produce the folding matrix of probabilities, P_{ij} , given by

$$P_{ij} = \frac{A_{ij}}{\sum_{k=0}^{N_b} A_{kj}} \quad (3.12)$$

The spectrum at truth level, t_j , and the reconstructed spectrum r_j , are then related by

$$r_j = \sum_{k=0}^{N_b} P_{jk} t_k. \quad (3.13)$$

An unfolded result, u_j , may then be obtained from the measured data d_j , by solving the matrix equation

$$d_j = \sum_{k=0}^{N_b} P_{jk} u_k. \quad (3.14)$$

The solution to this may be found by inverting P_{ij} , such that $u_j = \sum_k P_{ik}^{-1} d_k$. However, this is undesirable as it yields large fluctuations in u_j [?]. Transfer matrices tend to have large condition numbers, meaning that the solution is sensitive to slight changes in the input. Small variations in d_j , which may be due to statistical fluctuations, can produce large spurious fluctuations in u_j .

In order to avoid this, the unfolding method must incorporate some form of regularization. Typically equation 3.14 is solved numerically, and regularization may be done, for example, by incorporating the smoothness of u_j into the optimization method [?]. In this analysis, the unfolding is carried out using the Iterative, Dynamically Stabilized (IDS) method [?, ?].

3.4.1 IDS method

In the IDS method, the MC is re-weighted at each iteration such that the reconstructed MC spectrum is brought closer to that of the measured data, with the truth level spectrum and the transfer matrix adjusted accordingly. As the reconstructed MC is brought closer to the measured data spectrum through re-weighting, the truth level spectrum approaches the desired unfolded result. For features present in the measured data which were not simulated by the MC, the difference between data and reconstructed MC is then unfolded.

Regularization is implemented through the use of a regularization function, $f(\Delta x, \sigma, \lambda)$. This function determines how much unfolding should be done at a given iteration based on the difference between data and Monte Carlo, Δx , the uncertainty in this difference, σ , and the regularization parameter λ . The regularization function should take the ratio $\Delta x/\sigma\lambda$ as an argument, and return a value near zero at small values of this argument

and approach one at higher values.

As the regularization function depends on the difference between data and Monte Carlo, it is important that the Monte Carlo be normalized appropriately. The discrepancy is defined as

$$\Delta d_k = d_k - \frac{N_{\text{dSmc}}}{N_{\text{MC}}} r_k \quad (3.15)$$

where N_{MC} is the total number of jets in the MC sample and N_{dSmc} is the number of jets in data corresponding to structures which are simulated in the MC. Normalizing the MC in this way enables the unfolding to preserve features in the data, such as new physics signals, which were not simulated in the MC, while correctly scaling the MC in regions where it has a similar shape to the data. The total number of jets in the data sample may be taken as an initial estimate for N_{dSmc} . A better estimate may then be obtained using

$$N'_{\text{dSmc}} = N_{\text{dSmc}} + \sum_{k=1}^{N_B} (1 - f(\Delta d, \sigma, \lambda)) \Delta d_k. \quad (3.16)$$

This procedure may be repeated until the relative change in N_{dSmc} is less than a desired threshold.

3.4.2 Matching Efficiency

In order to obtain the transfer matrix from the Monte Carlo, reconstructed jets need to be matched with a corresponding truth jet. Jets are matched if they lie within a distance $\Delta R < 0.3$ in $y - \phi$ space. The spectrum of matched truth (or reconstructed) jets may be obtained by projecting the transfer matrix on the appropriate axis. The matched spectrum may then be compared to the unmatched spectrum to obtain the matching efficiency for truth jets and for reconstructed jets. As the transfer matrix is derived using only matched pairs of jets, the effect of the matching efficiency should be taken into consideration. Prior to the unfolding the measured data is multiplied by the

matching efficiency for reconstructed jets, and after unfolding the result is divided by the matching efficiency for truth jets.

An initial unfolding may then be performed on the data, yielding the result

$$u_j = t_j \cdot \frac{N_{\text{dSmc}}}{N_{\text{MC}}} + [1 - f(\Delta d_k, \sigma d_k, \lambda_M)] \cdot \Delta d_j + \sum_{k=1}^{N_B} f(\Delta d_k, \sigma d_k, \lambda_M) \cdot \tilde{P}_{kj} \cdot \Delta d_k \quad (3.17)$$

where the unfolding matrix \tilde{P}_{ij} is obtained from the transfer matrix:

$$\tilde{P}_{ij} = \frac{A_{ij}}{\sum_{k=0}^{N_b} A_{ik}} \quad (3.18)$$

The regularization functions determine how much unfolding is done in a given bin, based on the regularization parameter λ and significance of Δd_k . Only the difference between measured data and reconstructed MC is unfolded: In bins where Δd_k is small the unfolded result is dominated by the truth level MC spectrum. In those bins where the discrepancy is significant, the regularization parameter λ determines how much unfolding is carried out. As λ increases, less unfolding is performed on the data.

Once an initial estimate of u_j has been obtained, this may be used to re-weight the MC at truth level, and thus improve the transfer matrix. The updated transfer matrix is given by

$$A'_{ij} = A_{ij} + f(|\Delta u_j|, \sigma u_j, \lambda_M) \cdot \frac{N_{\text{MC}}}{N_{\text{dSmc}}} \cdot P_{ij} \cdot \Delta u_j, \quad (3.19)$$

where

$$\Delta u_j = u_j - \frac{N_{\text{dSmc}}}{N_{\text{MC}}} \cdot t_j. \quad (3.20)$$

The new transfer matrix can then be used to update the folding and unfolding matrices, P_{ij} and \tilde{P}_{ij} .

The procedure may then be carried out iteratively in the following sequence

- Update the normalization factor N_{dSmc} , according to 3.16.

- Perform the unfolding.
- Use the unfolded data to update the transfer matrix, and the folding/unfolding matrices.

3.5 Treatment of uncertainties

3.5.1 Statistical uncertainties

The statistical uncertainties on the final (unfolded) cross section measurement are obtained through “toy” Monte Carlos. For each toy, Poisson fluctuations are applied to the measured data spectrum and to the transfer matrix. The fluctuated data is then unfolded using the fluctuated transfer matrix. The unfolded spectra from the toys are then used to compute a covariance matrix, from which the statistical uncertainty on the unfolded data is taken.

3.5.2 Systematic Uncertainties

The JES uncertainty is the dominant source of systematic uncertainty. Its effect on the final cross section result is found by propagating each of the JES components listed in section 3.2.4 through the unfolding procedure. For each component, the measured data spectrum is shifted up and down in p_T by one standard deviation. The shifted spectra are then unfolded, and the uncertainty associated with that component is taken as the difference between the shifted and unshifted spectra, after unfolding.

The effect of the jet energy resolution (JER) uncertainty is also propagated through the unfolding. A modified Monte Carlo sample is produced by smearing the p_T of the reconstructed jets in the nominal MC sample. The reconstructed jets have their p_T smeared by a factor Δ , where Δ is a random variable with standard deviation σ_Δ and a

mean of one. The standard deviation of Δ is chosen to satisfy

$$\sigma_\Delta^2 + \sigma_{\text{nom}}^2 = (\sigma_{\text{nom}} + \sigma_{\text{JER}})^2, \quad (3.21)$$

where σ_{nom} is the nominal JER and σ_{JER} is its uncertainty. The additional smearing is thus applied in such a way as to increase the effective JER by one standard deviation. The data is then unfolded using the modified transfer matrix, and the difference between this result and that unfolded with the nominal transfer matrix is taken as the systematic uncertainty.

The matching between truth and reconstructed jets is another source of systematic uncertainty. As mentioned earlier, the transfer matrix is constructed by matching truth and reconstructed jets within $\Delta R < 0.3$ in rapidity and azimuthal angle. Transfer matrices are also constructed by matching jets within $\Delta R < 0.4$ and $\Delta R < 0.2$. The unfolding is carried out using these matrices, and the largest difference between either result and that obtained from the nominal transfer matrix is taken as the uncertainty.

Shape variations between the MC spectrum and the data will also introduce systematic uncertainty through the unfolding procedure. To estimate this effect, the truth level MC spectrum is reweighted in such a way to improve the agreement between the reconstructed MC and the measured data. The reweighted MC is then unfolded using the original transfer matrix (i.e., the one used to unfold the data). The difference between the result of this and the reweighted truth level MC is taken as a systematic uncertainty, as it reflects the effect of the MC shape on the unfolded spectrum.

The efficiency with which jets are reconstructed has also been considered. This is equivalent to the matching efficiency in the Monte Carlo, and may be estimated in the data by matching reconstructed jets to track jets defined using information from the inner detector. These two efficiencies may be compared in order to estimate the degree to which the jet reconstruction efficiency is mis-modeled by the simulation. The difference is taken

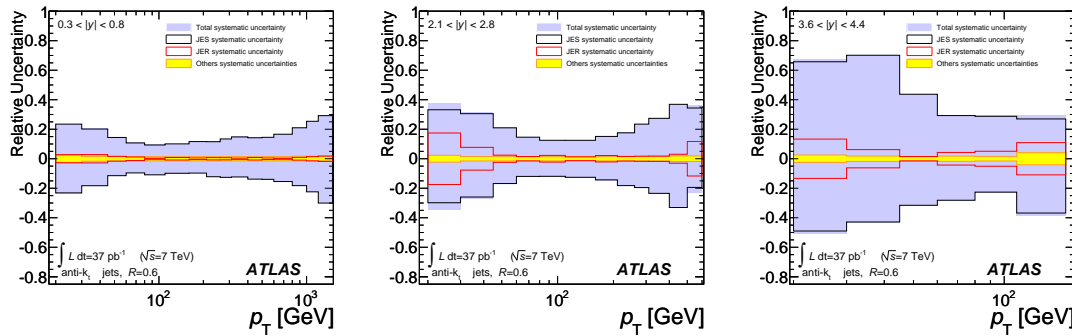


Figure 3.13: Systematic uncertainty on the inclusive jet cross section for anti- k_t jets with $R = 0.6$

as a systematic uncertainty, and is less than 1% for jets with p_T above 30 GeV.

plot of relative systematic for certain rapidity regions is shown in figure ??, showing the contributions from various components.

3.6 Results and discussion

3.6.1 Inclusive Jet Cross Section

results for the inclusive jet cross section are plotted in figure 3.14 for $R = 0.4$ jets and figure 3.15 for $R = 0.6$. Theoretical predictions are obtained using NLOJET++ with the CT10 pdf set, with the normalization and factorization scales set to the p_T of the leading jet, $\mu_r = \mu_f = p_T^{\max}$. The agreement between data and theory is generally good.

In figures 3.16 ($R = 0.4$) and 3.17 ($R = 0.6$), the ratio of the data and theory results is plotted. The CT10 pdf set is used as a baseline, though results obtained using other pdf sets (MSTW2008, NNPDF 2.1, and HERAPDF 1.5) are also shown. All pdf sets tend to predict a higher cross section than that seen in data, with the discrepancy worse at high p_T or high rapidity. MSTW2008 tends to follow the data better in these regions. In all cases, the differences between data and theory are similar in magnitude to the systematic uncertainties from theory and data.

Figures 3.18 and 3.19 show the same ratios, but also include theoretical results ob-

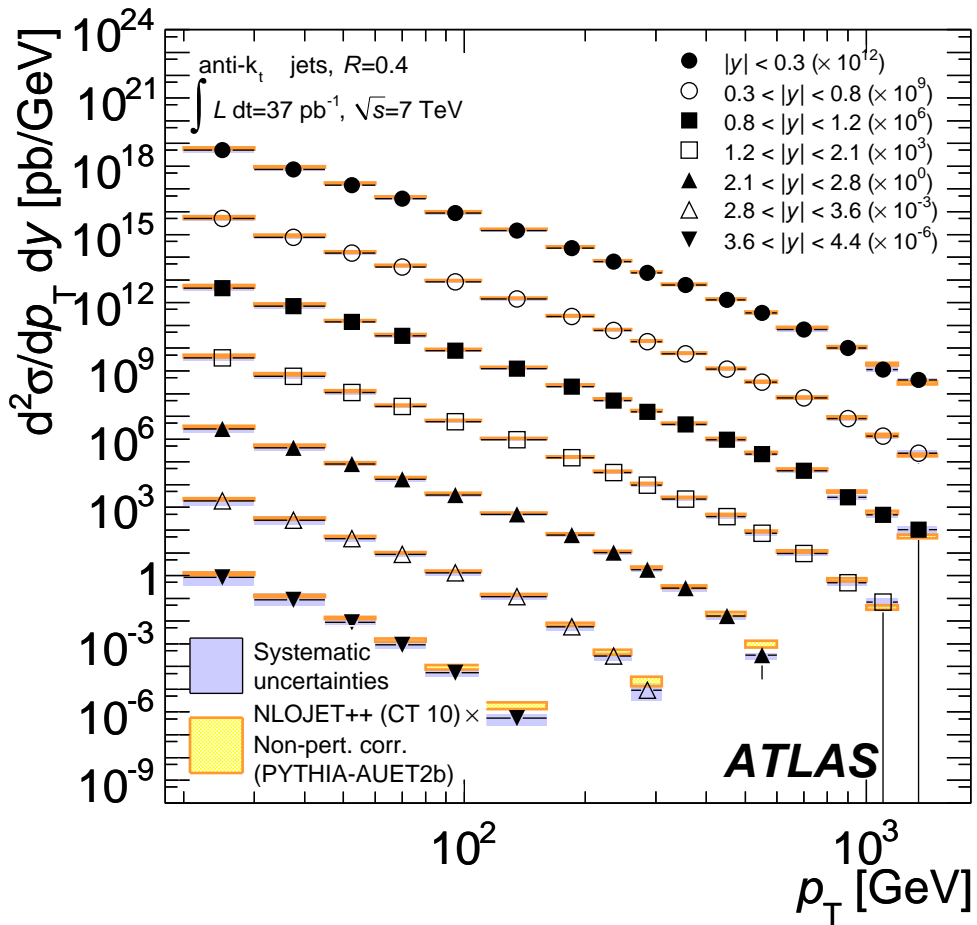


Figure 3.14: Inclusive jet cross section for ant- k_t jets with $R = 0.4$.

tained from POWHEG, with the matrix element calculated using the CT10 PDF set and the parton showering carried out using either PYTHIA (with either the AUET2B or Perugia2011 tune) or HERWIG (AUET tune). The POWHEG results vary significantly depending on the method used for parton showering. These variations are on the order of 30%, whereas the theoretical uncertainty due to non-perturbative effects is less than 10% for jets with $R = 0.4$.

3.6.2 Dijet Mass Spectrum

The dijet mass spectrum, after unfolding, is plotted in figures 3.20 for jets with $R = 0.4$, and 3.21 for $R = 0.6$. The theoretical results are again obtained using NLOJET++ with

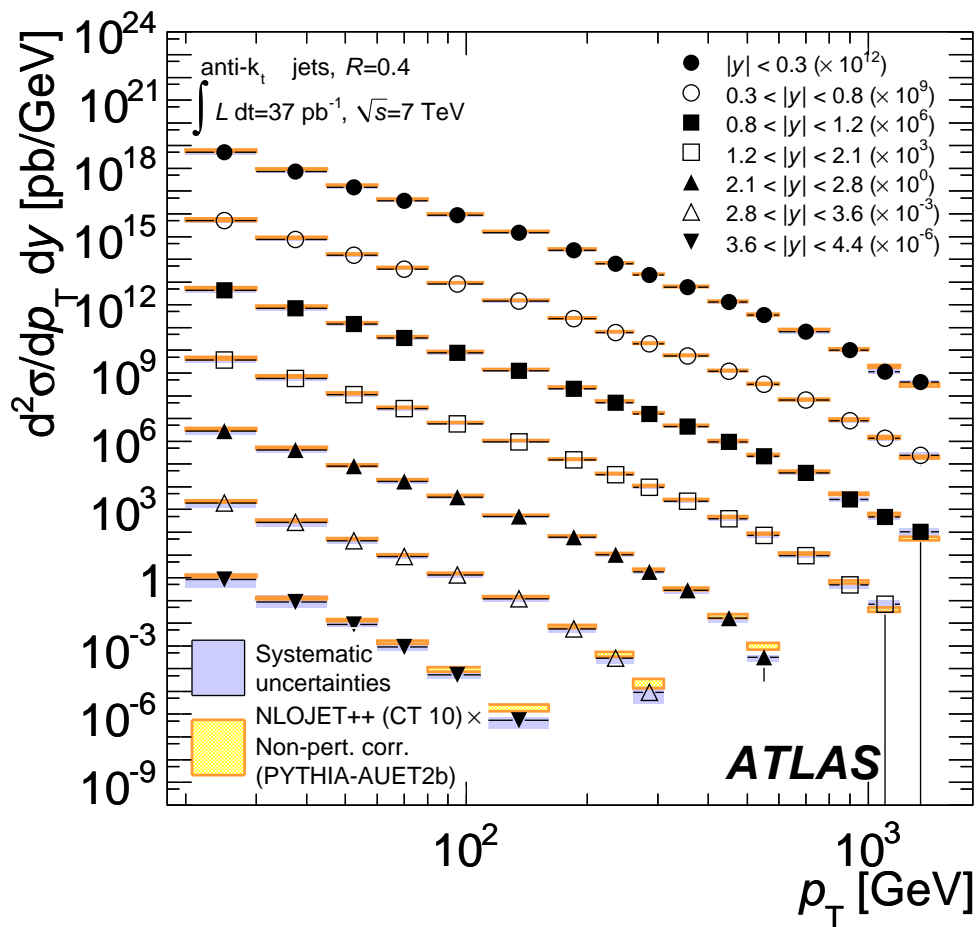


Figure 3.15: Inclusive jet cross section for ant- k_t jets with $R = 0.6$.

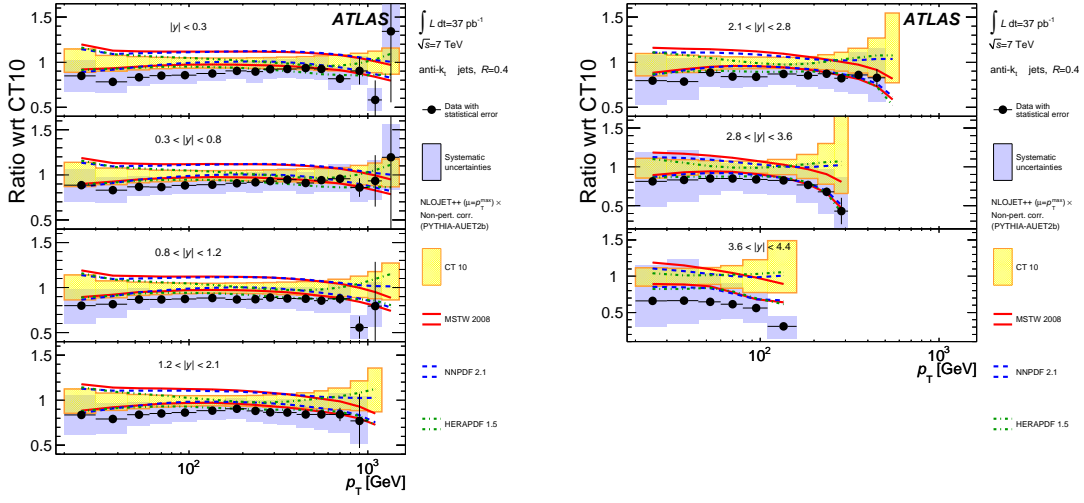


Figure 3.16: Ratio of the inclusive jet cross section to the CTEQ10 prediction, for different rapidity bins using anti- k_t jets with $R = 0.4$. Other pdfs also shown.

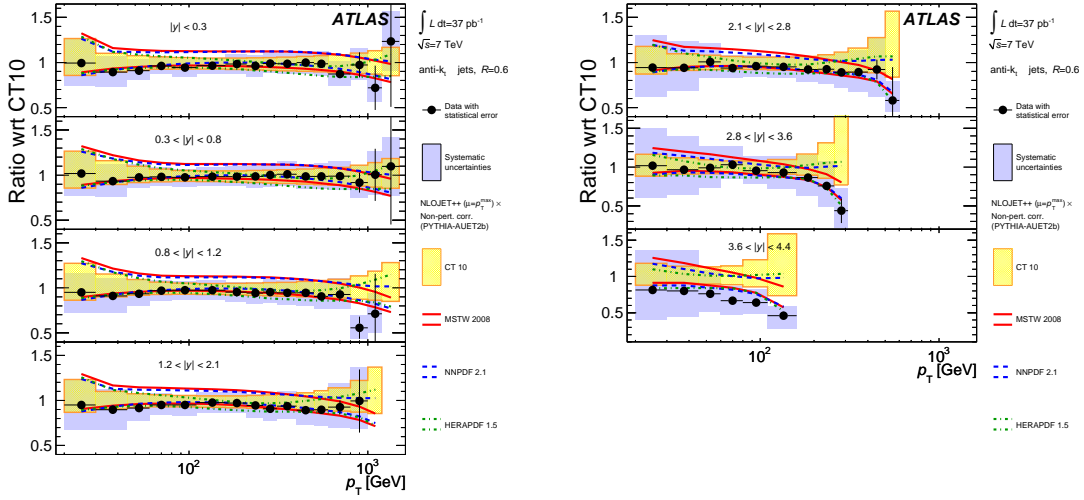


Figure 3.17: Ratio of the inclusive jet cross section to the CTEQ10 prediction, for different rapidity bins using anti- k_t jets with $R = 0.6$. Other pdfs also shown.

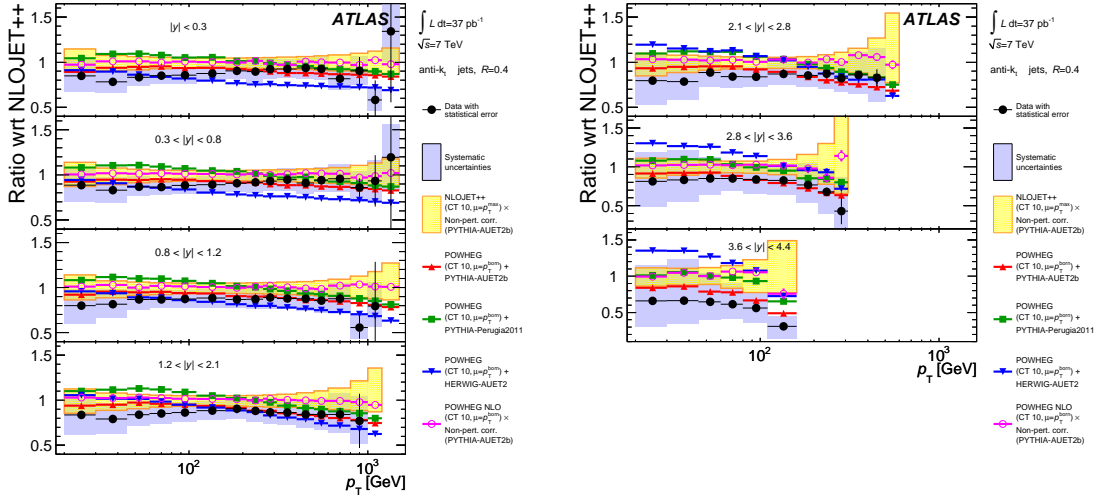


Figure 3.18: Ratio of the inclusive jet cross section to the CTEQ10 prediction, for different rapidity bins using anti- k_t jets with $R = 0.4$. Theoretical predictions made using POWHEG are also shown.

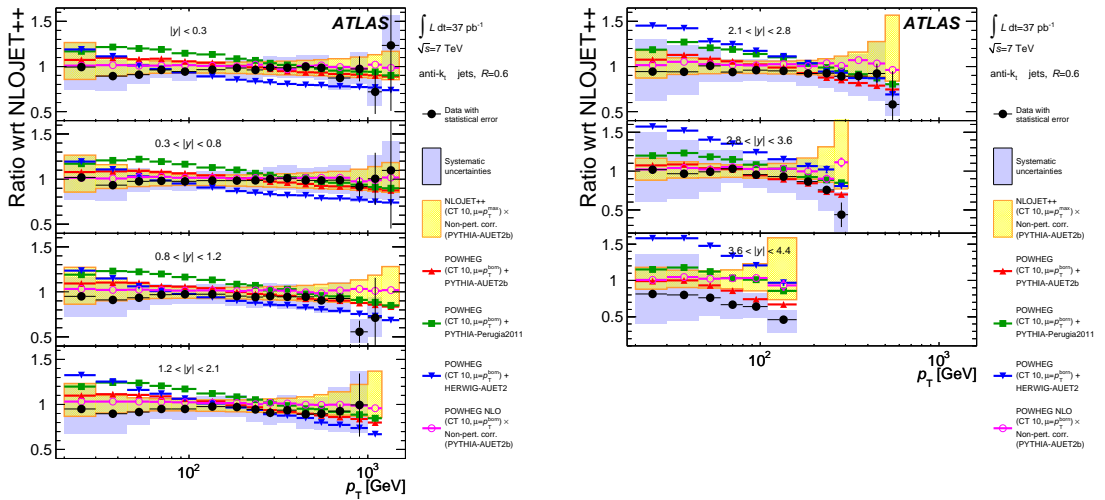


Figure 3.19: Ratio of the inclusive jet cross section to the CTEQ10 prediction, for different rapidity bins using anti- k_t jets with $R = 0.6$. Theoretical predictions made using POWHEG are also shown.

the CT10 pdf set and PYTHIA for the parton showering. In this case, the scales

$$\mu_r = \mu_f = \frac{m_{12}}{2 \cosh(0.7y^*)} \quad (3.22)$$

were chosen for normalization and factorization, as this choice was found to be more stable at high values of y^* .

Theoretical results from different pdf sets are plotted in figures 3.22 and 3.23, shown as a ratio to the result obtained using CT10. Data and theory can be seen to agree well at small separations. At larger values of y^* , fluctuations appear in the data/theory ratio. The data spectrum is smooth in this region, and fluctuations are due to lack of statistics in the theoretical predictions.

Results obtained from POWHEG are plotted in figures 3.24 and 3.25. POWHEG did not exhibit the instabilities seen at high separations in NLOJET++, and so the scales $\mu_r = \mu_f = p_T^{\max}$ are again used with POWHEG. The best agreement between theory and data is seen when using the AUET2b tune, with Perugia2011 and AUET yielding cross sections higher than that seen in data.

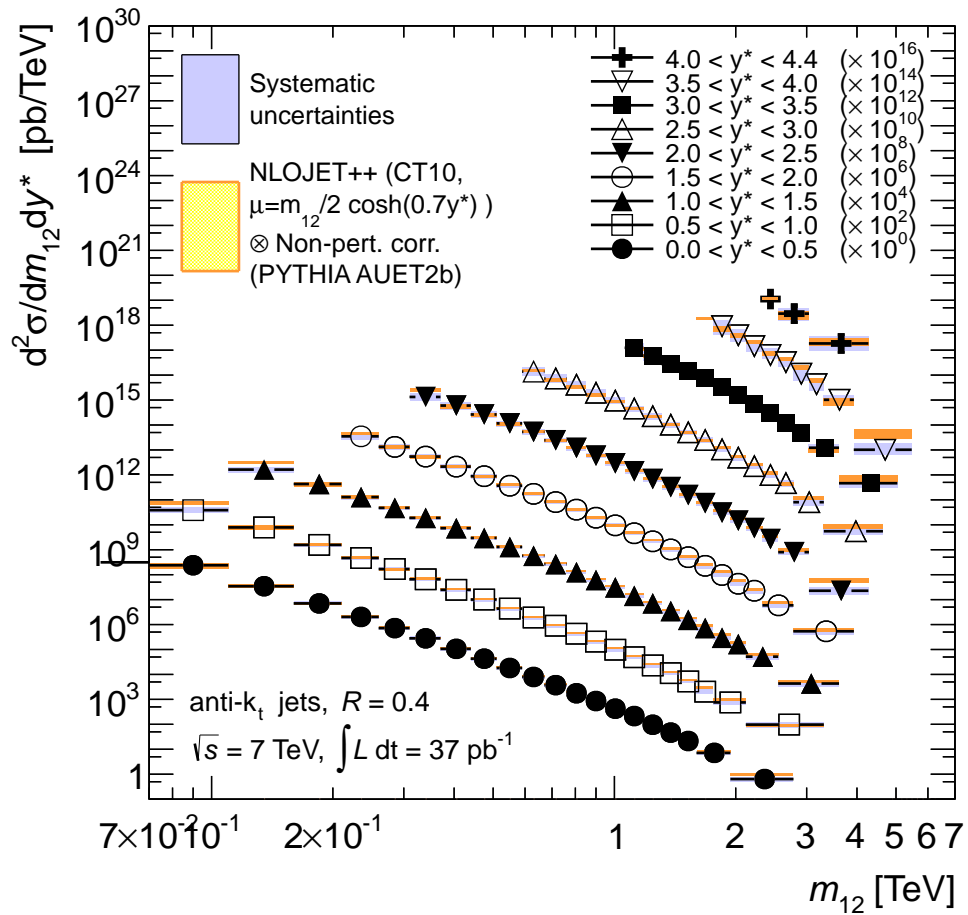


Figure 3.20: Dijet mass spectrum for anti- k_t jets with $R = 0.4$.

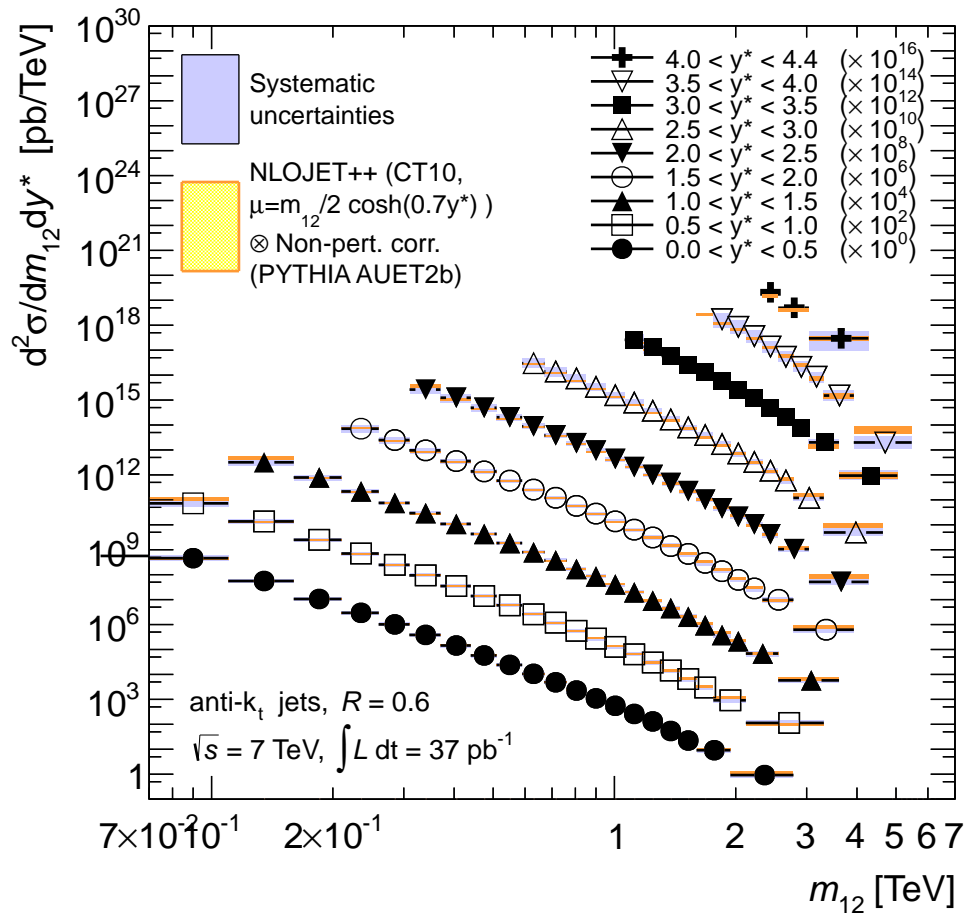


Figure 3.21: Dijet mass spectrum for anti- k_t jets with $R = 0.6$.

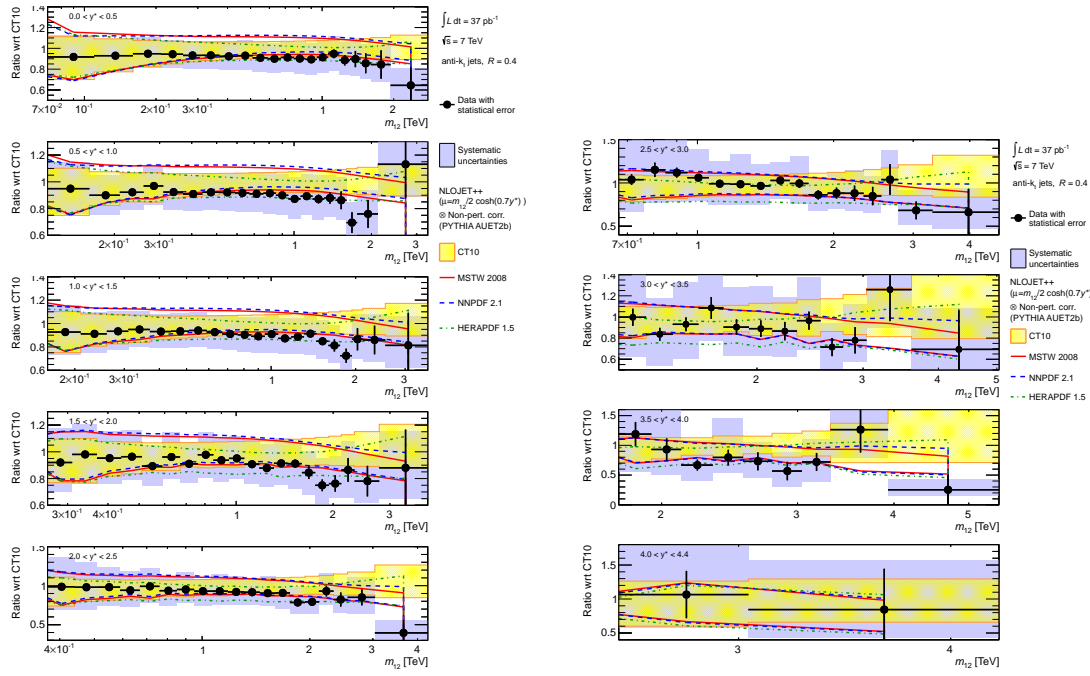


Figure 3.22: Ratio of measured dijet mass spectrum to theoretical prediction obtained using POWHEG, for anti- k_t jets with $R = 0.4$.

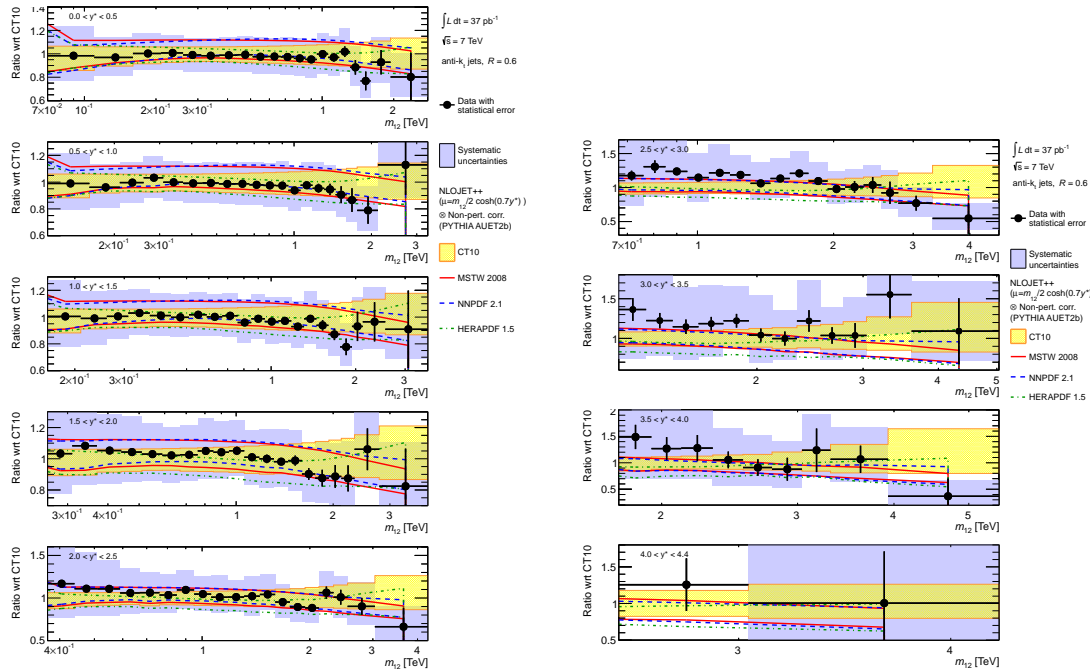


Figure 3.23: Ratio of measured dijet mass spectrum to theoretical prediction obtained using POWHEG, for anti- k_t jets with $R = 0.6$.

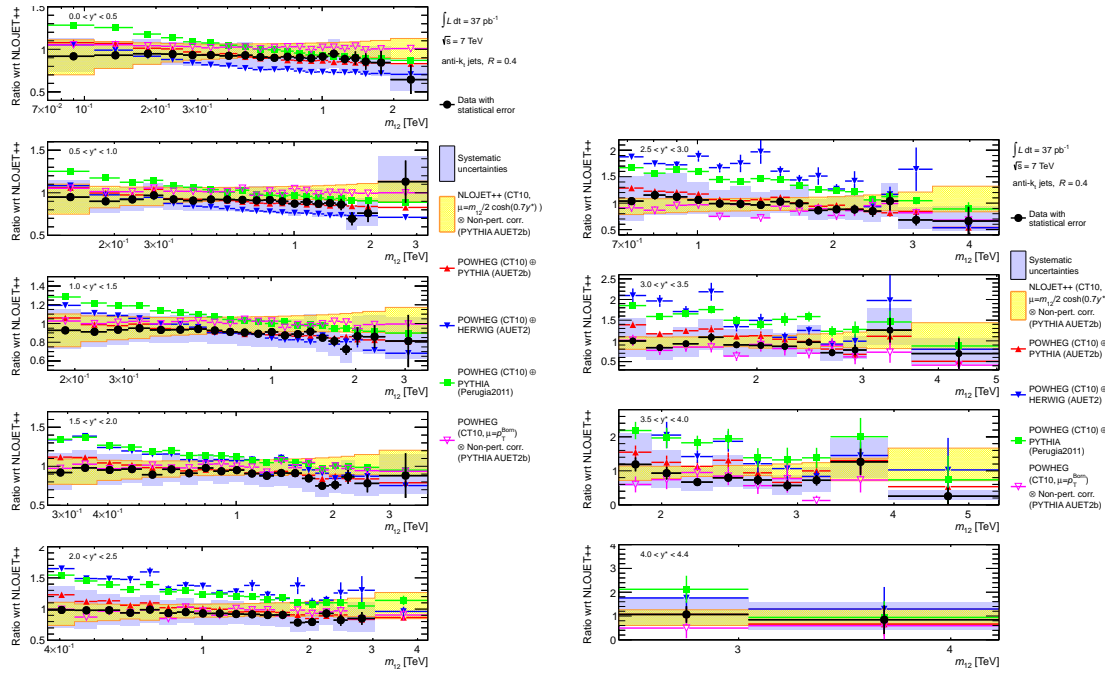


Figure 3.24: Ratio of measured dijet mass spectrum to theoretical prediction obtained using POWHEG, for anti- k_t jets with $R = 0.4$.

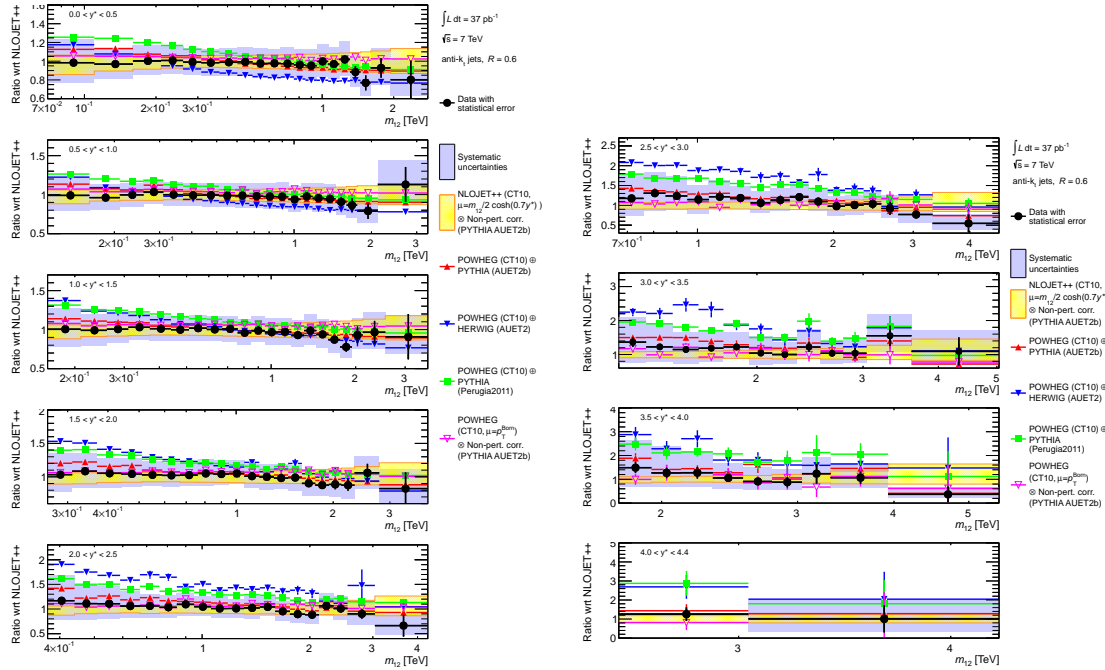


Figure 3.25: Ratio of measured dijet mass spectrum to theoretical prediction obtained using POWHEG, for anti- k_t jets with $R = 0.6$.

Chapter 4

TestBeam Overview

4.1 Introduction

test test this should reference the CT10 fig [12].

The first testbeam studies of the ATLAS Forward Calorimeter were carried out in 1993, using an early prototype of FCal1. This study provided proof of principle of the calorimeter design, and based on the results the design was adopted by the ATLAS collaboration [8]. The prototype used in these studies had a depth of 25cm, which is approximately half the depth of the FCal1 module presently being used in ATLAS. A subsequent beam test was carried out in 1995 using a full-depth FCal1 prototype [3]. In 1998 further beam tests were carried out at CERN using full-depth “module 0” prototypes of FCal1 and FCal2, which allowed the response of the hadronic modules to be investigated for the first time [14, 4]. The 2003 testbeam utilised all three of the C-side FCal modules presently operating in ATLAS, and will be discussed in detail in the following chapters. Following this, a 2004 coombined testbeam studied the behaviour of the end cap calorimeters[16]. This included the “module 0” FCal1 and FCal2 prototypes used in the 1998 testbeam, as well as modules from the EMEC and HEC calorimeters.

The 2003 testbeam studies were carried out in the H6 beamline at CERN, which is

fed by the Super Proton Synchrotron (SPS). Protons from the SPS were directed at fixed targets in order to produce secondary beams of the desired particles (electrons/positrons or charged pions) at the required energy.

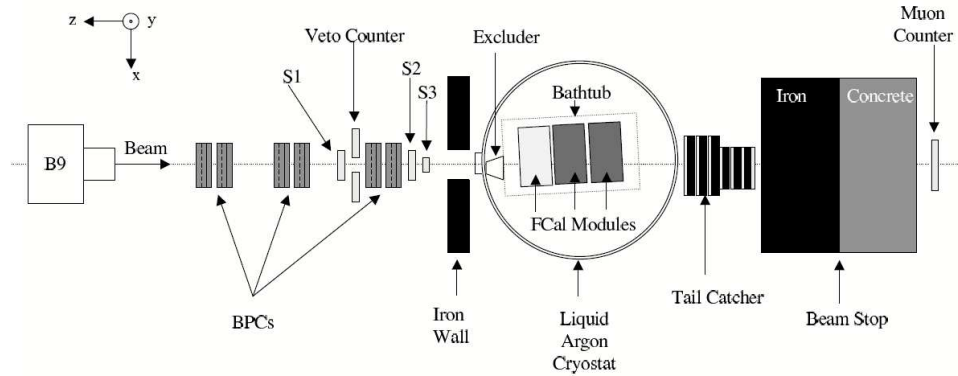


Figure 4.1: Diagram showing the setup used for the 2003 FCal beam test (not to scale).

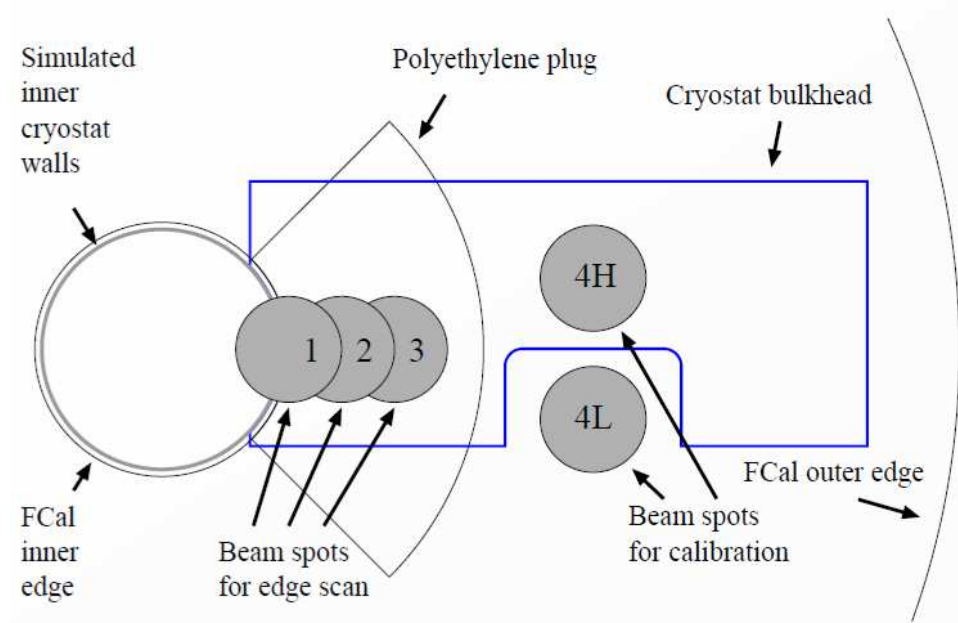


Figure 4.2: Beamspots studied in the testbeam.

A diagram of the beamline is shown in figure 4.1. Beam particles emerge from the B9 magnet, traveling a distance of 32 metres and passing through several sets of instruments before reaching the FCal. The B9 magnet was used to control the vertical inclination

of the beam, and thus the vertical position of the beamspot on the FCal face could be controlled via manipulation of the currents in the B9 magnet. The cryostat containing the FCal was able to be translated horizontally and rotated, which provided control over the horizontal position of the beamspot and the angle at which the beam particles struck the front face of the calorimeter. A total of 5 beamspots were used, numbered 1,2,3, 4L and 4H. The locations of these beamspots are depicted in figure 4.2. Positions 1,2 and 3 were used to study the effects of energy leakage across the beampipe from particles impacting close to the inner diameter. High energy (~ 200 GeV) beams of electrons and pions were used to provide data at these positions, and the results of these studies can be found in [11]. Position 4L was used to study the intrinsic response of the FCal with a minimal amount of material between the calorimeter and the incoming particles, whereas position 4H was used to simulate a more ATLAS-like environment with additional dead material introduced into the beamline. Electrons and pions at energies from 10-200GeV were used at these beamspots. This thesis will focus on the analysis of data taken at positions 4L and 4H, and the comparison of this data to results obtained from Monte Carlo simulations.

4.2 Beamlne Instrumentation

Eight beam profile chambers (BPCs) were used to provide tracking information on beam particles. Four of these BPCs were of a more sophisticated design, one pair of which was located about 1.6 metres downstream from the B9 magnet while the other pair was situated 3m upstream from the FCal, on an adjustable table described below. These chambers contain two readout planes, oriented at right angles such that measurements of both transverse coordinates may be made. Each readout plane covers an area of $120mm \times 120mm$, and has an average resolution of around $130\mu m$. The other four BPCs were of an older design and were able to measure a single track coordinate with a

resolution of about $325\mu m$. These were positioned in the middle of the beamline (about 20m from the FCal), with two BPCs measuring the X coordinate of the beam particles and the other two the Y coordinate. In total, the eight BPCs provide six independent measurements of the X and Y coordinates of the beam particle tracks.

A mapping between BPC and calorimeter coordinates was established through analysis of electron data. The track measured by the BPCs was projected on to the calorimeter in order to obtain the beam impact point in the BPC coordinate system. This was then associated with the barycentre of the energy deposited in FCal1 using the calorimeter coordinate system. However, the finite granularity of the calorimeter readout tended to bias the position of the energy barycentres towards the centre of the readout cells. This was corrected for by considering the ratio E_{\max}/E_1 , where E_1 was the total energy deposited in FCal1 and E_{\max} was the largest energy value contained in a single channel. This ratio was plotted as a function of (BPC) x and y , with minimal values in the ratio corresponding to cases where energy was shared evenly between multiple channels. The positions of the minima could thus be associated with cell boundaries in the calorimeter coordinate system, which then allowed the mapping between BPC and calorimeter coordinate systems to be determined with greater precision.

The adjustable table was positioned about 2 metres upstream from the cryostat, on which three scintillators (S1, S2, S3) were positioned. These scintillators were polystyrene-based, and were used for triggering and “beam cleaning”, which is discussed in section 5.1. All three scintillators were 1 cm thick, with S1 and S2 having cross-sectional dimensions of $10\text{cm} \times 10\text{cm}$, while S3 had dimensions $7\text{cm} \times 7\text{cm}$. A veto counter was also present on the table, consisting of rectangular piece of scintillator ($63\text{cm} \times 63\text{cm} \times 5\text{cm}$) with a circular hole 65mm in diameter that the beam passed through. The height of this table could be varied such that the beam instruments were in the appropriate position for the beamspot under study.

As the liquid argon gaps in the FCal are much smaller than those used in typical

liquid argon calorimeters, FCal channels are susceptible to shorts should any conductive debris find its way into the liquid argon. Because the cryostat was not a particularly clean environment, the FCal was housed inside a “bathtub” which sat inside the cryostat. The bathtub was made from stainless steel 1.5 mm thick, and had a rectangular shape. Holes were present on its sides to allow the liquid argon to flow in as the cryostat was filled, but these were covered with a fine mesh to keep any debris out.

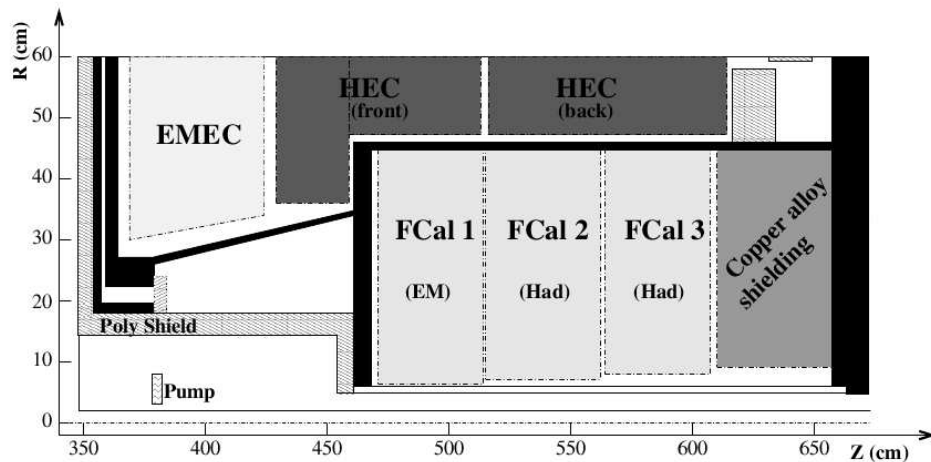


Figure 4.3: Cross section of FCal positioned within the end-cap cryostat, showing the inactive material laying between the calorimeter and the interaction point.

In order to simulate a more ATLAS-like environment for data taken at positions 1,2,3 and 4H, additional material was inserted into the beamline. A cross section of part of the ATLAS end cap is shown in figure 4.3, showing the uninstrumented (or “dead”) material present in the end-cap. An aluminium plate 5.1 mm thick was bolted to the inside of the bathtub to model the cryostat bulkhead, with a slot cut out of the plate such that the additional aluminium would not affect beams directed at position 4L. The area covered by this plate is shown in figure 4.2.

The JM shielding (labelled “poly shield” in figure 4.3) is made of boronated polyethylene and is present in ATLAS to prevent albedo radiation from scattering back into the inner detector. This was modelled in the beam test by placing a wedge shaped piece of polyethylene on the outside of the bathtub such that it covered positions 1,2, and 3,

simulating the toroidal “plug” part of the shielding that lies close to the beam pipe and adjacent to the cryostat bulkhead. An iron wall was located between the adjustable table and the cryostat. This wall had a 10cm x 10cm slot cut into it to allow the beam to pass through. When taking data at position 4H, a rectangularly shaped piece of polyethylene with dimensions 5cm x 20cm x 1m was placed at an angle in this slot. This was done in order to model the tube shaped part of the JM shielding that ran parallel to the beam axis. When running at position 1, a small piece of aluminium was instead placed in this slot, simulating the ion pump present close to the beampipe in ATLAS.

An “excluder” made of RohaCell was also attached to the outside of the bathtub. In ATLAS the area between the FCal support tube and the beampipe is evacuated, and so the excluder was placed inside the cryostat to prevent this space from being occupied by liquid argon. The density of RohaCell is 0.011 g/cm³ whereas that of liquid argon is 1.43 g/cm³, so the RohaCell provides a relatively good approximation of a vacuum. A hollow stainless steel cylinder was also placed inside the FCal during the beam test to simulate the beampipe.

A tail-catcher calorimeter was positioned downstream of the cryostat, and was comprised of layers of steel and scintillator. Behind the tail-catcher was a beamstop of iron and concrete, and beyond that a muon counter was located. The tail-catcher and muon counter were only used for muon identification: no information from the tail-catcher was used in the analysis of the FCal response.

A CEDAR (Cherenkov Differential counter with Achromatic Ring focus, [7]) detector was located upstream of the B9 magnet and used for particle identification. The CEDAR detector consisted of a chamber filled with gas (He or N₂) at high pressure. As beam particles passed through this chamber, they would emit Cherenkov radiation at an angle that depended on their velocity and mass. The optics of the CEDAR would then collect this light and focus it into a ring-shaped image, with different types of particles giving rings of different radii. An adjustable annular aperture was positioned in front of a

series of photomultipliers, such that they would only detect light from rings of a given radius. The radius selected by the aperture could be tuned such that signal from the photomultipliers corresponded to a beam particle of the desired mass.

4.2.1 Timing and Pulse Shapes

done using ofc method described in section 1.2.3. A SPICE [15] simulation of the electronics chain is used to obtain an initial estimate of the pulse shape used in the OFC calculation. This estimate was then improved using an iterative procedure that incorporated data taken from physics runs. The data used in this procedure is taken from events in which have a large pulse amplitude, in order to ensure that the signal is coming from a physical energy deposit.

Pulse shapes are sampled in time with the TTC clock on the FEBs. Seven samples were recorded for each pulse during physics runs, with the timing adjusted such that on average the fourth sample was coincident with the pulse peak. In ATLAS the timing is synchronised to the LHC clock, such that samples are taken in time with each bunch crossing. This was not the case during the beam test, as beam particles arrived at random phases with respect to the TTC clock. In this case, timing for the event was taken from the S1 scintillator. A LeCroy 2228A Time to Digital Converter (TDC) with a timing resolution of 50 ps was used to measure the phase difference between the event trigger and the TTC clock, with the trigger from the S1 scintillator used as a start signal and the clock pulse from the TTC used as a stop signal. The TDC only measured a phase difference between the start and stop signals, and so readings close to 0 or 25 ns were ambiguous. To resolve this a second TDC was used in which the stop signal was delayed by 10 ns, which allowed the time interval between the beam trigger and the TTC pulse to be determined uniquely.

While the OFC method is capable of handling time differences between pulse peaks and sample times, the Taylor expansion used in equation 1.3 becomes invalid when this

time, τ , becomes large. To avoid this issue, events are binned according to the TDC phase time, using 25 bins of width 1 ns. A set of OFCS is calculated for each bin using a pulse shape that has been shifted in time by the relevant amount. During event reconstruction, the amplitude of each pulse is obtained by using the set of OFCs corresponding to the TDC phase time for that event. Only a single set of OFCs is required at **ATLAS**, as in this case the TTC clocks are synchronised with that of the LHC, and so the samples are taken in time with the bunch crossings.

4.2.2 Offline Reconstruction

Offline reconstruction of testbeam data is carried out in **Athena**. For each event, the LArRawChannelBuilder algorithm retrieves the pulse samples (which are stored as LArDigits), and fetches the OFCs from a database. The pedestal is then subtracted from these samples and the OFCs are applied, giving the amplitude of the pulse in ADC counts. This amplitude is then converted to an energy using a factor (the “ADC2MeV” value) that depends on the channel and gain. The energy of the channel, in MeV, is then stored as a LArRawChannel object. Another algorithm is then used to create CaloCell object from this LArRawChannel. From the CaloCell the position, time, energy, quality, and four-momentum of the channel may be retrieved, making CaloCells suitable objects to be used in data analysis. Because of this, CaloCell information is recorded by default in Event Summary Data (ESD) files, which are one of the standard formats used by **ATLAS**. CaloCells are also used as input for topoclustering algorithms, which in turn are used as input for jet-finding and missing energy algorithms.

For initial studies of the testbeam data, the ADC2MeV factors used in the reconstruction were set to 1, such that the final energies obtained were in terms of ADC counts. This was done to simplify measurements of the FCal energy. However, the LArRawChannel class used in **Athena** stores channel energys as an integer number of MeV, as energies less than 1 MeV are deemed insignificant. An unforeseen consequence of this was that

in earlier versions of the testbeam analysis, cell energies were truncated (rounded down) to an integer number of ADC counts. This rounding meant that energy was effectively lost during the reconstruction process, up to ~ 80 MeV per cell in FCal1 and ~ 160 (~ 185) MeV in FCal2 (FCal3). This had some effect on the electron results but a more significant effect on the hadron results, due to broader showers and higher ADC2MEV factors used in the hadronic modules. The bug has since been fixed, and none of the results presented here are affected by it.

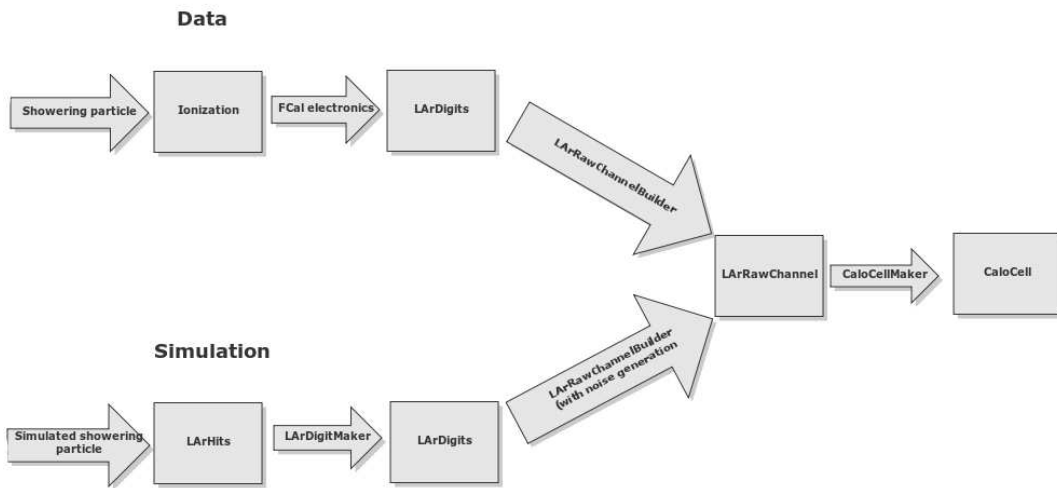


Figure 4.4: Flowchart showing the processes/algorithms and data structures involved in the reconstruction of testbeam data and simulation results.

4.3 Simulation

A Monte Carlo simulation of the testbeam setup has been developed within the Athena framework. Geant 4.9.2 [?] is used to simulate interactions of the beam particles with beamline elements. The results of this simulation are then reconstructed and analyzed in the same manner as the data.

4.3.1 Geant4

Geometry in **Geant4** is described in terms of volumes. A “solid volume” is first created to describe the shape of a given object. This is then used to derive a logical volume, which inherits the shape of the solid and is associated with a material. A material type is defined by specifying the relative mass fractions of its constituent elements and the density of the material. Logical volumes are then used to construct physical volumes , which inherit the shape and material information from the logical volume. A physical volume also has a position and orientation assigned to it, and it is by positioning these physical volumes that the geometry of the simulation is defined. A special physical volume, the world volume, is created first. All subsequent physical volumes are then placed either inside the world, or inside another physical volume.

The description of the beamline used in the simulation contains all the beamline elements from the B9 magnet to the tailcatcher, including all scintillators, BPCs, cryostat material and beampipes. Most of these objects are defined from scratch, however the description of the FCal is taken from that used in the full **ATLAS** simulation while the cryostat description has been taken from another testbeam simulation. Elements upstream of the B9 magnet, such as the CEDAR detector, have not been included.

The description of the FCal has been modified in some respects, to improve some aspects of the material description. In the default FCal definition the rods in the hadronic modules are made of WFeNi whereas they are actually pure tungsten, which has a slightly higher density. The density of the absorber matrix was also corrected, as an updated estimate of this value was obtained . The correct materials and densities (given in section 1.2.3) have been used in the testbeam simulation.

The abstract way in which positions are defined can also lead to errors. **Geant4** uses matrices to represent transformations, and so the order of operations are important. When a physical volume is inserted into the world (or another physical volume), it is placed at the origin of that volume’s coordinate system, and must be repositioned by

applying transformations. These transformations are not commutative, so care must be taken to ensure the operations are applied in the correct order. The last operation specified prior to the creation of a physical volume is the first operation applied to it once it is placed in the world, which can be counterintuitive if these transformations are not thought of as matrix operations.

In **Geant4**, physics is defined in terms of processes. Particles are propagated through the simulation in a step by step fashion, with continuous processes (such as ionisation) acting on the particle during the step while discrete processes (such as decays, pair production) take place at the end of a step. After each step, the particle’s kinematics are updated. Secondary particles are only produced if their energy exceeds a “range cut”. If a process would produce a secondary particle with energy less than the range cut, this energy is instead deposited in the material. Range cuts are specified as a distance, but **Geant4** converts this distance to an energy based on the material the particle is travelling through at the time. A range cut of $30\mu m$ has been used for testbeam simulations, which is appropriate given the narrow width of the active liquid argon gaps. In the full **ATLAS** simulation, range cuts of $100\mu m$ are used in the EM barrel and EMEC calorimeters, while a cut value of 1mm is used in the HEC.

Electromagnetic showers are generally well understood and relatively straightforward to model. Hadronic showers are more complex, and a variety of processes are used to describe the shower development. Hadronic “physics lists” are used to define the specific set of processes available and the energy ranges in which they are used. Three physics lists have been used in the simulation of the test beam, and are outlined below:

- QGSP_BERT: Quark Gluon String Precompound with Bertini cascade. This is the default physics list used for **ATLAS** simulations. The Quark Gluon String model [10] is used to simulate hard inelastic scattering for hadrons in with energies from 12 GeV to 100 TeV. One or more strings are formed between partons of the colliding hadrons, and these strings are then “cut” by inserting quark/anti-quark

pairs. One member of the pair becomes the new “end” of the string, while the other forms a hadron with the parton that was the old end. This process repeats until the string has insufficient energy to form new pairs. The precompound model is then used to de-excite what remains of the nucleus. Between 9.5 and 25 GeV, a Low Energy Parameterization (LEP) is used to describe inelastic scattering [9]. For particles with energy less than 10 GeV, a Bertini intra-nuclear cascade model [5, 6] is used to describe inelastic scattering with nuclei. The incoming hadron is classically scattered within the nucleus, using cross sections and angular distributions taken from experiment.

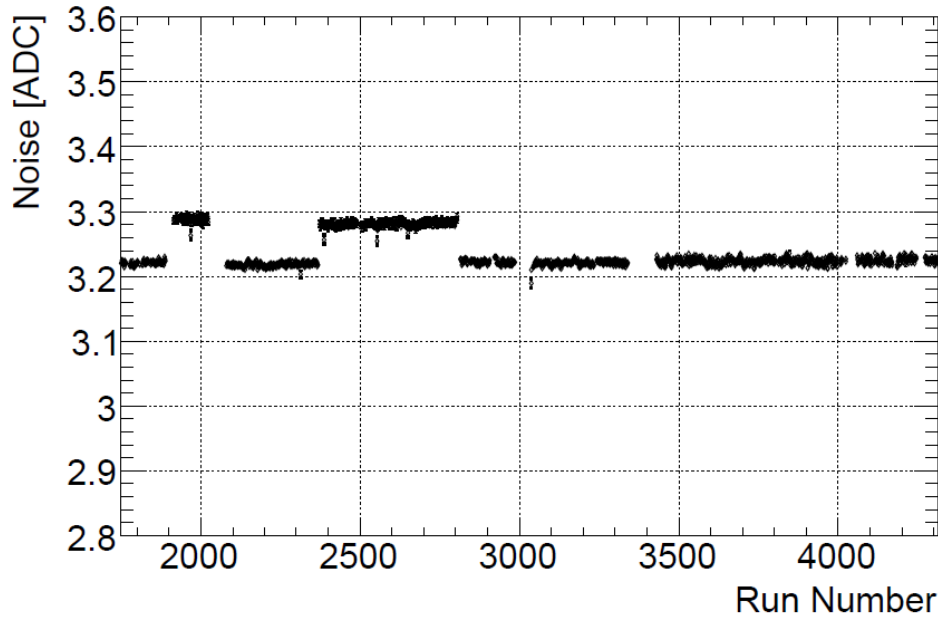
- **QGSP_BERT_HP:** This physics list is essentially the same as QGSP_BERT, but includes high precision modeling for low energy neutrons ($<20\text{MeV}$). This method relies extensively on cross sections obtained from experiment. It was reported in [17] that the high precision neutron tracking had a significant effect on the development of hadronic showers in tungsten, and so it was considered worthwhile to investigate this physics list.
- **FTFP_BERT:** This physics list uses the Fritiof string model [1] to model high energy inelastic interactions, which is similar to the Quark-Gluon String model described above. The Fritiof model can be applied over a wide range of energies, and is used for hadrons with energies between 4 GeV and 100TeV. As with QGSP_BERT, the precompound model is used to de-excite the nucleus following the Fritiof interaction. The Bertini Cascade model is also used at energies below 5 GeV.

4.3.2 Reconstruction of Simulation Results

The reconstruction chain used for Monte Carlo simulations is, with a few exceptions, the same as that used for reconstruction of the test beam data. In **Geant4**, when a showering particle deposits energy through ionization in a liquid argon gap, a “hit” is produced.

The hit describes the size, time and location of the energy deposited in the liquid argon. A digitization step then collects these hits and simulates the electronics chain to in order to produce digitized samples of the pulse shape, which are again stored as LArDigits. These are then processed into LArRawChannels and CaloCells in the same manner as is used for data, as shown in figure 4.4.

Electronic noise must also be modeled in the simulation. For the FCal, most of this noise arises in the preamplifiers on the summing boards. Noise can be quantified by studying the rms of the pedestal values, which gives a value of 3.2 ADC counts per sample when averaged over all channels and all runs. In addition to physics data, some randomly triggered events were recorded during data taking. The data taken by these random triggers is essentially all noise, and allows the correlations in the noise to be studied.



step, where the autocorrelation matrix for the noise is retrieved from a database. It is then used to randomly generate the noise contributions that are added to each sample. However, during data taking the level of electronic noise present was seen to vary, as can be seen in figure 4.5. Data for different beam configurations was taken at various times, so the average noise present for runs at a specific particle/beamspace/energy differs to that for runs with another beam configuration.

To account for this, randomly triggered data taken from the same runs as the physics data is used to generate noise added into the simulation, using a procedure discussed below. This method allows different beam configurations to be reconstructed with different levels of noise, whereas the default method of generating noise lacks this functionality.

4.3.3 Noise Generation and Application

The noise added into the simulation is derived from the randomly triggered data. A covariance matrix is generated by running over the randomly triggered data taken with a specific beam configuration (e.g. 200GeV pions directed at position 4L), such that

$$M_{ij} = \frac{1}{N_{\text{events}}} \sum_n^{N_{\text{events}}} e_{i,n} e_{j,n} \quad (4.1)$$

where $e_{i,n}$ is the noise reconstructed from the i -th channel of the n -th event, in ADC counts. The matrix M_{ij} is then diagonalised, such that it can be written as

$$\mathbf{M} = \mathbf{U}^T \mathbf{D} \mathbf{U} \quad (4.2)$$

where \mathbf{U} is a unitary matrix with columns equal to the eigenvectors of \mathbf{M} , and \mathbf{D} is a diagonal matrix which has the eigenvalues of \mathbf{M} as its entries. The matrix \mathbf{U}^T thus acts as a transformation matrix, transforming information from the “channel” basis to the eigenvector basis. The eigenvectors and eigenvalues are written to file, and then retrieved

during the reconstruction.

The noise is applied in the LArRawChannelBuilder algorithm, after the pulse peak has been found through application of the OFCs. The matrix U_{ij} and eigenvalues D_{ii} are first read from file. For each event a vector of noise, N_i is then generated. This is done in the eigenvector basis using a normal distribution, such that $\text{sigma}(N_i) = D_{ii}$. This noise is then transformed back into channel basis, such that

$$N'_i = \sum_j U_{ij} N_j \quad (4.3)$$

which builds in all the correlations between channels. The noise N'_i is then added to the reconstructed pulse peak of the i -th channel.

The default method relies on an autocorrelation matrix, such that correlations between samples are present but each channel is considered independently. This method avoids dealing with the noise on individual samples and instead considers the total noise on the reconstructed pulse peak, while also incorporating correlations in the noise between different channels. These correlations are significant, as without them the estimations of the noise contribution in a given cluster are too low. This is important when studying the energy resolution of the FCal, which will be discussed later.

Chapter 5

Testbeam Results

5.1 Event Selection

The three scintillators located on the adjustable table (S1, S2, S3) are used for triggering. Coincident signals are required from all three in order for the event to be accepted. Signal from the veto counter indicates that the beam particle has scattered off the upstream material, and in these cases the event is rejected. For data taken from an electron beam, events were also rejected if there was any signal in either the tail-catcher or the muon counter, indicating the presence of muons. Muons can sometimes be produced during hadronic showers, and so these cuts were not applied for data taken from pion beams.

A series of “Beam Cleaning” cuts were applied, which also used information from the scintillators. The beam cleaning cuts were implemented in order to remove events which contained multiple beam particles and events in which the beam particle had scattered off the upstream material. In order to remove events in which multiple particles were present, the signal from each scintillator was compared to that expected for a minimum ionizing particle (MIP). If a single scintillator produced a signal consistent with 5 times that of a MIP, or at least two scintillators gave signals over twice the MIP threshold, the event was rejected.

Particle tracks are reconstructed by performing a linear fit on the data from the BPCs. The $x - z$ and $y - z$ planes are fitted separately, with the BPCs providing six measurements of the track in each plane. If the χ^2 value for either fit exceeds 40.0, the event is rejected. These tracks were then used to make “beam envelope” cuts, which were intended to remove events containing undesired particles. The secondary beams delivered to the testing area were not completely pure, and so hadrons were sometimes present in the electron beams and protons sometimes present in the pion beams. The magnet systems in the H6 beamline tended to place electrons and hadrons into different areas of phase space, due to differences in their charge to mass ratios. The x intercept of the track, c_x , is measured using the BPC closest to the FCal. This is used to determine an “ideal” slope in the $x - z$ plane for the desired particle type, $m_{x,i}(c_x)$, as well as a width parameter, $\sigma_x(c_x)$. The procedure is then repeated to obtain the intercept, ideal slope, and width parameter in the $y - z$ plane, denoted as c_y , $m_{y,i}(c_y)$, and $\sigma_y(c_y)$ respectively. The quantity

$$\Delta S = \left(\left(\frac{m_{x,i}(c_x) - m_{x,m}}{\sigma_x(c_x)} \right)^2 + \left(\frac{m_{y,i}(c_y) - m_{y,m}}{\sigma_y(c_y)} \right)^2 \right)^{1/2} \quad (5.1)$$

is then calculated, where $m_{x,m}$ and $m_{y,m}$ are the measured track slopes in the x and y directions, respectively. If ΔS exceeds a specified threshold (1.25 in this analysis), the measured track is deemed to lie outside the beam envelope for the desired particle type, and the event is rejected.

While the primary purpose of the BPCs was to obtain tracking information on the beam particles, they were used in the beam cleaning in a similar way to the scintillators. A key feature of MWPCs is that the total charge arriving at an anode is proportional to the total number of electron-ion pairs produced in the chamber, and from this the number of ionizing particles that passed through the active areas could be inferred. Events were rejected if a single BPC produced a signal five times greater than that expected for a

single MIP, or if at least two BPCs generated a signal twice that expected for a single MIP.

As mentioned earlier, two TDCs were used to measure the time interval from the trigger signal until the clock pulse on the TTC, at which time the signals from the calorimeter were sampled. output from the TDC is given as an integer number of TDC counts, between ~ 300 and ~ 800 , which covers a time interval of 25 ns and thus gives the TDC a time resolution of 50 ps. There are three regions where a mismeasurement of the TDC can be problematic: near the TDC's minimum value, its maximum value, and the "wrap around" region. The wrap around point is where the phase jump occurs, such that the time interval measured by the TDC jumps suddenly from 0 ns to 25 ns. The TDC phase quality is defined as the smallest difference between the TDC reading and one of the problematic values. Event timing was determined using the TDC which had the highest phase quality. The event was rejected if the TDC phase quality did not lie in the range $20 < \text{TDcPhaseQuality} < 230$, as in these cases the better clock choice was still within 1 ns of a problematic region.

The CEDAR detector was also used to improve the beam purity. This was mainly used to eliminate proton events when taking data with π^+ beams, by rejecting events containing beam particles that the CEDAR did not identify as charged pions. However, the CEDAR was also used when recording electron data at 60 GeV, as it proved exceptionally difficult to obtain a relatively pure electron beam at this energy.

5.2 Electron analysis

5.2.1 Cylindrically Clustered Results

Using the tracking information obtained from the BPCs, the point at which the beam particles strike the front face of the calorimeter can be determined. Cylindrical clusters are then formed by summing the energy of each cell within a certain radius of this

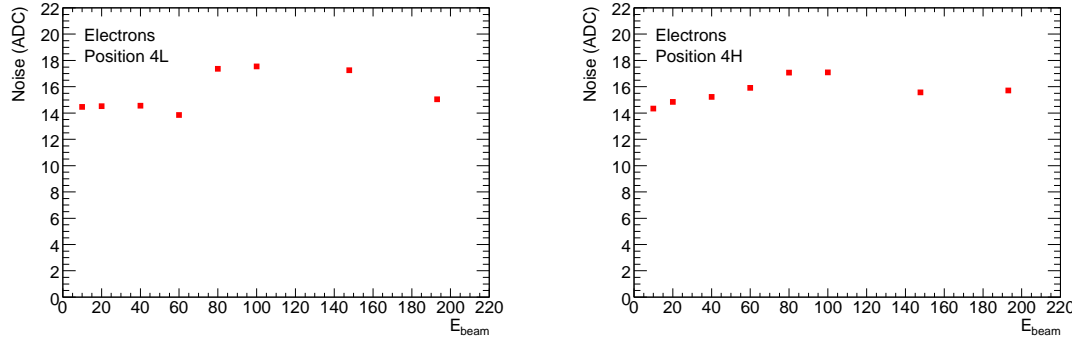


Figure 5.1: RMS of the electronics noise clustered at different energies, for electron beams directed at position 4L (left) and position 4H (right). **MOVE THESE PLOTS IN WITH RESPONSES?**

impact point. A clustering radius of 8 cm is used for analysis of the electron data. For electromagnetic showers, about 80-90% of the energy is contained within a cylinder of radius ρ_M , the Molière radius. The Molière radius in FCal1 is 17mm, and so about 99% of the shower's energy is contained within an 8 cm cluster, as can be seen in figure 5.2. Clusters with radii 12 cm and 16 cm are also generated during reconstruction. These larger clusters capture about 1% more energy than the 8 cm cluster, however the noise contained within the cluster increases by $\sim 50\%$ at a radius of 12 cm and $\sim 100\%$ at a radius of 16 cm. For this reason 8 cm clusters are used in the analysis of electron data.

The energy reconstructed for a given particle is dependent on the position at which that particle impacts the calorimeter, as an electron striking the centre of an electrode rod will deposit less visible energy in the calorimeter than one that impacts close to the liquid argon gap. As the diameter of the beamspot (65 mm) is an order of magnitude larger than the spacing between adjacent electrodes (7.5 mm in FCal1), many different impact points are sampled, which leads to a non-gaussian distribution in the response. A good fit to the data is obtained using a double gaussian function,

$$F(E) = A_1 \exp\left(-\frac{(E - m_1)^2}{2\sigma_1^2}\right) + A_2 \exp\left(-\frac{(E - m_2)^2}{2\sigma_2^2}\right) \quad (5.2)$$

where A_i , m_i , and σ_i are the peaks, means and widths of the component gaussians. The

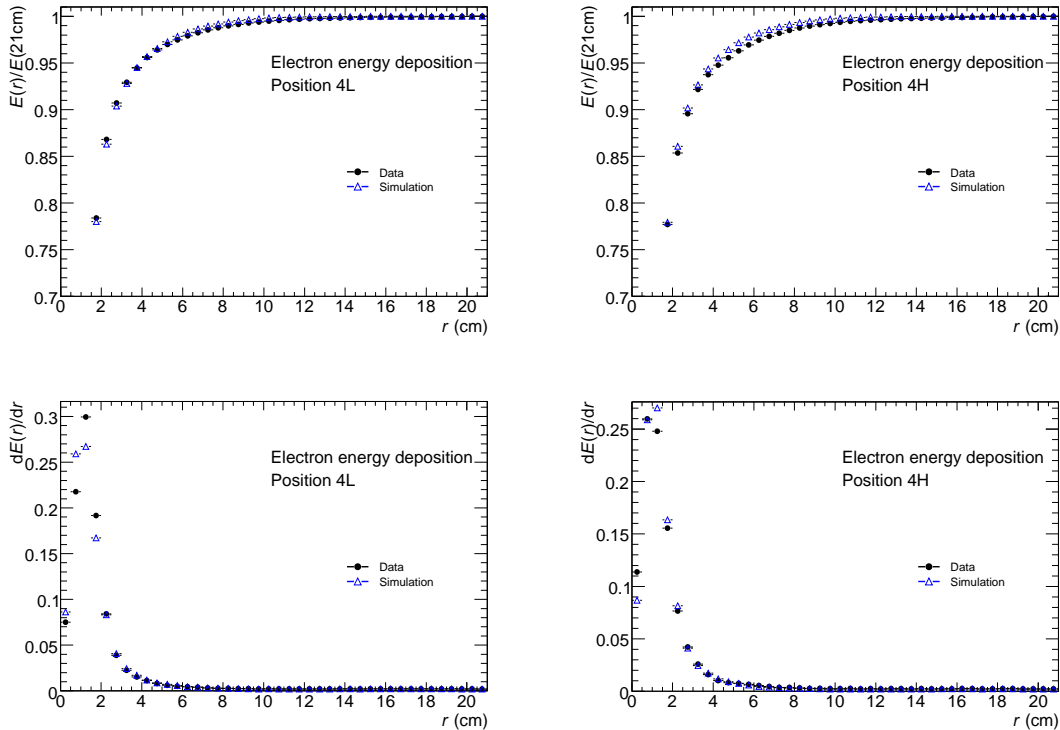


Figure 5.2: Energy contained in cylindrical clusters as a function of the clustering radius. Figures 5.2(a) and 5.2(b) show the fraction of energy contained within a cylindrical cluster of radius r compared to cluster of radius 21cm, for showers initiated by 193.1 GeV electrons at position 4L and 4H, respectively. Figures 5.2(c) and 5.2(d) show the fractional energy deposited between r and $r + dr$ as a function of r , for position 4L and 4H respectively.

mean response (\bar{E}) is taken as the first moment of $F(E)$, where the i -th moment, μ_i , is given by

$$\mu_i = \frac{\int_{E_{\min}}^{E_{\max}} E^i F(E) dE}{\int_{E_{\min}}^{E_{\max}} F(E) dE}, \quad (5.3)$$

where E_{\min} and E_{\max} are values obtained from the histogram of the energy response. The lower limit, E_{\min} , is taken from the low edge of the lowest energy bin that is not empty, while E_{\max} is the upper edge of the highest non-empty histogram bin. The width of the fit, σ , is determined from the second moment, such that

$$\sigma = (\mu_2 - \mu_1^2)^{1/2}. \quad (5.4)$$

Statistical uncertainties on these quantities may be written in terms of higher order moments. For simplicity, a (single) gaussian fit is made to the response, and the moments of this gaussian are used to compute the statistical uncertainties. The statistical uncertainties on the mean and width obtained from the fit are then

$$\Delta \bar{E} = \Delta \mu_1 = \frac{\sigma_g}{\sqrt{N_g}} \quad (5.5)$$

$$\Delta \sigma = \frac{\sigma_g}{\sqrt{2N_g}}, \quad (5.6)$$

where σ_g is the width of the (single) gaussian and N_g is the number of events contained within it (i.e. its integral).

The response of the FCal to electrons is plotted in figures 5.3 and 5.4, for beams directed at position 4L and 4H respectively. These results are summarized in tables 5.1 and 5.2. The properties of noise are obtained by reconstructing randomly triggered events. For each physics event, a randomly triggered event taken from the same run is chosen at random and reconstructed. The beam impact point from the physics event is used in the randomly triggered event, and a cylindrical cluster is formed around this point. A gaussian fit is then performed on the clustered energies, and the width of this

is used as an estimate of the noise present in the physics events. This width is used in the computation of the energy resolution, which is described below.

Beam Energy (GeV)	Fitted Mean (ADC)	Fitted Width (ADC)	Noise (ADC)
193.1 GeV	2300.6 ± 0.5	94.4 ± 0.3	15.1 ± 0.1
147.8 GeV	1763.4 ± 0.8	75.9 ± 0.5	17.2 ± 0.1
100 GeV	1186.4 ± 0.3	56.8 ± 0.2	17.5 ± 0.1
80 GeV	946.9 ± 0.3	47.9 ± 0.2	17.4 ± 0.1
60 GeV	708.1 ± 0.9	36.6 ± 0.7	13.9 ± 0.2
40 GeV	472.4 ± 0.2	29.9 ± 0.1	14.6 ± 0.1
20 GeV	229.3 ± 0.1	21.7 ± 0.1	14.5 ± 0.0
10 GeV	110.9 ± 0.1	17.7 ± 0.1	14.5 ± 0.1

Table 5.1: Results for the FCal response to electrons, directed at position 4L. Quoted errors are statistical only.

Beam Energy (GeV)	Fitted Mean (ADC)	Fitted Width (ADC)	Noise (ADC)
193.1 GeV	2263.9 ± 0.7	90.9 ± 0.5	15.7 ± 0.1
147.8 GeV	1718.3 ± 0.8	72.1 ± 0.5	15.6 ± 0.1
100 GeV	1150.8 ± 0.3	55.1 ± 0.2	17.1 ± 0.1
80 GeV	912.1 ± 0.3	48.8 ± 0.2	17.1 ± 0.1
60 GeV	680.1 ± 0.4	40.5 ± 0.2	15.9 ± 0.1
40 GeV	448.1 ± 0.2	30.9 ± 0.1	15.2 ± 0.1
20 GeV	215.8 ± 0.1	23.1 ± 0.1	14.9 ± 0.0
10 GeV	102.7 ± 0.1	18.5 ± 0.1	14.3 ± 0.1

Table 5.2: Results for the FCal response to electrons, directed at position 4H. Quoted errors are statistical only.

The simulated response to electrons is shown in figure 5.5 for position 4L and figure 5.6 for position 4H, and these results are summarized in tables 5.3 and 5.4. All of the physics lists listed in section?? model electromagnetic showers in the same way, and so no distinction among physics lists is made for the Monte Carlo results contained in this section.

The double gaussian fit is performed on the electron peak in the response distribution. While the beam envelope cuts improve the purity of the electron sample, some of these events still contain showers initiated by hadrons. The high tail of the hadron distribution

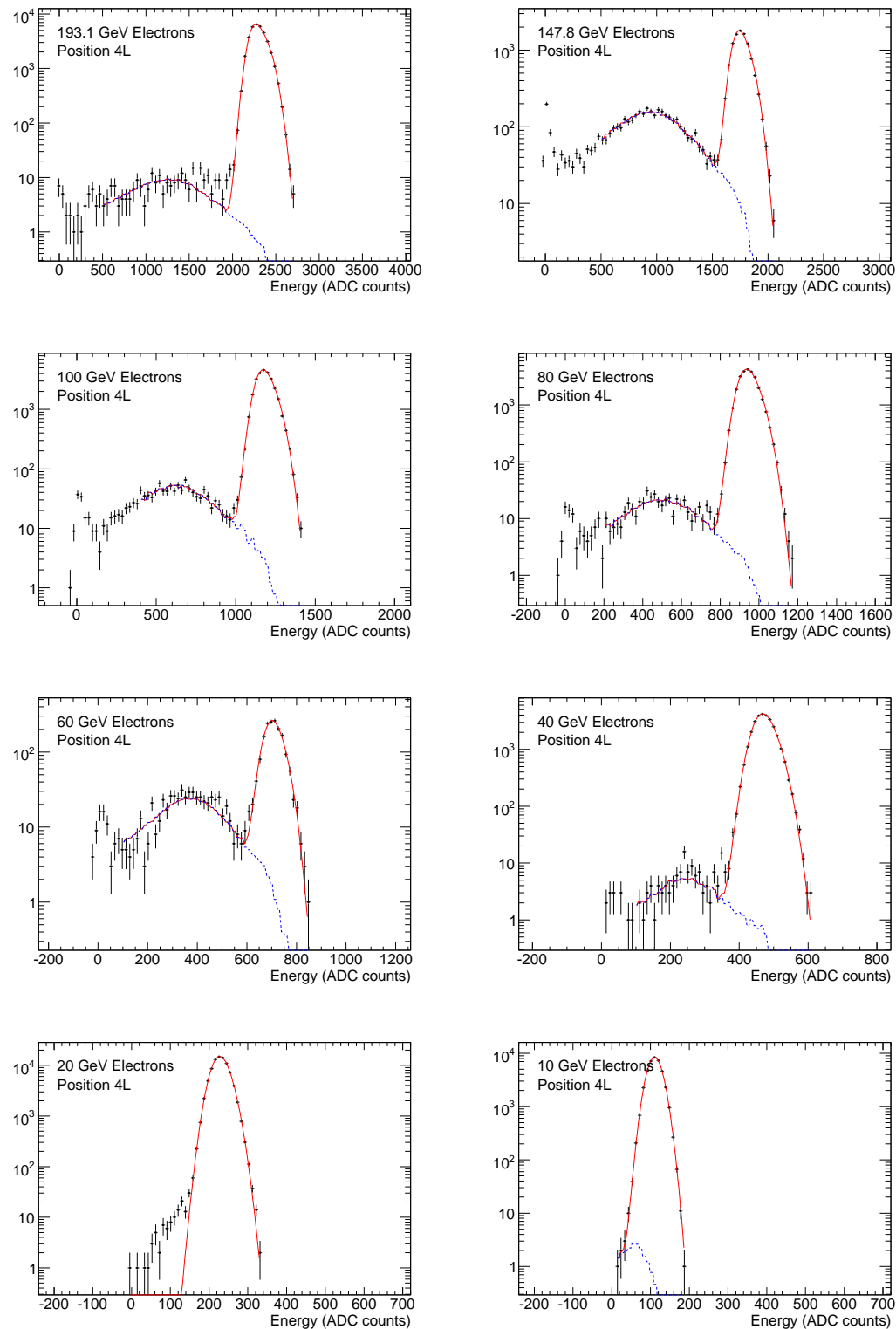


Figure 5.3: Response of the FCal to electrons directed at position 4L. The blue dashed curve shows the fit to the hadron contamination present in the data sample. The red curve is the total fit to the data, which consists of a double gaussian fit to the electron peak as well as the fit to the hadron contamination.

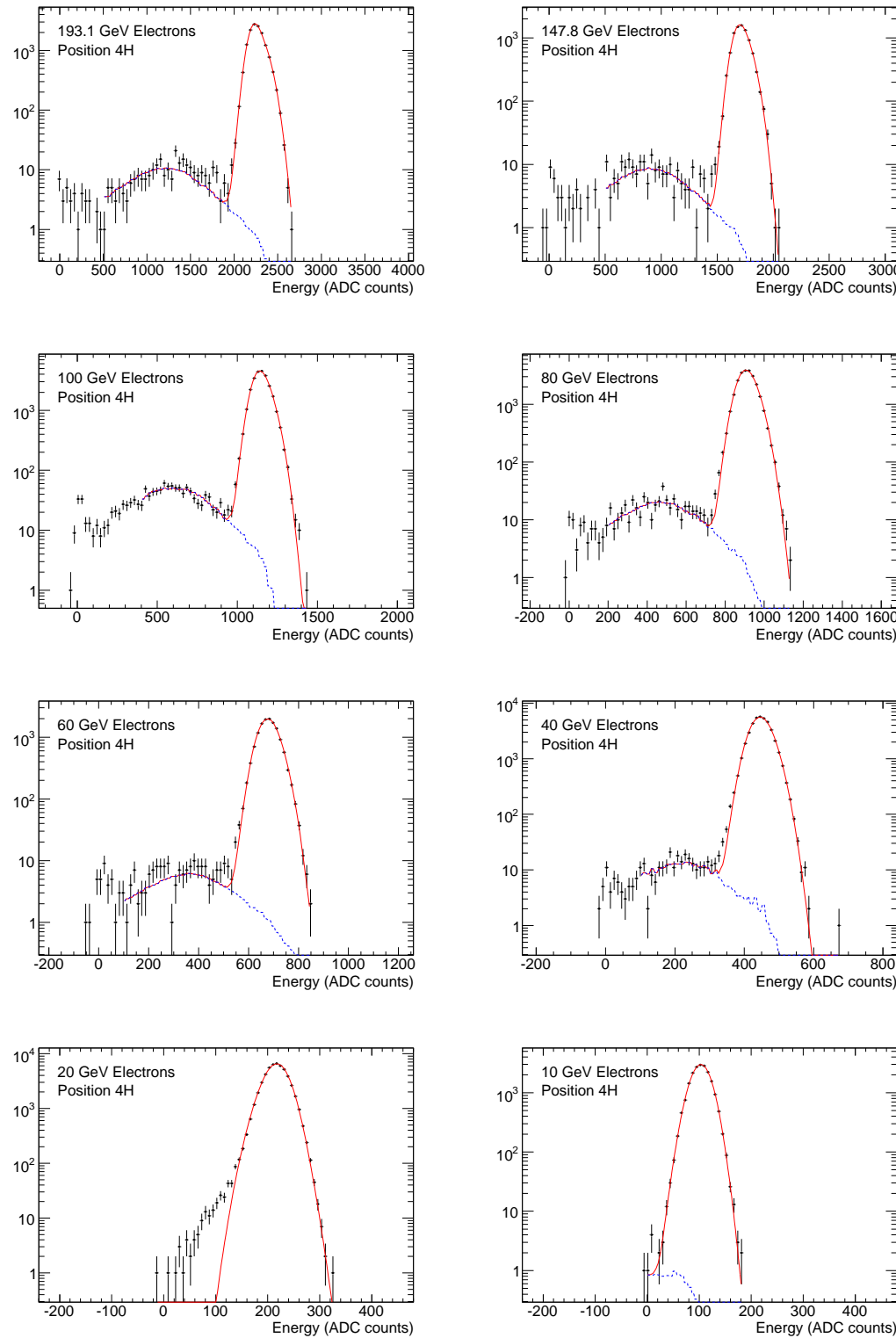


Figure 5.4: Response of the FCal to electrons directed at position 4H.

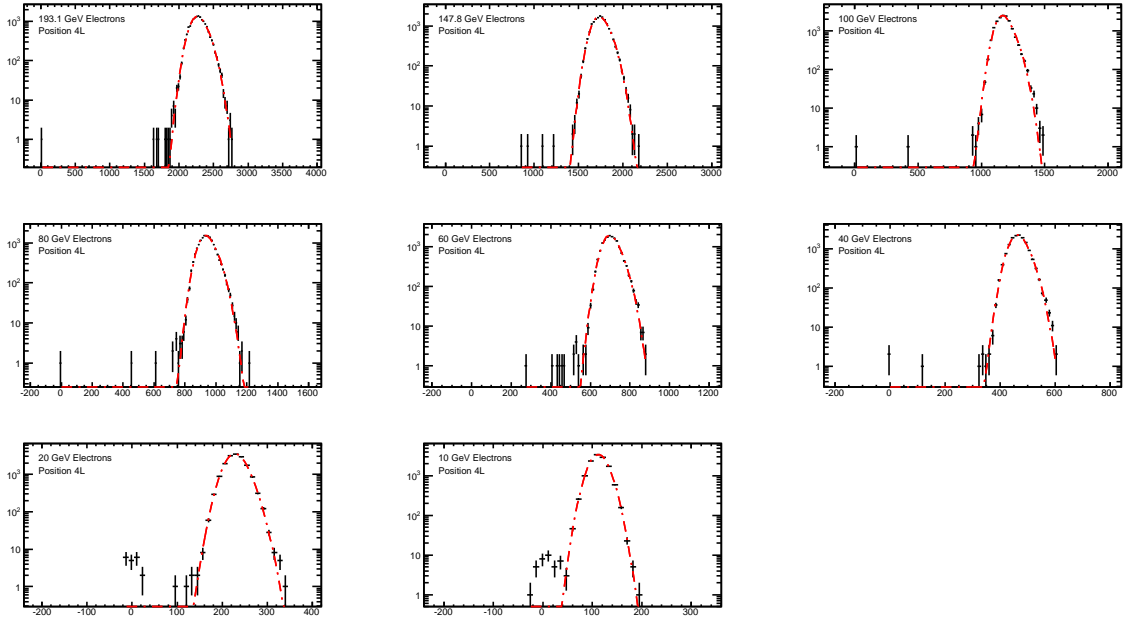


Figure 5.5: Monte Carlo results for electron beams directed at position 4L.

Beam Energy (GeV)	Fitted Mean (ADC)	Fitted Width (ADC)	Noise (ADC)
193.1 GeV	2285.2 ± 0.9	114.3 ± 0.7	14.2 ± 0.1
147.8 GeV	1747.4 ± 0.7	91.3 ± 0.5	17.0 ± 0.1
100 GeV	1180.2 ± 0.5	62.5 ± 0.3	17.4 ± 0.1
80 GeV	942.8 ± 0.4	51.7 ± 0.3	14.1 ± 0.1
60 GeV	705.3 ± 0.3	40.9 ± 0.2	14.2 ± 0.1
40 GeV	467.9 ± 0.3	31.6 ± 0.2	14.5 ± 0.1
20 GeV	230.5 ± 0.2	22.2 ± 0.1	14.3 ± 0.1
10 GeV	112.5 ± 0.2	18.0 ± 0.1	14.3 ± 0.1
5 GeV	53.1 ± 0.1	16.9 ± 0.1	14.1 ± 0.1

Table 5.3: Simulated response of the FCal to electron beams directed at position 4L. Quoted uncertainties are statistical only.

overlaps with the low tail of the electron peak, and this effect must be accounted for when analysing the data. This is accomplished by including data taken from hadron runs into the fit for the electron response. The total function fitted to the distributions shown in figure 5.3 is given by

$$G(E) = F(E) + w H_\pi(E), \quad (5.7)$$

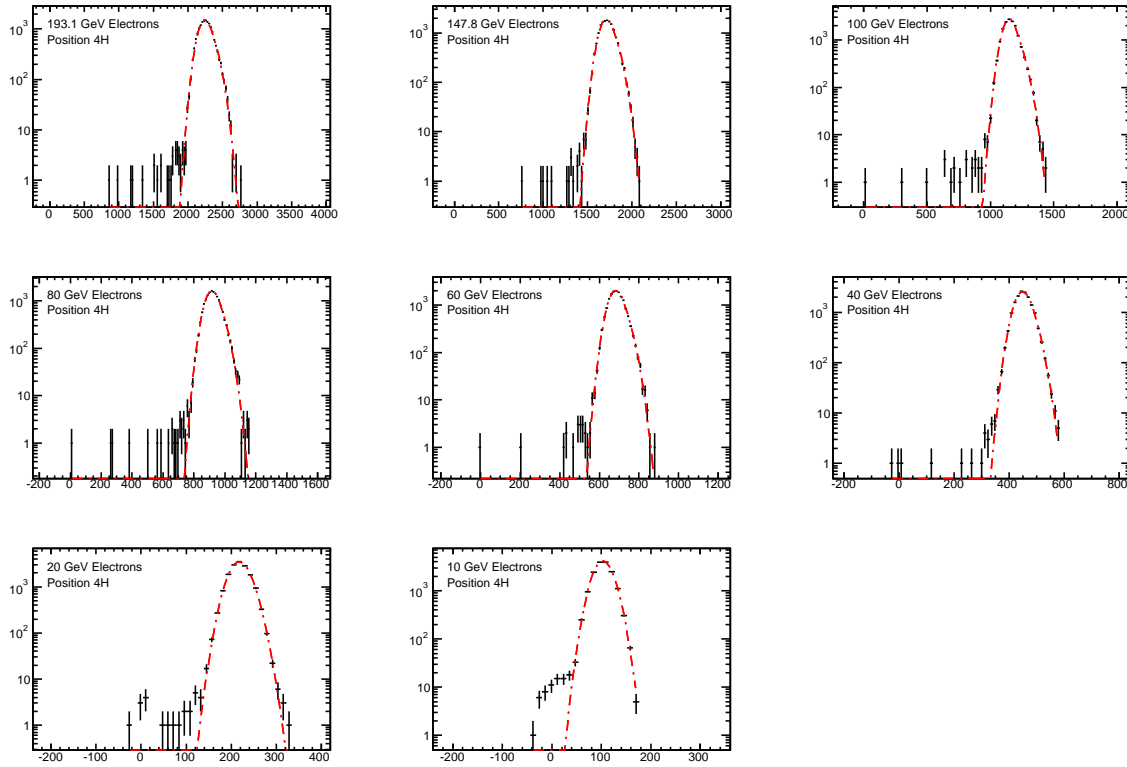


Figure 5.6: Monte Carlo results for electron beams directed at position 4H.

Beam Energy (GeV)	Fitted Mean (ADC)	Fitted Width (ADC)	Noise (ADC)
193.1 GeV	2259.7 ± 0.8	103.2 ± 0.6	15.9 ± 0.1
147.8 GeV	1723.5 ± 0.7	82.8 ± 0.5	15.6 ± 0.1
100 GeV	1159.5 ± 0.4	58.4 ± 0.3	17.0 ± 0.1
80 GeV	923.0 ± 0.4	48.2 ± 0.3	17.1 ± 0.1
60 GeV	687.7 ± 0.3	39.3 ± 0.2	16.1 ± 0.1
40 GeV	452.4 ± 0.2	30.7 ± 0.2	15.0 ± 0.1
20 GeV	218.8 ± 0.2	22.3 ± 0.1	14.6 ± 0.1
10 GeV	103.5 ± 0.1	18.4 ± 0.1	14.3 ± 0.1

Table 5.4: Simulated response of the FCal to electron beams directed at position 4H. Quoted uncertainties are statistical only.

where $F(E)$ is the double gaussian function described above. The “function” $H_\pi(E)$ is derived from data taken during pion runs. Cylindrical clusters with radius 8 cm are formed for each pion event, and used to fill a histogram with the same binning as is used for the electron response. The energy E is then converted to a bin number, and

the number of entries in this bin is taken as the value of $H_\pi(E)$. The parameter w corresponds to a weight for the hadron data and is allowed to freely vary in the fitting, as are the parameters of the double gaussian.

The two dominant sources of systematic uncertainties arise from the cluster radius and the beam polarity. The electron beams used in this study were secondary or tertiary beams produced by directing proton beams from the SPS at a fixed target. At higher energies a secondary beam was used, the polarity of which ($e+$ or $e-$) was determined based on the needs of other neighboring experiments. At lower energies a tertiary beam was used, and the polarity of this beam could be chosen freely.

Data was taken at position 4L using both $e-$ and $e+$ beams at energies of 10 GeV and 20 GeV. Physically, electromagnetic showers induced by electrons should on average deposit the same energy as those initiated by positrons. The 10 GeV and 20 GeV results in figure 5.3 use data obtained from both $e+$ and $e-$ beams. Considered separately, the response to 10 GeV positrons is on average 1.6% higher than the response to electrons. At 20 GeV, the response to positrons is 1.0% higher than the response to electrons. This difference in response is attributed to variation in the beam conditions, and is considered as a source of systematic uncertainty.

As mentioned above, a larger clustering radius captures a slightly larger fraction of the showering particles energy, while significantly increasing the amount of noise present in the cluster. The choice of clustering radius is thus taken as a source of systematic uncertainty. Other systematic effects considered include the binning used in histograms, inclusion of the pion response in the electron fit, the parameterization used for the fit, and event selection criteria.

Linearity plots are shown in figures 5.7(a) (for position 4L) and 5.7(b) (position 4H), depicting the mean reconstructed energy as a function of beam energy. A linear fit has been applied to the plots, the results of which are given in table 5.12. The y intercept of the line was not fixed at zero when performing the fit, and was instead allowed to vary.

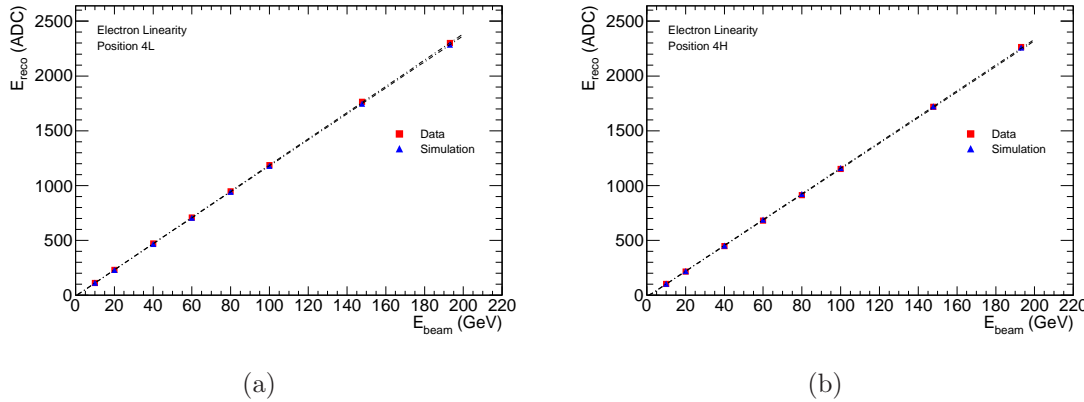


Figure 5.7: Linearity of the response to electrons at position 4L (left) and 4H (right).

linearity result	slope (ADC/GeV)	Intercept (ADC)
Data (4L)	11.964 ± 0.002	-9.26 ± 0.07
Simulation (4L)	11.865 ± 0.003	-6.45 ± 0.13
Data (4H)	11.693 ± 0.002	-17.53 ± 0.10
Simulation (4H)	11.747 ± 0.003	-15.44 ± 0.13

Table 5.5: Linearity results for electron data. quoted uncertainties are statistical.

The negative result for the intercept is due to energy losses in the upstream material, with the additional material at 4H giving an intercept larger in magnitude than that at 4L. As the simulation only modeled the beamline downstream of the B9 magnet, energy losses in materials upstream of this point would not be reflected in the simulation results. This is a possible explanation as to why the simulation results have a higher (less negative) intercept than those obtained from data.

The linearity shown in figure 5.7(a) uses events from both e^+ and e^- runs at 10 GeV and 20 GeV, which is considered to be the "nominal" case. The systematic uncertainty on the linearity due to beam polarity effects is obtained by varying the data used at 10 GeV and 20 GeV. At each of each of these energies, the response may be determined using events from e^+ runs, events from e^- runs, or events from either e^+ or e^- runs. A fit to the linearity is performed for each of these cases, and compared to the nominal result. The largest difference observed for each parameter is taken as the systematic uncertainty

due to beam polarity effects. At position 4H, only a single beam polarity was used at each energy, with e^+ beams being used at 10 GeV and 20 GeV. To obtain the uncertainty due to beam effects the responses at these points was scaled by the $e^+ : e^-$ response ratio observed at 4L, in order to estimate the response to e^- beams. This yielded four different response combinations, which were then used to estimate the systematic uncertainty.

Other sources of systematic were treated in a similar fashion. For example, the effect of the cluster radius was estimated by using 12cm and 16cm clusters. A fit was performed on the resulting linearity plots, and the fit parameters were compared to those obtained using 8 cm clusters, with the largest difference taken as the uncertainty on that parameter. Systematic uncertainties from different sources were then summed in quadrature to obtain the final uncertainty on the results.

The linearity at position 4L is best described by a line with slope $12.0 \pm 0.1 \text{ADC/GeV}$ and intercept -9.3 ± 1.1 ADC counts, where the quoted uncertainties are due to systematic effects. At position 4H, the linearity is described by a line with slope $11.7 \pm 0.2 \text{ADC/GeV}$ and intercept -17.5 ± 1.6 ADC counts. A prediction of the ADC2GeV calibration factor was made prior to the beam test, based on a simulation of the FCal electronics chain and knowledge of the FCal geometry. The predicted value for FCal1 was found to be 12.0 ADC/GeV [2], in good agreement with the results obtained here.

The residuals obtained from the linearity fits are plotted in figure ???. Systematic uncertainties on the residuals were estimated using the method described above. When performing a fit on the data, the difference between the resulting set of residuals and the nominal residuals is taken as the uncertainty on the residuals due to that particular source of systematic error. The uncertainties from different sources are then summed in quadrature. From the plot in figure ???, it can be seen that the response at position 4L is linear to within 1%. This is also the case at position 4H for energies of 20 GeV and above.

The energy resolution of the FCal to electrons is plotted in figure 5.9. As the randomly

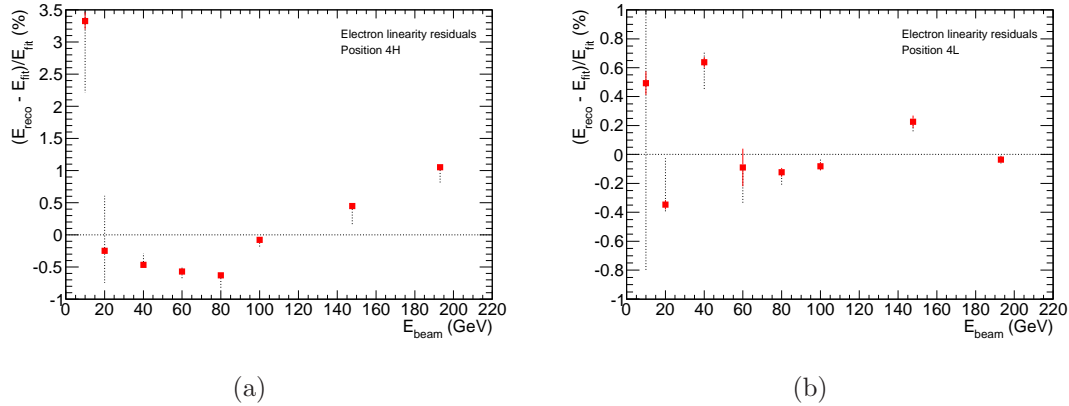


Figure 5.8: Residuals obtained from the linearity fit for electrons at position 4L (left) and 4H (right). Solid lines in the error bars represent the statistical uncertainties, while the systematic uncertainties are represented by the dotted lines.

triggered events provide information on the amount of noise present in the electronics, the contribution of this noise has been subtracted in quadrature from the width of the response. The resolution is thus defined as σ_E/\bar{E} , where

$$\sigma_E = \sqrt{\sigma^2 - \sigma_N^2} \quad (5.8)$$

where σ_N is the width of the noise distribution obtained from randomly triggered events and σ is the width of the response. The width, σ , is obtained from the double gaussian fit as described by equation 5.4, and the obtained values are listed in tables 5.1 and 5.2.

The resolution is fit to a function of the form

$$\frac{\sigma_E}{E} = \left(\frac{A^2}{E/GeV} + B^2 \right)^{\frac{1}{2}}, \quad (5.9)$$

where A is the called the stochastic term, and represents the contribution to the resolution arising from fluctuations in the energy deposited in the liquid argon gaps of the FCal. The constant term, B , is due to energy independent effects on the resolution, such as non-uniformities in the calorimeter structure. A term proportional to E^{-2} is sometimes

included in equation 5.9 to describe the effects of noise on the resolution. As the noise has been accounted for by the subtraction procedure described above, this term has been omitted. The fit results are listed in table 5.6.

	Stochastic Term (% GeV ^{1/2})	Constant Term (%)
Data (4L)	27.0 ± 0.2	3.58 ± 0.02
Simulation (4L)	24.7 ± 0.3	4.56 ± 0.03
Data (4H)	33.7 ± 0.2	3.11 ± 0.03
Simulation (4H)	28.1 ± 0.3	3.96 ± 0.03

Table 5.6: Fit parameters for energy resolution to electrons. Quoted uncertainties are statistical only.

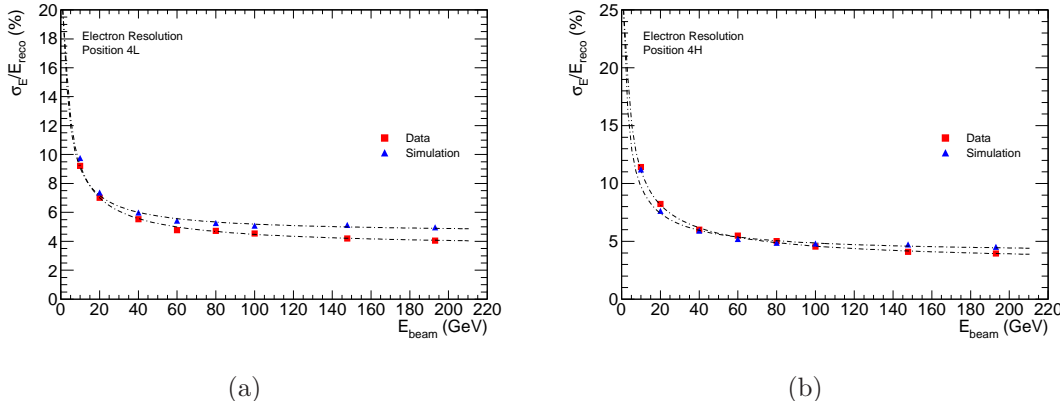


Figure 5.9: Energy resolution of the FCal to electrons, using data taken from position 4L (left) and 4H (right). A noise subtraction procedure has been applied, as described in the text.

The non-uniformity of the response with respect to the beam particles impact point on the calorimeter forms the dominant contribution to the constant term in the resolution. The additional upstream material present for runs directed at position 4H causes the beam particles to begin showering earlier. The energy in the shower is thus distributed over a larger area by the time it reaches the FCal, decreasing the impact point dependence and resulting in a lower constant term for the resolution measured at position 4H. The simulation results for electrons give a lower (i.e. better) resolution than that seen in data, although the discrepancy is smaller at position 4H than 4L.

5.2.2 Hadron Results

In the analysis of hadron data, the signal from the FCal is first calibrated to the electromagnetic (EM) scale. This is done by applying ADC2MeV factors, which convert the reconstructed pulse peak (in ADC counts) to the corresponding energy that would be deposited in the calorimeter by an electromagnetic particle (i.e. an electron or photon). The ADC2MeV values used in the reconstruction are 83.3 MeV/ADC, 163.9 MeV/ADC and 185.2 MeV/ADC for FCal1, FCal2 and FCal3 respectively, and were obtained from a SPICE simulation of the FCal electronics. As discussed above, the predicted value for FCal1 is in good agreement with the value obtained from the linearity of the FCal1 response to electrons. Data taken in a previous beam test allowed the ratio of the FCal1 and FCal2 responses to be studied, and the SPICE results agree with this data to within 5%.

Figure 5.10 shows the transverse distribution of energy (at the EM scale) for 200 GeV hadrons showering within the FCal. Figures 5.10(a) and 5.10(c) show the energy deposited within a transverse distance r from the impact point, as a fraction of the energy deposited within 21cm of the impact point. Figures 5.10(b) and 5.10(d) show the derivatives of these functions. The Monte Carlo results (for all physics lists studied) show that a larger fraction of the energy is contained within smaller transverse distances, indicating that the simulated showers are smaller than those observed in data.

Cylindrical clusters with radius 16cm are used for analysis of the hadron data. The longitudinal shower profiles for 200 GeV hadrons are shown in figure 5.12. These show the amount of energy (at the EM scale) clustered within each module as a fraction of the total energy clustered in all modules. The Monte Carlo results deposit more energy in FCal1 and less energy in FCal2, indicating the the simulated showers are shorter than those observed in data. The shower maximum is the point at which the particle shower contains the largest number of particles, and thus corresponds to the depth at which the rate of energy deposition is greatest. The additional material in front of position 4H

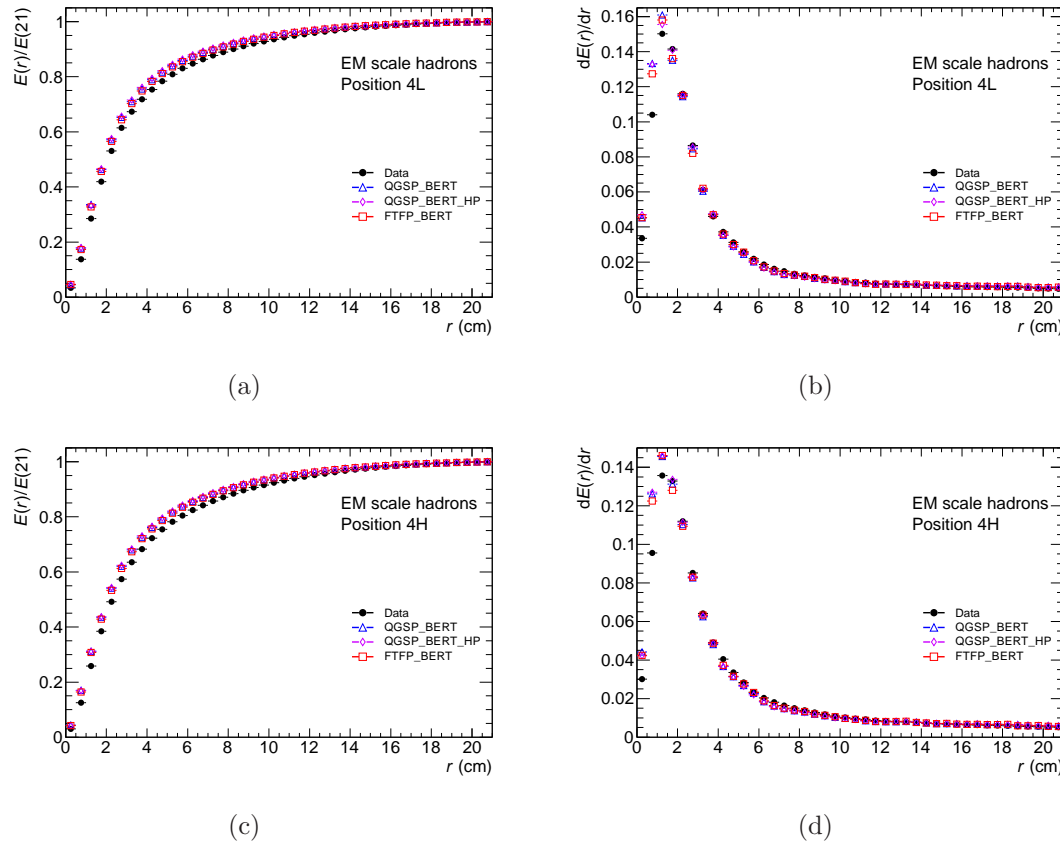


Figure 5.10: Energy distribution within the FCal as a function of the transverse distance (r) from the projected beam impact point. Results obtained from position 4L are shown in the upper row, while results from position 4H are in the lower row. Figures 5.10(c) and 5.10(a) shows the cumulative energy distribution while figures 5.10(b) and 5.10(d) show the derivatives of these plots.

causes the shower to start earlier, and thus moves the location of the shower maximum back towards the front of the FCal. This results in a larger fraction of energy being deposited in FCal1 at position 4H compared to position 4L.

The mean response of the FCal to hadrons is plotted in figure 5.12, as a function of the beam energy. The response here is taken at the EM scale. One feature of hadronic showers is that not all of the shower's energy is visible to the calorimeter. For example, when a nucleus breaks up as a result of an interaction with a showering hadron, an amount of nuclear binding energy is lost from the products of the reaction. Alternatively, a hadronic

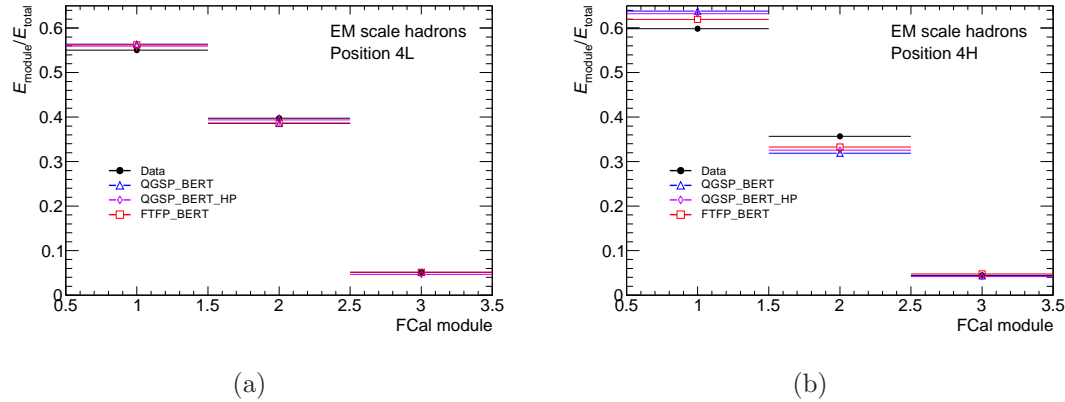


Figure 5.11: Longitudinal distributions of energy deposited in the FCal. These show the relative amounts of energy clustered in each module, for beams directed at position 4L (left) and 4H (right).

interaction may produce a neutrino, which will carry energy out of the detector. Energy lost in processes such as these cannot be measured by the calorimeter, resulting in a response lower than that of an EM particle with the same energy. For this reason, the energy reconstructed at the EM scale is only around 60-80% of the beam energies considered in this analysis. Some particles produced in hadronic interactions, such as η and π^0 mesons, decay to photons which then shower electromagnetically. Hadronic showers thus have an EM component, and the relative amount of the shower energy that is carried by this EM component increases with the energy of the initial hadron. It is this behaviour that gives rise to the non-linear shape seen in figure 5.12.

The measured energy is calibrated to the hadronic scale through a flat weighting scheme, whereby a single weight is assigned to each module. The calibrated energy is then given by

$$E_{\text{reco}} = g_1 E_1^{\text{EM}} + g_2 E_2^{\text{EM}} + g_3 E_3^{\text{EM}} \quad (5.10)$$

where E_1^{EM} , E_2^{EM} , and E_3^{EM} are the EM scale energies clustered in FCal1, FCal2 and FCal3, respectively, and g_1 , g_2 , and g_3 are the flat weights for these modules.

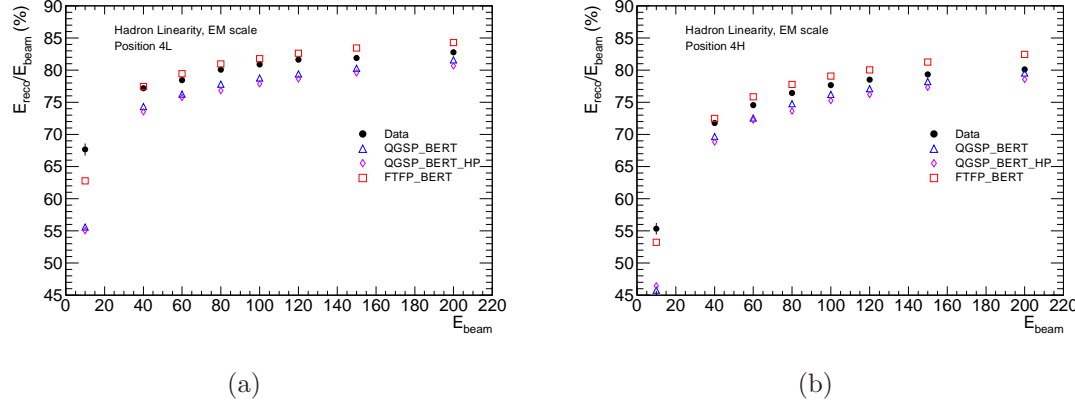


Figure 5.12: Ratio of energy reconstructed at the EM scale to the beam energy, for hadrons directed at position 4L (left) and 4H (right).

The weights are derived at a given beam energy, and are found by minimising the function

$$\chi^2 = \sum_i^{N_{\text{events}}} (g_1 E_{1,i}^{\text{EM}} + g_2 E_{2,i}^{\text{EM}} + g_3 E_{3,i}^{\text{EM}} - E_{\text{beam}})^2 \quad (5.11)$$

where E_{beam} is the beam energy and the sum over i runs over all events taken at this energy. The weights are constrained such that the mean reconstructed energy is equal to the beam energy. This constraint is implemented by assigning g_3 the value

$$g_3 = \frac{E_{\text{beam}} - g_1 \langle E_2^{\text{EM}} \rangle - g_2 \langle E_2^{\text{EM}} \rangle}{\langle E_3^{\text{EM}} \rangle}, \quad (5.12)$$

where the angled brackets denote the average taken over all events. With this constraint applied, χ^2 in equation 5.11 becomes equal to the variance of the reconstructed energy, and so minimising χ^2 minimises the width of the distribution of reconstructed energy.

The flat weights derived at each energy are plotted in figure ???. Weights derived using Monte Carlo results are also shown for comparison, but are not used in the analysis: weights derived from 200 GeV data are used to calibrate all data and simulation results to the hadronic scale. As the beam energy decreases the relative amount of energy deposited in FCal1 and FCal2 increases, while that deposited in FCal3 decreases. At 10 GeV less energy is deposited in FCal2, and so the weight g_2 drops while g_1 rises suddenly.

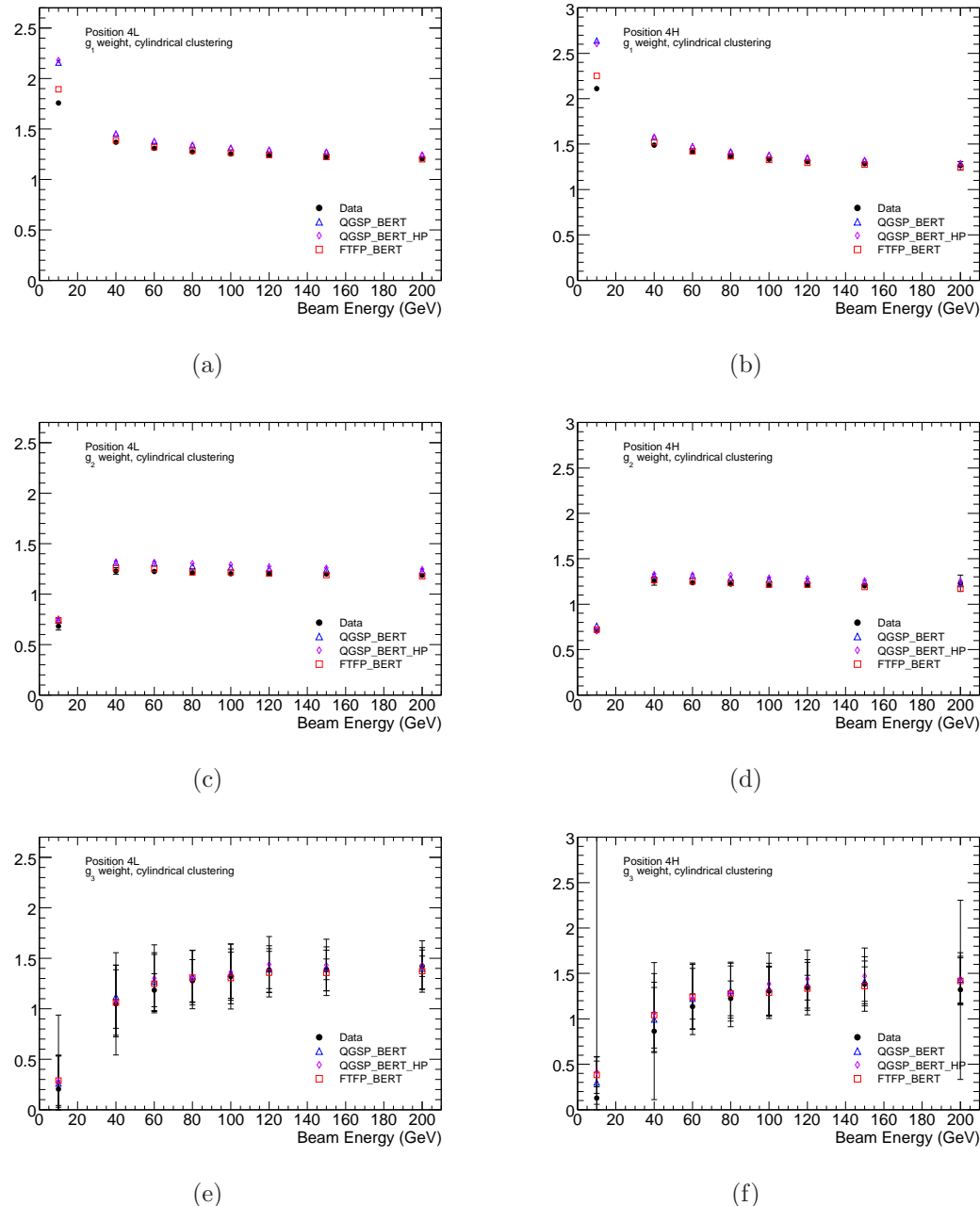


Figure 5.13: Flat weights used in hadronic calibration, as a function of the energy at which they are derived. Only the weights derived using 200GeV are used in the analysis.

The uncertainty on g_3 is found by propagating the statistical uncertainties on g_1 and g_2 . As FCal3 contains a small fraction of the total energy deposited in the FCal, even at high beam energies, this results in an uncertainty on g_3 that is much larger than the uncertainties on the other two weights.

The hadronic response of the FCal is plotted in figures 5.14 (4L) and 5.14 (4H). A double gaussian is fitted to the response and used to extract the mean and width, as was done in the electron analysis. The results obtained from the fitting are summarised in tables 5.7 and 5.8.

Beam Energy (GeV)	Fitted Mean (GeV)	Fitted Width (GeV)	Noise (GeV)
200 GeV	200.1 ± 0.1	19.5 ± 0.0	6.4 ± 0.0
150 GeV	148.4 ± 0.0	16.1 ± 0.0	6.5 ± 0.0
120 GeV	118.3 ± 0.0	14.2 ± 0.0	6.8 ± 0.0
100 GeV	97.7 ± 0.1	13.4 ± 0.1	7.3 ± 0.0
80 GeV	77.3 ± 0.1	11.3 ± 0.0	6.5 ± 0.0
60 GeV	56.7 ± 0.0	9.6 ± 0.0	6.1 ± 0.0
40 GeV	37.2 ± 0.1	8.5 ± 0.1	6.1 ± 0.0
10 GeV	8.2 ± 0.1	6.6 ± 0.1	6.2 ± 0.1

Table 5.7: Results for the FCal response to hadrons directed at position 4L. Quoted errors are statistical only.

Beam Energy (GeV)	Fitted Mean (GeV)	Fitted Width (GeV)	Noise (GeV)
200 GeV	201.0 ± 0.1	23.4 ± 0.0	6.5 ± 0.0
150 GeV	149.5 ± 0.1	19.1 ± 0.1	6.4 ± 0.0
120 GeV	118.4 ± 0.1	17.1 ± 0.0	7.2 ± 0.0
100 GeV	97.5 ± 0.1	15.9 ± 0.1	7.6 ± 0.0
80 GeV	76.7 ± 0.1	14.1 ± 0.0	7.6 ± 0.0
60 GeV	56.1 ± 0.0	11.7 ± 0.0	6.7 ± 0.0
40 GeV	36.1 ± 0.1	9.9 ± 0.1	6.5 ± 0.1
10 GeV	7.0 ± 0.1	7.2 ± 0.1	6.4 ± 0.1

Table 5.8: Results for the FCal response to hadrons directed at position 4H. Quoted errors are statistical only.

The ratio of mean reconstructed energy at the hadronic scale to the beam energy is plotted in figure 5.17. As most of the energy is deposited in FCal1 and FCal2, which

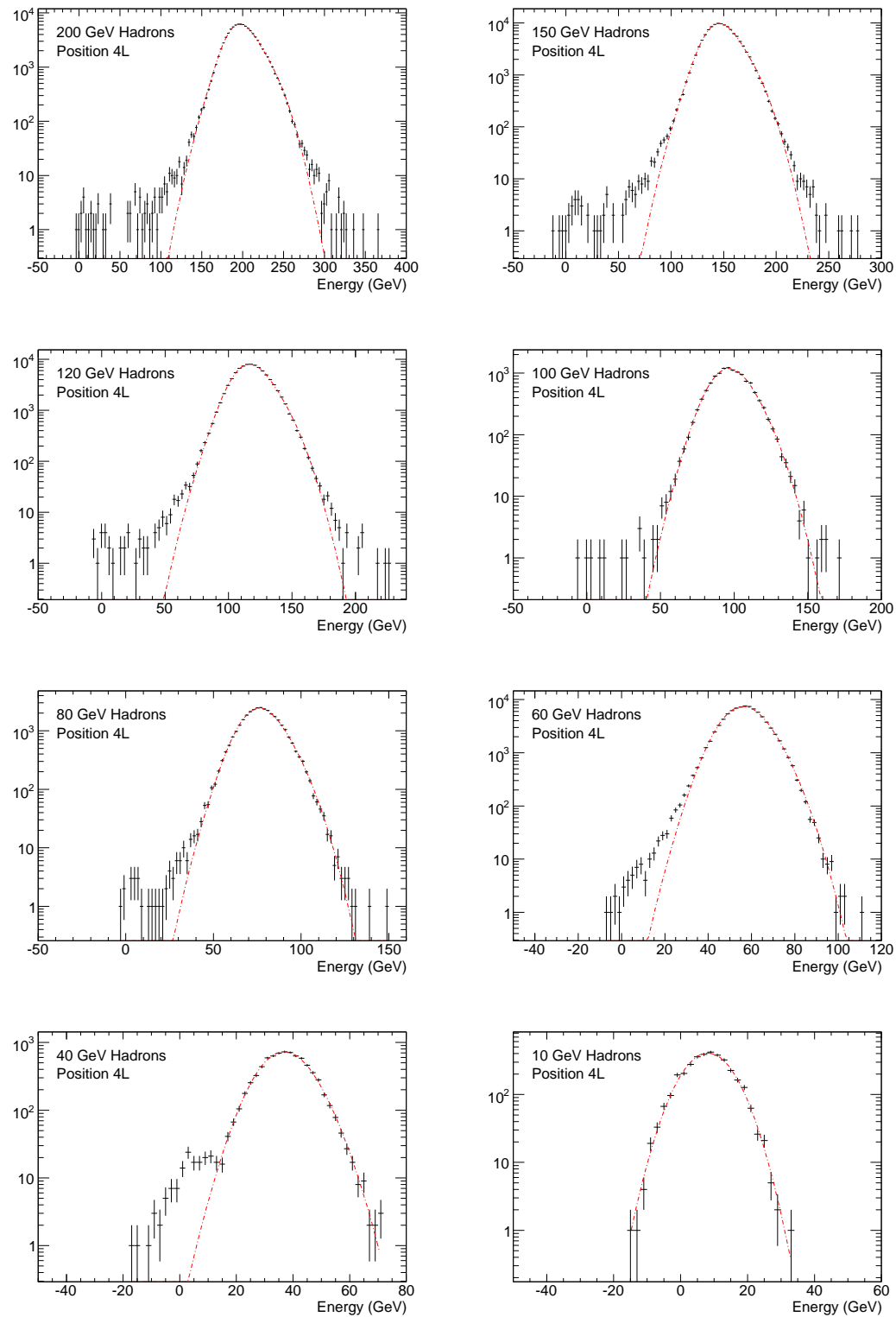


Figure 5.14: FCal response to hadron beams directed at position 4L.

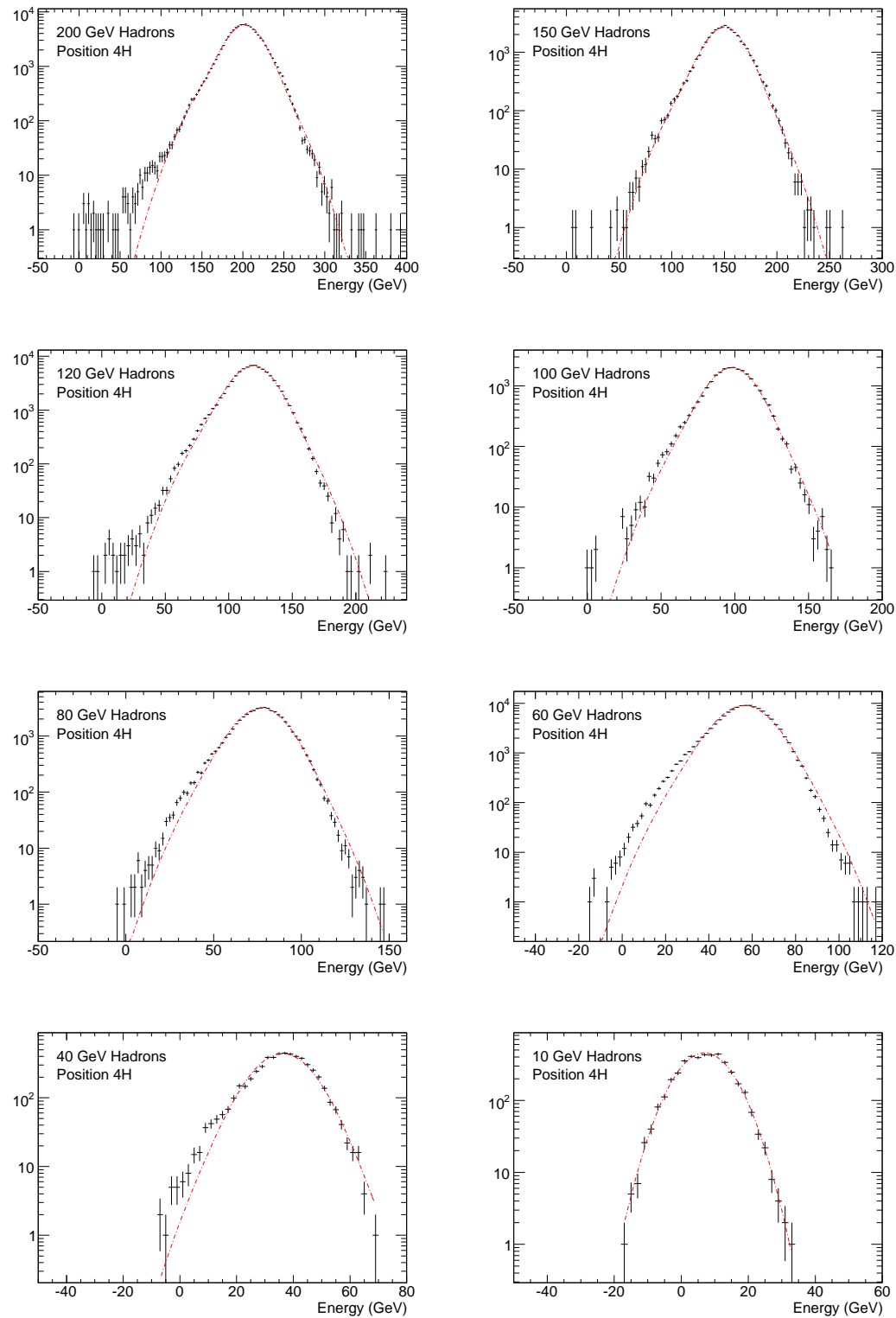


Figure 5.15: FCal response to hadron beams directed at position 4H.

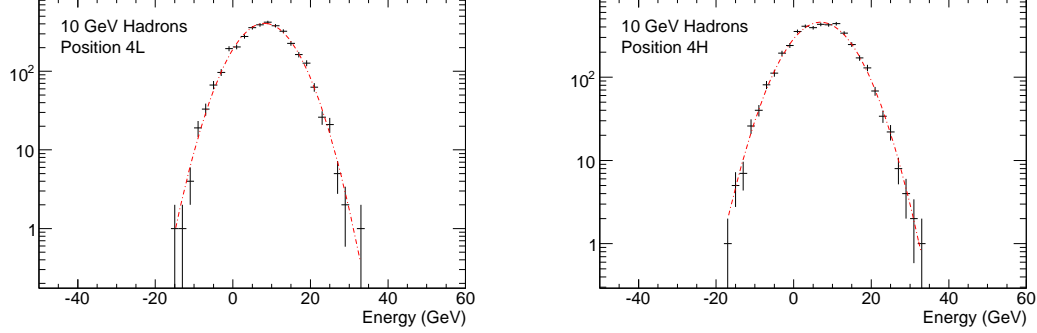


Figure 5.16: RMS of the electronics noise contribution to cylindrical clusters at position 4L (Fig. 5.16(a)) and position 4H (Fig. 5.16(b)).

have similarly valued weights at 200 GeV, the shape of these plots are very similar to those shown in figure 5.12.

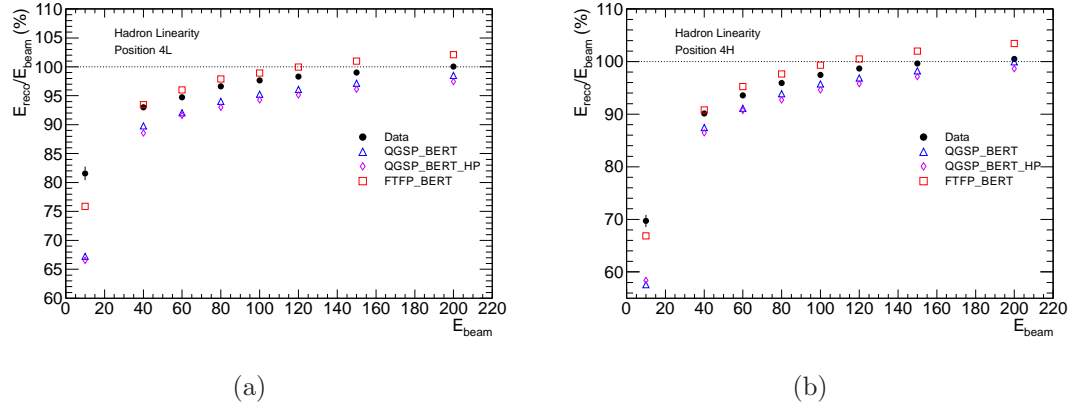


Figure 5.17: Ratio of reconstructed energy to beam energy for hadrons directed at position 4L (left) and 4H (right). Hadronic calibration is accomplished through flat weights, which are derived from the 200GeV data.

The energy resolution of the FCal to hadrons is plotted in figure 5.18. At higher energies the data and simulation results agree to within a 1-2% percent. The resolution information is fit to the same function used for electrons; the results of which are listed in table 5.9.

Systematic effects on the resolution are dominated by the choice of weights used for hadronic calibration. The weights derived at 100GeV, 120GeV and 150 GeV are used to

estimate this uncertainty. Each set of weights is used to calibrate the data and obtain information on the resolution, which is then fit. The largest deviation seen between the fits obtained using these weights and the nominal set of weights (which are derived at 200 GeV) is then taken as the systematic uncertainty. Uncertainties related to the fitting procedure, histogram binning and event selection criteria are also considered, with uncertainties arising from different sources being summed in quadrature. The values for the stochastic and constant term of the resolution at position 4L are thus $88 \pm 3\%$ $\text{GeV}^{1/2}$ and $6.8 \pm 0.4\%$, respectively, where the quoted uncertainties are systematic. For position 4H, the stochastic and constant term are $121 \pm 7\text{ GeV}^{1/2}$ and $7.1 \pm 1.2\%$, respectively.

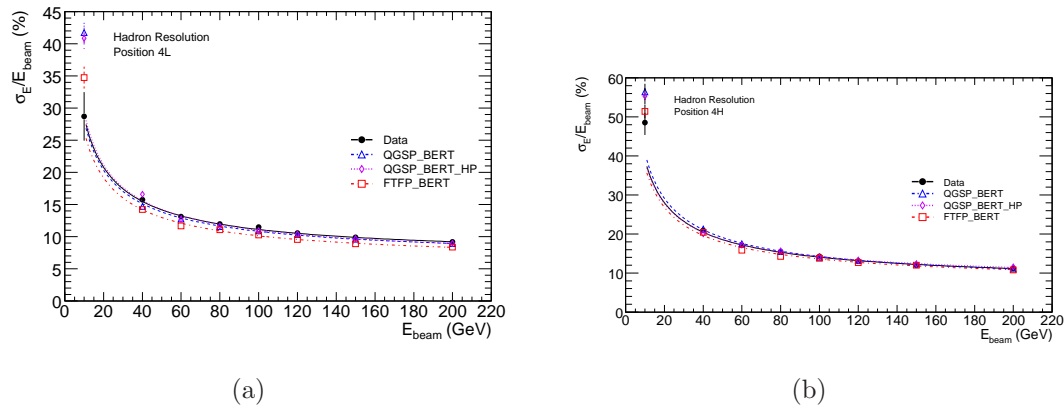


Figure 5.18: Energy resolution of the FCal to hadrons, using data taken from position 4L (left) and 4H (right). A noise subtraction procedure has been applied, as described in the text.

	Stochastic Term (% GeV ^{1/2})	Constant Term (%)
Data (4L)	88.0 ± 0.6	6.79 ± 0.06
QGSP_BERT (4L)	86.2 ± 1.1	6.54 ± 0.18
QGSP_BERT_HP (4L)	90.5 ± 1.1	6.22 ± 0.13
FTFP_BERT (4L)	81.2 ± 1.1	6.04 ± 0.11
Data (4H)	121.3 ± 0.6	7.13 ± 0.07
QGSP_BERT (4H)	127.2 ± 1.1	6.41 ± 0.17
QGSP_BERT_HP (4H)	119.6 ± 1.2	7.71 ± 0.15
FTFP_BERT (4H)	115.8 ± 1.1	7.12 ± 0.14

Table 5.9: Fit parameters for energy resolution to electrons. Quoted uncertainties are statistical only.

5.3 Topologically Clustered Results

5.3.1 Electrons

In addition to cylindrical clusters, topological clusters (as described in section ??) are formed during the reconstruction of each event. The clustering is done in `Athena` using the standard "420" thresholds. The noise values used to define these thresholds are obtained from randomly triggered data. In `ATLAS`, the tracking detectors do not cover the pseudorapidity region in which the FCal is located. Topological clusters do not require tracking information for their formation, and thus they can be used to measure energy deposited in the FCal during data taking at the LHC.

The topoclustering software in `Athena` contains a splitting step [13], which is enabled by default. The splitter is intended to form new cluster within existing clusters, in cases where the new clusters can be associated with energy deposited by individual particles. New clusters are formed around local maxima, which are cells that satisfy the following conditions:

- have more energy than any adjacent cells
- have at least 4 neighboring cells belonging to the original cluster
- have energy greater than 500 MeV

As the RMS of the noise in the hadronic modules of the FCal is close to 500 MeV, the splitter has been turned off in this analysis in order to prevent noise fluctuations from creating new clusters.

The response of the FCal to electrons is shown in figures 5.19 and 5.19, for beams directed at position 4L and 4H respectively. As with the cylindrically results, the response is fit to the sum of a double gaussian (for the electron peak) and an contribution derived from hadron data in order to account for any residual beam contamination. Quantities obtained from the fit are listed in tables 5.10 and 5.11

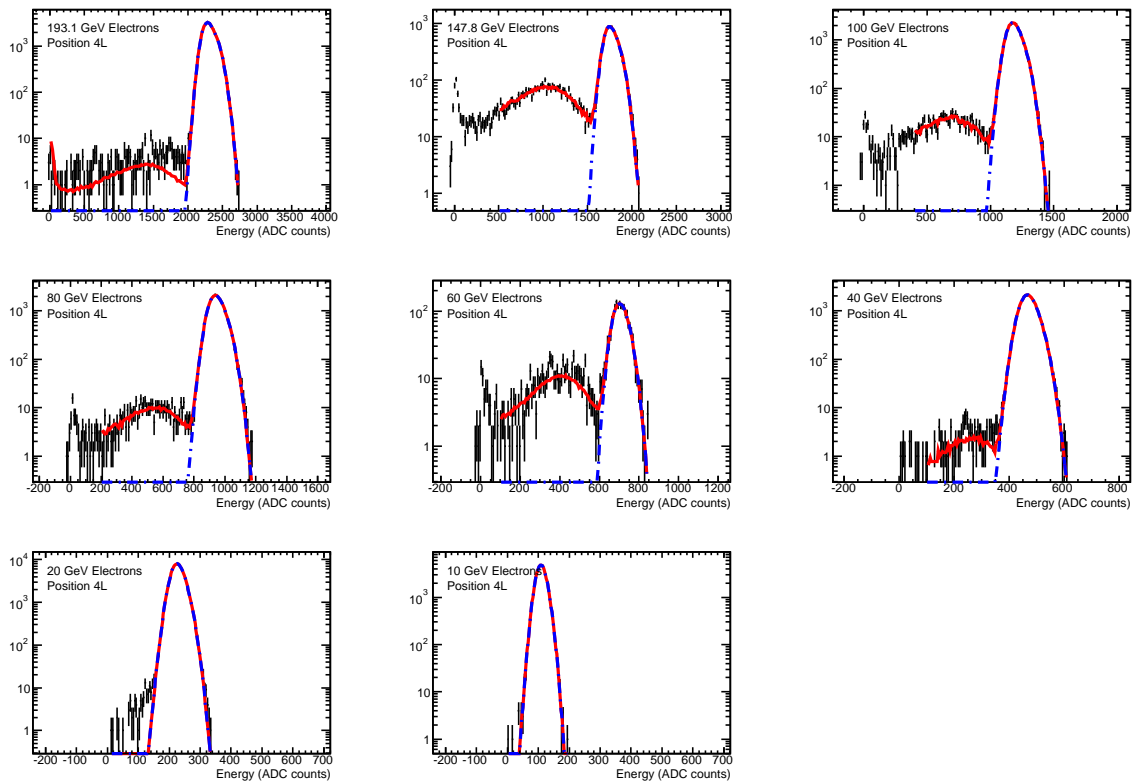


Figure 5.19: FCal response to electron beams directed at position 4L. The lower-right plot shows the clustered noise (in GeV) at each energy.

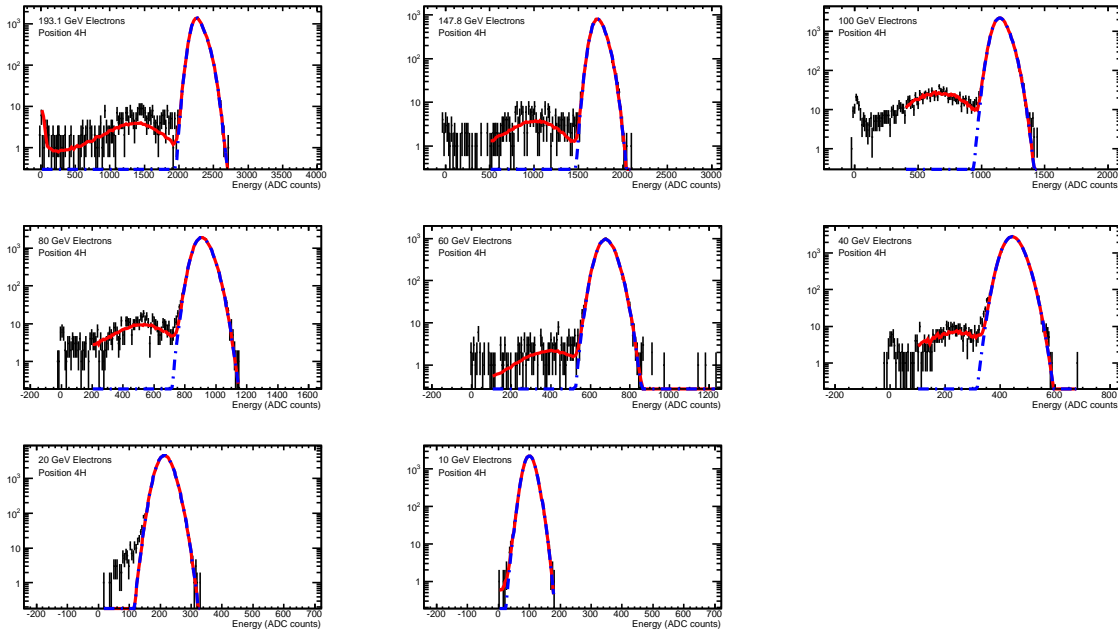


Figure 5.20: FCal response to electron beams directed at position 4H, .

Beam Energy (GeV)	Fitted Mean (ADC)	Fitted Width (ADC)	Noise (ADC)
193.1 GeV	2312.4 ± 0.5	95.4 ± 0.3	18.8 ± 0.1
147.8 GeV	1769.8 ± 0.8	77.5 ± 0.5	21.6 ± 0.1
100 GeV	1189.3 ± 0.3	58.0 ± 0.2	19.7 ± 0.1
80 GeV	948.1 ± 0.3	49.2 ± 0.2	18.6 ± 0.1
60 GeV	707.9 ± 1.0	37.0 ± 0.7	15.3 ± 0.2
40 GeV	471.2 ± 0.2	30.2 ± 0.1	14.1 ± 0.1
20 GeV	227.8 ± 0.1	20.9 ± 0.1	12.7 ± 0.0
10 GeV	109.6 ± 0.1	15.9 ± 0.1	11.5 ± 0.0

Table 5.10: Results for the FCal response to electrons, using topologically clustered data from beams directed at position 4L. Quoted uncertainties are statistical only.

The linearity obtained using topological clusters is shown in figure 5.21. The slopes obtained from the topologically clustered results are marginally higher than those obtained from cylindrical clustering, while the intercepts are slightly lower. Cells containing low amounts of energy may not be included in the topoclusters in cases where they would be included in a cylindrical cluster, giving the topoclusters a lower energy than the cylindrical clusters. This effect would be more significant at low energies than high energies,

Beam Energy (GeV)	Fitted Mean (ADC)	Fitted Width (ADC)	Noise (ADC)
193.1 GeV	2278.5 ± 0.7	91.9 ± 0.5	20.8 ± 0.1
147.8 GeV	1726.5 ± 0.8	73.2 ± 0.5	19.5 ± 0.1
100 GeV	1154.2 ± 0.3	56.5 ± 0.2	19.8 ± 0.1
80 GeV	913.8 ± 0.3	50.0 ± 0.2	18.7 ± 0.1
60 GeV	680.4 ± 0.4	41.1 ± 0.3	16.8 ± 0.1
40 GeV	446.9 ± 0.2	31.2 ± 0.1	14.8 ± 0.1
20 GeV	214.6 ± 0.1	22.1 ± 0.1	13.1 ± 0.0
10 GeV	101.2 ± 0.1	17.0 ± 0.1	11.6 ± 0.1

Table 5.11: Results for the FCal response to electrons, using topologically clustered data from beams directed at position 4H. Quoted uncertainties are statistical only.

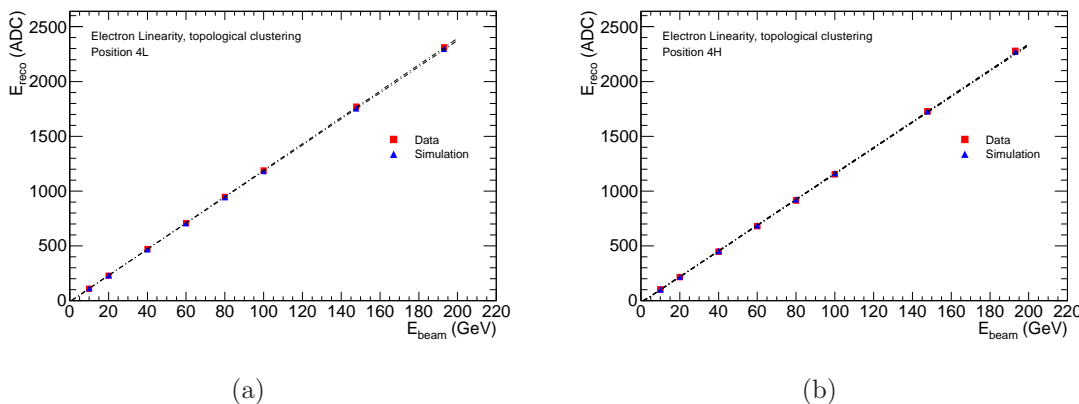


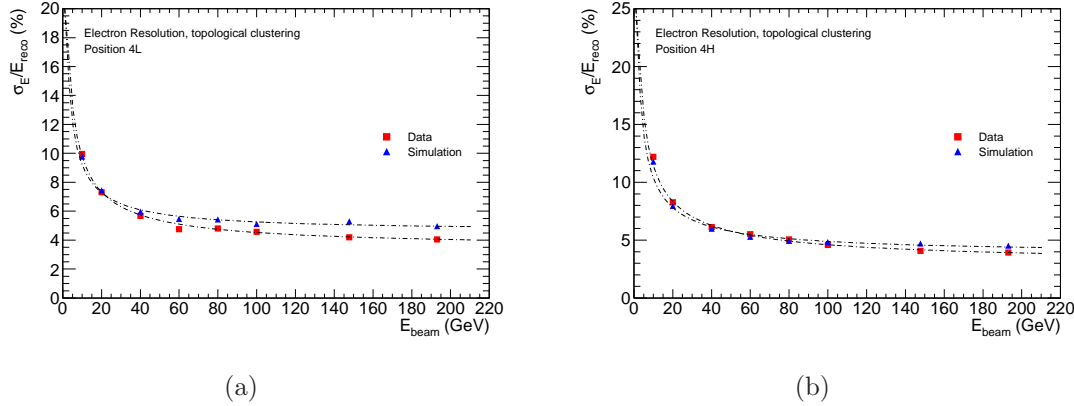
Figure 5.21: Ratio of reconstructed energy to the beam energy, for electrons directed at position 4L (left) and 4H (right).

and may explain the lower intercept and higher slope seen in the topoclustered results.

Systematics are estimated using the same method employed in the case for cylindrical clustering. To estimate the effect of the clustering method, a "430" clustering scheme was also used and compared with the results of the "420" method. The slope and intercept for topoclustered data at position 4L are 12.02 ± 0.04 GeV/ADC and -11.7 ± 1.2 ADC counts, respectively, where the quoted uncertainties are systematic. At position 4H, the slope is 11.75 ± 0.6 GeV/ADC and the intercept is -19.9 ± 2.3 ADC counts.

The energy resolution is plotted in figure 5.22, with fit results listed in table 5.13. The noise subtraction procedure is done in the same way as it was for the cylindrically

linearity result	slope (ADC/GeV)	Intercept (ADC)
Data (4L)	12.023 ± 0.002	-11.67 ± 0.07
Simulation (4L)	11.905 ± 0.003	-7.96 ± 0.12
Data (4H)	11.751 ± 0.002	-19.86 ± 0.09
Simulation (4H)	11.789 ± 0.003	-16.74 ± 0.12

Table 5.12: Linearity results for electron data. quoted uncertainties are statistical.**Figure 5.22:** Energy resolution of the FCal to electrons directed at position 4L (left) and position 4H (right).

clustered case. As cells with low energy are not included in the topological clusters, this reduces the number of cells sampled and causes a slight increase in the stochastic term compared to the case for cylindrical clustering.

	Stochastic Term (% GeV ^{1/2})	Constant Term (%)
Data (4L)	28.8 ± 0.1	3.49 ± 0.02
Simulation (4L)	25.2 ± 0.3	4.62 ± 0.02
Data (4H)	34.8 ± 0.2	3.02 ± 0.03
Simulation (4H)	30.5 ± 0.3	3.82 ± 0.03

Table 5.13: Fit parameters for energy resolution to electrons. Quoted uncertainties are statistical only.

5.3.2 Hadrons

The ratio of the mean response (at the EM scale) to the beam energy is plotted in figure ??, for hadron events that have been clustered topologically. These plots exhibit

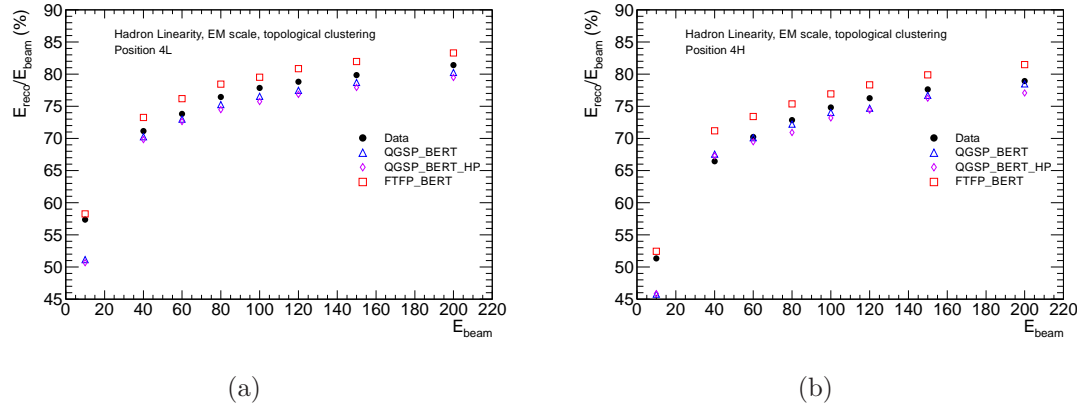


Figure 5.23: Ratio of energy reconstructed at the EM scale to the beam energy, for hadrons directed at position 4L (left) and 4H (right).

Beam Energy (GeV)	Fitted Mean (GeV)	Fitted Width (GeV)	Noise (GeV)
200 GeV	200.1 ± 0.1	19.6 ± 0.0	5.1 ± 0.0
150 GeV	147.1 ± 0.0	16.0 ± 0.0	4.7 ± 0.0
120 GeV	116.1 ± 0.1	13.9 ± 0.0	4.3 ± 0.0
100 GeV	95.6 ± 0.1	13.0 ± 0.1	4.8 ± 0.0
80 GeV	75.1 ± 0.1	11.0 ± 0.0	4.1 ± 0.0
60 GeV	54.3 ± 0.0	9.1 ± 0.0	3.6 ± 0.0
40 GeV	34.9 ± 0.1	7.6 ± 0.1	3.1 ± 0.0
10 GeV	7.0 ± 0.1	3.3 ± 0.0	1.9 ± 0.0

Table 5.14: FCal response to hadrons at position 4L, obtained from fits to topologically clustered data.

the same behaviour seen for cylindrical clustering, although there is better agreement between data and simulation at lower energies. The weights used for hadronic calibration are derived in the same way, and are plotted in figure ???. At high energy, the weights are very similar to those obtained with cylindrical clusters. At lower energies less energy is contained within the topological clustering, and so the derived weights in FCal1 and FCal2 are much larger than for the cylindrically clustered case.

The calibrated responses are plotted in figures 5.25 and ?? and summarised in tables 5.14 and 5.15. While the mean response is slightly diminished, the clustered noise is significantly lower due to the noise reducing properties of the topological clustering.

The mean response (hadronically calibrated) is plotted in figure 5.27 as a function

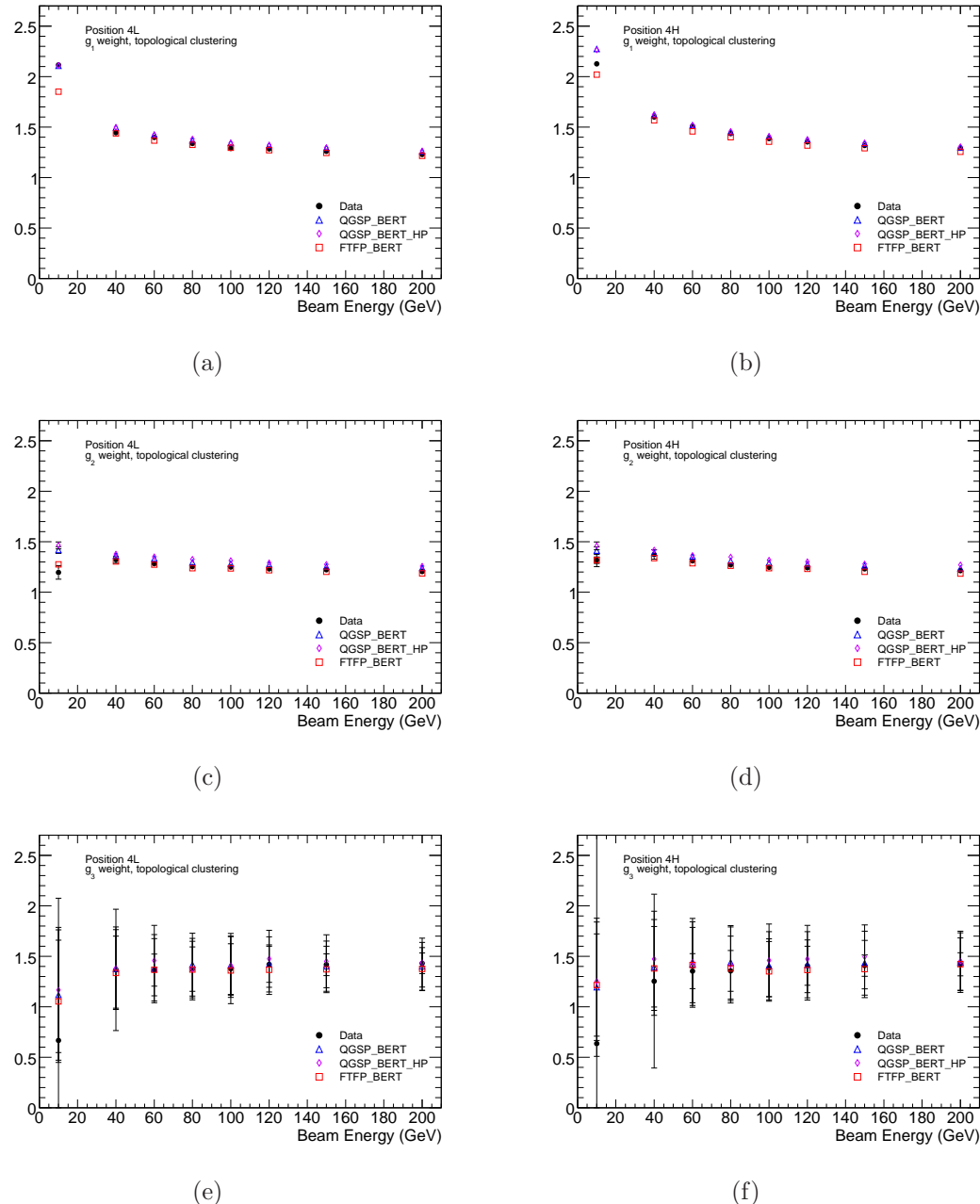


Figure 5.24: Flat weights used in hadronic calibration, as a function of the energy at which they are derived. Only the weights derived using 200GeV are used in the analysis.

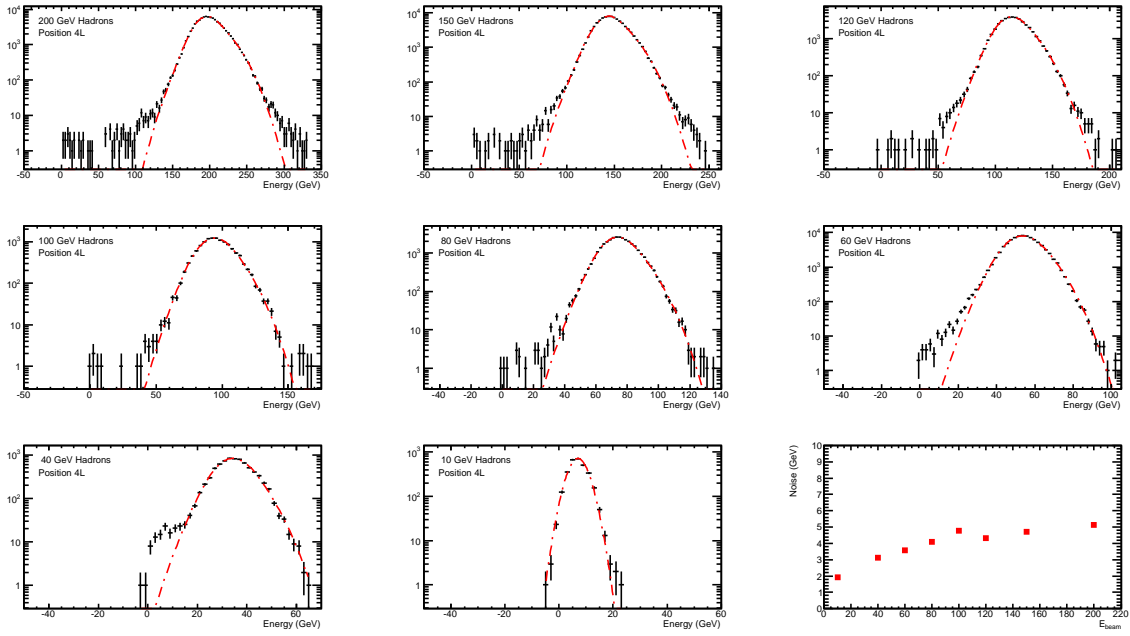


Figure 5.25: FCal response to hadron beams directed at position 4L.

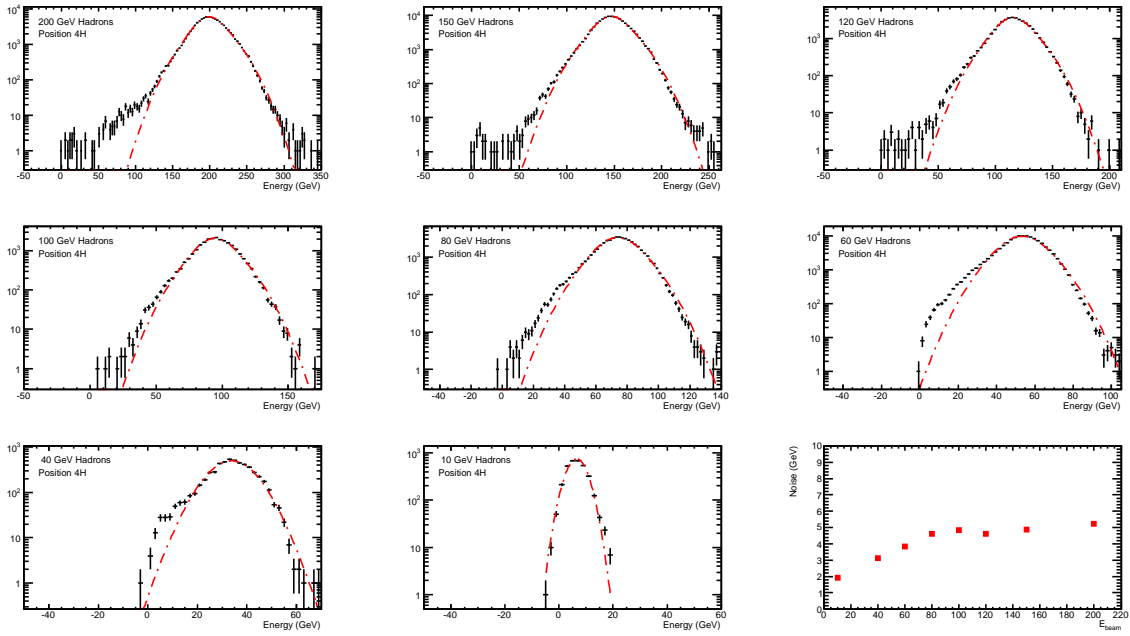


Figure 5.26: FCal response to hadron beams directed at position 4H.

of beam energy. Again, as most of the energy is deposited in FCal1 and FCal2, which have similar weights, the shape of this plot is very similar to that seen at the EM scale

Beam Energy (GeV)	Fitted Mean (GeV)	Fitted Width (GeV)	Noise (GeV)
200 GeV	200.2 ± 0.1	22.5 ± 0.0	5.2 ± 0.0
150 GeV	147.5 ± 0.0	18.6 ± 0.0	4.9 ± 0.0
120 GeV	116.0 ± 0.1	16.1 ± 0.1	4.6 ± 0.0
100 GeV	95.0 ± 0.1	15.2 ± 0.1	4.9 ± 0.0
80 GeV	74.0 ± 0.1	13.3 ± 0.0	4.6 ± 0.0
60 GeV	53.5 ± 0.0	10.8 ± 0.0	3.8 ± 0.0
40 GeV	33.8 ± 0.1	8.6 ± 0.1	3.1 ± 0.0
10 GeV	6.5 ± 0.1	3.4 ± 0.0	1.9 ± 0.0

Table 5.15: FCal response to hadrons at position 4H, obtained from fits to topologically clustered data.

in figure 5.23. While the topological clustering had only a slight effect on the linearity for electrons, the energy density in hadronic showers is much lower, and so the topological clustering excludes a significantly larger fraction of the energy. This results in the mean response being considerably lower at energies below 200GeV when compared to the cylindrically clustered case.

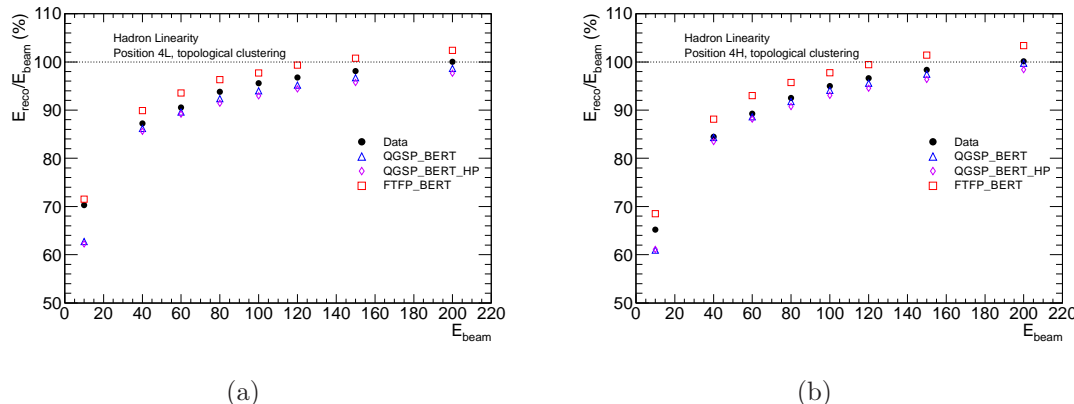


Figure 5.27: Ratio of reconstructed energy to the beam energy, for hadrons directed at position 4L (left) and 4H (right). Flat weights have been applied to calibrate the reconstructed energy to the hadronic scale.

The resolution is plotted in figure 5.28, and fit results are listed in table 5.16. Again, as less energy is included in the topological clusters the stochastic term is substantially increased compared to the resolutions obtained from cylindrical clustering. The stochastic terms increase by $\sim 20\% \text{GeV}^{1/2}$ at position 4L and by 10-20 % $\text{GeV}^{1/2}$ at position 4H. In

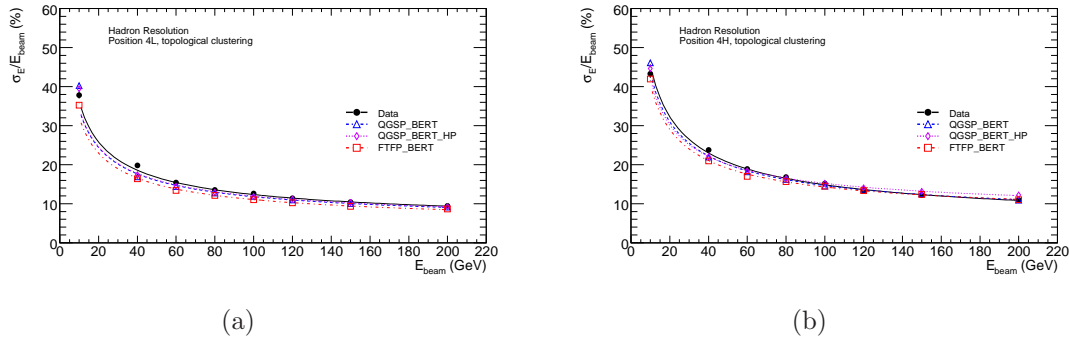


Figure 5.28: Energy resolution of the FCal to hadrons directed at position 4L (left) and position 4H (right). Flat weights have been applied to calibrate the reconstructed energy to the hadronic scale.

spite of this large increase in the stochastic term, the resolution at 200GeV is relatively unchanged. Systematic effects on the resolution are again dominated by the hadronic weights, giving values of $114 \pm 2\%$ GeV $^{1/2}$ for the stochastic term and $4.9 \pm 0.3\%$ for the constant term at position 4L. At position 4H the stochastic term is $137 \pm 6\%$ GeV $^{1/2}$ while the constant term is $3.8 \pm 1.3\%$.

	Stochastic Term (% GeV ^{1/2})	Constant Term (%)
Data (4L)	113.5 ± 0.4	4.86 ± 0.08
QGSP_BERT (4L)	107.0 ± 0.7	4.97 ± 0.12
QGSP_BERT_HP (4L)	107.6 ± 0.7	5.18 ± 0.12
FTFP_BERT (4L)	100.7 ± 0.6	4.59 ± 0.12
Data (4H)	143.6 ± 0.4	3.80 ± 0.12
QGSP_BERT (4H)	136.6 ± 0.8	5.30 ± 0.17
QGSP_BERT_HP (4H)	130.1 ± 0.8	7.77 ± 0.12
FTFP_BERT (4H)	126.4 ± 0.7	6.62 ± 0.13

Table 5.16: Fit parameters for energy resolution to hadrons, obtained using topologically clustered data. Quoted uncertainties are statistical only.

5.3.3 Cluster moments

reference the nim paper, compare our results to theirs (generally agree) Local Hadronic Calibration is another method for calibrating energy deposits to the hadronic scale. This method is applies to topological clusters, and makes use of various moments that describe

the shape of the energy deposit. These moments are used to classify a cluster as being electromagnetic or hadronic in nature, and the cluster is then weighted appropriately. Two of the most important of these moments are the energy density, ρ , and λ_c , which describes the depth of the energy deposit within the calorimeter.

These moments are plotted in figure 5.29 for electrons and figure 5.30 for hadrons. The data and simulation are generally in agreement for the electron results, however the simulation results for the cluster depth have a tail at high λ_c which significantly enhanced compared to that seen in data.

For hadrons, the data and simulation agree quite well. The simulation results for the energy density are a little higher than that seen in data, while for the cluster depth the simulation results are a little lower. These results are expected given that the simulation generates showers that are shorter and narrower than those seen in data (c.f. figures 5.11 and 5.10).

s in MeV

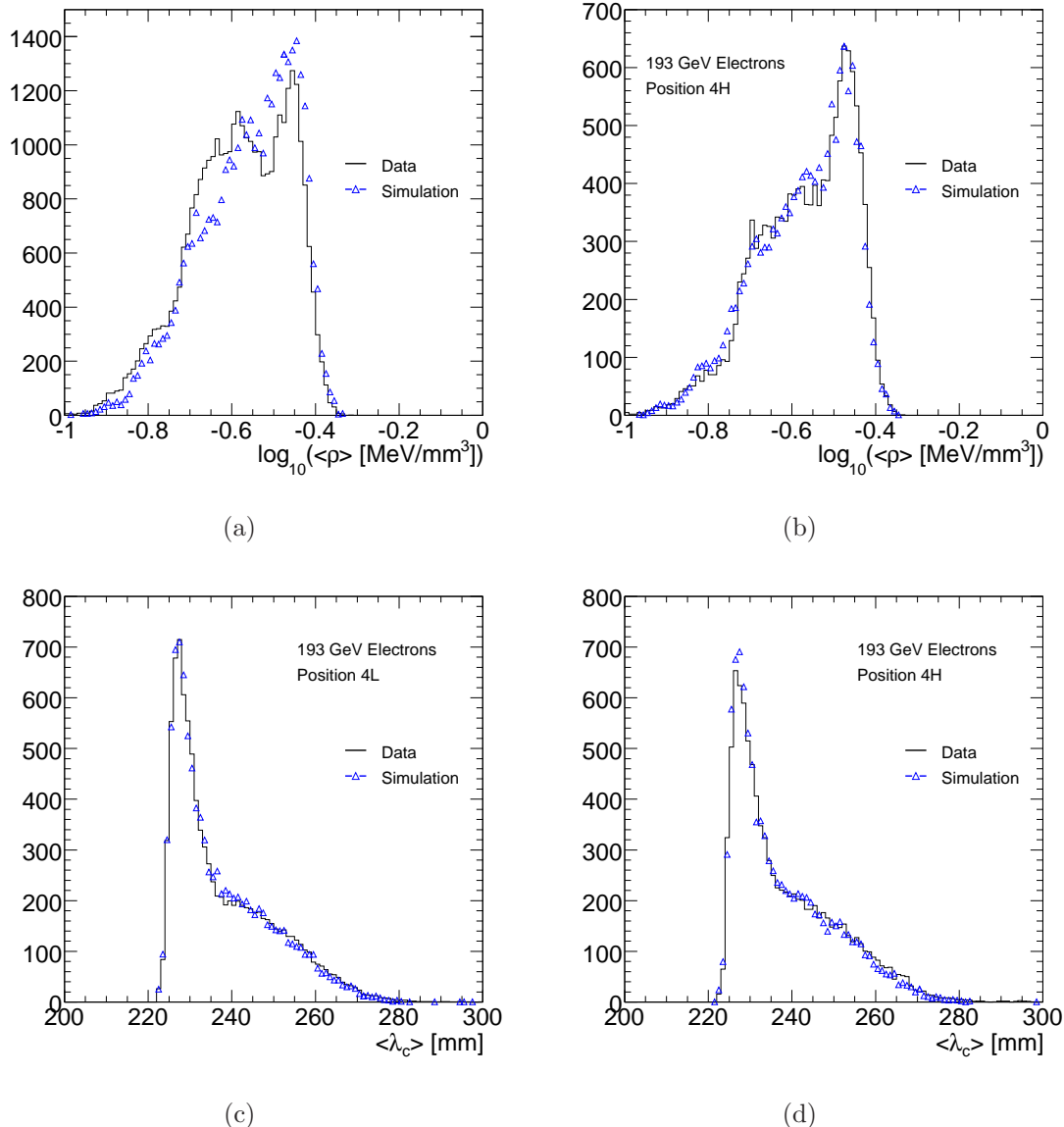


Figure 5.29: Shower moments derived from topological clusters. The upper plots show the energy density of clusters resulting from 193GeV electrons directed at position 4L (left) and 4H (right). The lower plots show the distribution of λ_c , which describes the depth of the cluster centre within the calorimeter.

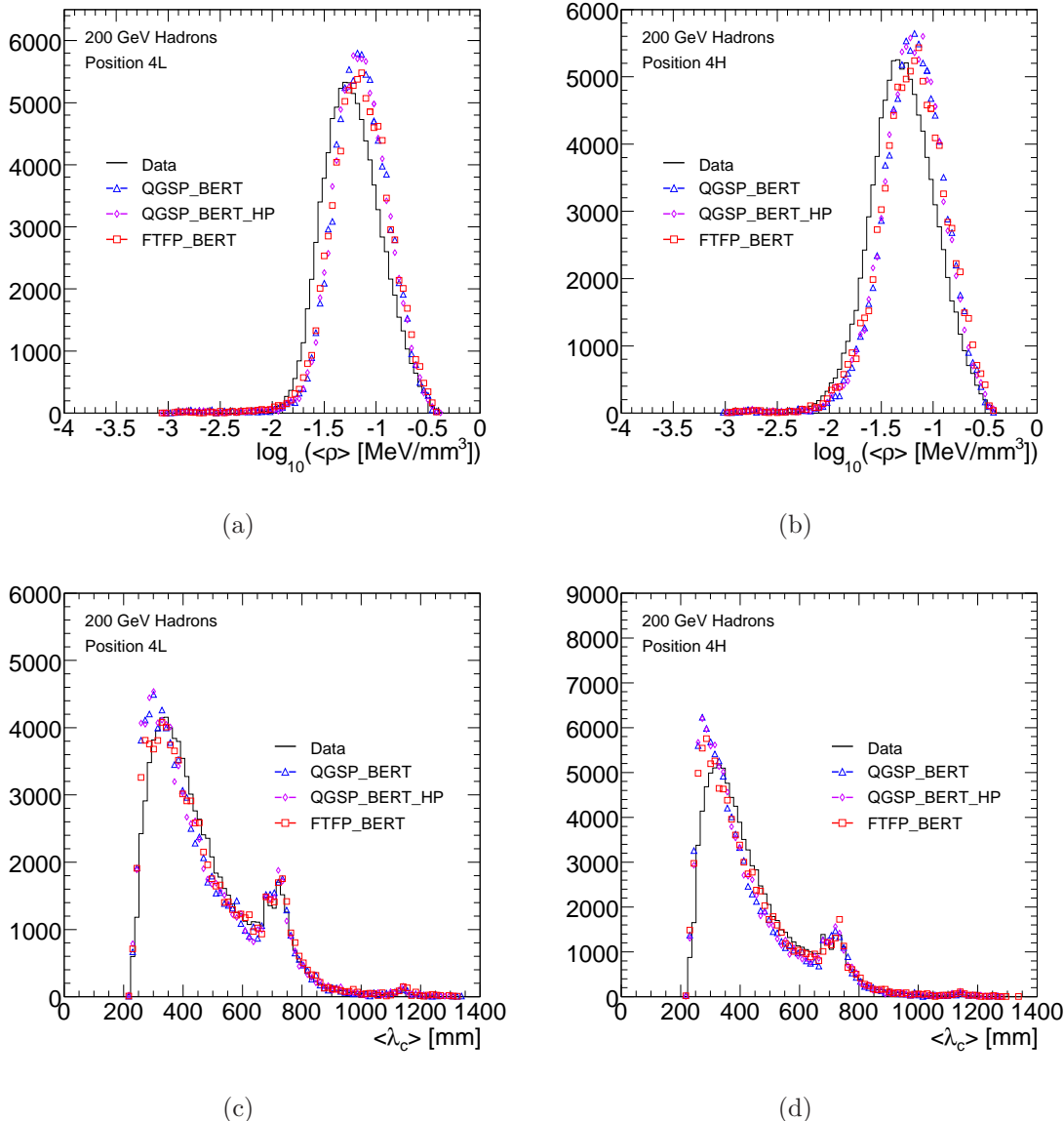


Figure 5.30: Shower moments derived from topological clusters. The upper plots show the energy density of clusters resulting from 200GeV hadrons directed at position 4L (left) and 4H (right). The lower plots show the distribution of λ_c , which describes the depth of the cluster centre within the calorimeter.

Bibliography

- [1] *ATLAS tile calorimeter: Technical Design Report*. Technical Design Report ATLAS. CERN, Geneva, 1996.
- [2] Atlas calorimeter response to single isolated hadrons and estimation of the calorimeter jet scale uncertainty. Technical Report ATLAS-CONF-2011-028, CERN, Geneva, Mar 2011.
- [3] Combination of higgs boson searches with up to 4.9 fb-1 of pp collisions data taken at a center-of-mass energy of 7 tev with the atlas experiment at the lhc. Technical Report ATLAS-CONF-2011-163, CERN, Geneva, Dec 2011.
- [4] In-situ pseudorapidity intercalibration for evaluation of jet energy scale uncertainty using dijet events in proton-proton collisions at $\sqrt{s}=7$ tev. Technical Report ATLAS-CONF-2011-014, CERN, Geneva, Mar 2011.
- [5] R. Achenbach et al. The ATLAS level-1 calorimeter trigger. *JINST*, 3:P03001, 2008.
- [6] G. Altarelli and G. Parisi. Asymptotic freedom in parton language. *Nuclear Physics B*, 126(2):298 – 318, 1977.
- [7] B. Andersson, G. Gustafson, and B. Nilsson-Almqvist. A model for low-pt hadronic reactions with generalizations to hadron-nucleus and nucleus-nucleus collisions. *Nuclear Physics B*, 281(1-2):289 – 309, 1987.

- [8] J. P. Archambault et al. Energy calibration of the ATLAS liquid argon forward calorimeter. *JINST*, 3:P02002, 2008.
- [9] J.C. Armitage, A. Artamonov, L. Austin, V. Epchtein, V. Jemanov, K. Johns, V. Khovansky, P. Loch, J.K. Mayer, R. Norton, R.S. Orr, J.P. Rutherford, M. Ryabinin, A. Savin, P. Shatalov, L. Shaver, M. Shupe, G. Stairs, J. Steinberg, and D. Tompkins. Results for electrons from the 1995 atlas forward calorimeter prototype testbeam. *Nuclear Physics B - Proceedings Supplements*, 61(3):101 – 105, 1998.
|ce:title|Proceedings of the Fifth International Conference on Advanced Technology and Particle Physics|ce:title|.
- [10] J.C. Armitage, A. Artamonov, L. Babukhadia, M. Dixit, T.M. Embry, et al. Electron signals in the forward calorimeter prototype for ATLAS. *JINST*, 2:P11001, 2007.
- [11] A Artamonov, D Bailey, G Blanger, M Cadabeschi, T Y Chen, V Epshteyn, P Gorbunov, K K Joo, M Khakzad, V Khovanskiy, P Krieger, P Loch, J Mayer, E Neuheimer, F G Oakham, M O'Neill, R S Orr, M Qi, J Rutherford, A Savine, M Schram, P Shatalov, L Shaver, M Shupe, G Stairs, V Strickland, D Tompkins, I Tsukerman, and K Vincent. The atlas forward calorimeter. *J. Instrum.*, 3:P02010, 2008.
- [12] Bernard Aubert et al. Development and construction of large size signal electrodes for the ATLAS electromagnetic calorimeter. *Nucl. Instrum. Meth.*, A539:558–594, 2005.
- [13] V.S. Barashenkov, H.W. Bertini, K. Chen, G. Friedlander, G.D. Harp, A.S. Iljinov, J.M. Miller, and V.D. Toneev. Medium energy intranuclear cascade calculations: a comparative study. *Nuclear Physics A*, 187(3):531 – 544, 1972.
- [14] Hugo W. Bertini. Low-energy intranuclear cascade calculation. *Phys. Rev.*, 131:1801–1821, Aug 1963.

- [15] Volker Blobel. An Unfolding method for high-energy physics experiments. pages 258–267, 2002.
- [16] Claude Bovet, Rne Maleyran, L Piemontese, Alfredo Placci, and Massimo Placidi. *The CEDAR counters for particle identification in the SPS secondary beams: a description and an operation manual*. CERN, Geneva, 1982.
- [17] C.P. Burgess and G.D. Moore. *The Standard Model: A Primer*. Cambridge University Press, 2007.
- [18] Matteo Cacciari, Gavin P. Salam, and Gregory Soyez. The antik_t jet clustering algorithm. *JHEP*, 04:063, 2008.
- [19] W.E. Cleland and E.G. Stern. Signal processing considerations for liquid ionization calorimeters in a high rate environment. *Nuclear Instruments and Methods in Physics Research Section A: Accelerators, Spectrometers, Detectors and Associated Equipment*, 338(2-3):467 – 497, 1994.
- [20] J. Colas, M. Pripstein, and W. A. Wenzel. The electrostatic transformer. *Nuclear Instruments and Methods in Physics Research A*, 294:583–590, September 1990.
- [21] ATLAS Collaboration. Measurement of inclusive jet and dijet cross sections in proton-proton collisions at 7 TeV centre-of-mass energy with the ATLAS detector. 2010.
- [22] ATLAS Collaboration. Measurement of jet production in 7 tev proton-proton collisions with the atlas detector. Technical Report ATLAS-COM-CONF-2010-052, CERN, Geneva, Jun 2010. See back up note for full author list.
- [23] The ATLAS Collaboration. The atlas experiment at the cern large hadron collider. *Journal of Instrumentation*, 3(08):S08003, 2008.

- [24] John C. Collins, Davison E. Soper, and George Sterman. Factorization for short distance hadron-hadron scattering. *Nuclear Physics B*, 261(0):104 – 142, 1985.
- [25] M.I. Ferguson, L. Harlow, P. Loch, M. Qi, J. Rutherford, A. Savine, L. Shaver, M. Shupe, J. Steinberg, C. Zeitnitz, and D. Rahm. Electron testbeam results for the atlas liquid argon forward calorimeter prototype. *Nuclear Instruments and Methods in Physics Research Section A: Accelerators, Spectrometers, Detectors and Associated Equipment*, 383(220133):399 – 408, 1996.
- [26] H. Fesefeldt. The simulation of hadronic showers physics and applications. Technical Report PITHA-85/02, Aachen Technische Hochschule, Germany, 1985.
- [27] G Folger and J P Wellisch. String parton models in geant4. 2003.
- [28] D. M. Gingrich et al. Construction, assembly and testing of the ATLAS hadronic end-cap calorimeter. *JINST*, 2:P05005, 2007.
- [29] W. Greiner, S. Schramm, and E. Stein. *Quantum Chromodynamics*. Springer, 2007.
- [30] L. Heelan. *Calibration of the ATLAS Forward Calorimeter and a Study of the Top Quark Production Cross-section Measurement in the Dilepton Channel*. PhD thesis, Carleton University (Canada), 2011.
- [31] E Khramov, N Rusakovich, T Carli, A Henriques, V Giangiobbe, Z Liang, C Santoni, and M Simonyan. Study of the response of the hadronic barrel calorimeter in the atlas combined test-beam to pions of energies from 20 to 350 gev for beam impact points from 0.2 to 0.65. Technical Report ATL-TILECAL-PUB-2009-007. ATL-COM-TILECAL-2009-006, CERN, Geneva, Apr 2009.
- [32] P. Krieger. Density of hadronic modules. private communication, 2007.
- [33] Hung-Liang Lai, Marco Guzzi, Joey Huston, Zhao Li, Pavel M. Nadolsky, et al. New parton distributions for collider physics. *Phys.Rev.*, D82:074024, 2010.

- [34] Hung-Liang Lai, Marco Guzzi, Joey Huston, Zhao Li, Pavel M. Nadolsky, et al. CT10 global analysis, additional figures and results, 2012. <http://hep.pa.msu.edu/cteq/public/ct10/figs/>.
- [35] W Lampl, S Laplace, D Lelas, P Loch, H Ma, S Menke, S Rajagopalan, D Rousseau, S Snyder, and G Unal. Calorimeter clustering algorithms: Description and performance. (ATL-LARG-PUB-2008-002. ATL-COM-LARG-2008-003), Apr 2008.
- [36] P. Loch. Testbeam results for the ATLAS forward calorimeter module 0. pages 184–191, 1999.
- [37] Bogdan Malaescu. An Iterative, dynamically stabilized method of data unfolding. 2009.
- [38] Bogdan Malaescu. An Iterative, Dynamically Stabilized(IDS) Method of Data Unfolding. 2011.
- [39] Laurence W. Nagel and D.O. Pederson. Spice (simulation program with integrated circuit emphasis). Technical Report UCB/ERL M382, EECS Department, University of California, Berkeley, Apr 1973.
- [40] J. Pinfold, J. Soukup, J.P. Archambault, C. Cojocaru, M. Khakzad, G. Oakham, M. Schram, M.G. Vincter, V. Datskov, V. Drobin, A. Fedorov, S. Golubykh, N. Javadov, V. Kalinnikov, S. Kakurin, M. Kazarinov, V. Kukhtin, E. Ladygin, A. Lazarev, A. Neganov, L. Petrova, I. Pisarev, N. Rousakovitch, E. Serochkin, S. Shilov, A. Shalyugin, Yu. Usov, D. Bruncko, E. Kladiva, P. Stavina, P. Strizenec, F. Barreiro, C. Gabaldon, F. Labarga, E. Nebot, C. Oliver, S. Rodier, J. del Peso, A. Belkin, M. Heldmann, L. Koepke, R. Othegraven, T. Schliephake, D. Schroff, H. Secker, J. Thomas, C. Zeitnitz, C. Benchouk, F. Djama, F. Hubaut, E. Monnier, V. Niess, P. Pralavorio, M. Raymond, B. Resende, D. Sauvage, C. Serfon,

- S. Tisserant, J. Toth, G. Azuelos, P. Delsart, C. Leroy, R. Mehdiyev, A. Akinmov, M. Blagov, A. Komar, A. Snesarev, M. Speransky, V. Sulin, M. Yakimenko, V. Epshteyn, V. Khovansky, P. Shatalov, M. Aderholz, T. Barillari, W. Cwienk, A. Fischer, J. Habring, J. Huber, A. Karev, A. Kiryunin, L. Kurchaninov, S. Menke, P. Mooshofer, H. Oberlack, D. Salihagic, P. Schacht, T. Chen, J. Ping, M. Qi, V. Kazanin, V. Malyshev, A. Maslennikov, G. Pospelov, R. Snopkov, A. Soukharev, A. Talyshев, Y. Tikhonov, P. Cavalleri, P. Schwemling, S. Chekulaev, S. Denisov, V. Evdokimov, M. Levitsky, A. Minaenko, G. Mitrofanov, A. Moiseev, A. Pleskatch, D. Stoyanova, L. Zakamsky, M. Bieri, D. O'Neil, J. Rani, D. Schouten, M. Vetterli, P. Loch, J. Rutherford, A. Savin, L. Shaver, M. Shupe, C. Galt, P. Gorbounov, N. Knecht, P. Krieger, L. Ma, R. Mazini, R. Orr, M. Losty, C.J. Oram, M. Wielers, P.S. Birney, M. Fincke-Keeler, I. Gable, T.A. Hodges, T. Hughes, T. Ince, N. Kanaya, R.K. Keeler, R. Langstaff, M. Lefebvre, M. Lenckowski, R. McPherson, W. Shaw, H.M. Braun, and J. Thadome. Performance of the atlas liquid argon endcap calorimeter in the pseudorapidity region in beam tests. *Nuclear Instruments and Methods in Physics Research Section A: Accelerators, Spectrometers, Detectors and Associated Equipment*, 593(3):324 – 342, 2008.
- [41] P. Speckmayer. Impact of the choice of physics list on geant4 simulations of hadronic showers in tungsten. Technical Report LCD-Note-2010-00, CERN, Switzerland, 2010.